Université catholique de Louvain

Institute of Condensed Matter and Nanosciences

Structural and interfacial engineering of borohydride-based solid electrolytes for alkali-metal batteries

Yuqin Fan

Supervisor

Prof. Yaroslav Filinchuk

June, 2026

Université catholique de Louvain

Institute of Condensed Matter and Nanosciences

Structural and interfacial engineering of borohydride-based solid electrolytes for alkali-metal batteries

Yuqin Fan

Jury Member:

Prof. Yaroslav Filinchuk (UCLouvain, Belgium), supervisor

Prof. Jean-François Gohy (UCLouvain, Belgium), president

Prof. Alexandru Vlad (UCLouvain, Belgium)

Prof. Torben R. Jensen (Aarhus University, Denmark)

Prof. Jiande Wang (Hunan University, China)

June, 2026

Acknowledgements

Time flies quickly, my five-year PhD journey is now coming to an end. Looking back on these years, I am filled with gratitude and reflection. I am truly glad to have spent this precious period at the Université catholique de Louvain (UCLouvain) in Belgium. These five years have not only allowed me to develop my research skills systematically but also helped me grow as a person, becoming more mature and resilient.

Throughout my PhD studies, I owe my deepest gratitude to my supervisor, Prof. Yaroslav Filinchuk, for his continuous guidance, trust, and inspiration. He gave me great freedom in exploring research directions while always providing invaluable advice on scientific thinking, experimental design, data analysis, manuscript preparation, and project management. His rigorous approach to science, open-mindedness, and patient mentorship have deeply influenced me and will continue to guide my future career.

I am also sincerely grateful to Dr. Li Xiao, whose support and encouragement were important at the early stage of my PhD application. His help during the China Scholarship Council (CSC) application process made it possible for me to begin my doctoral studies at UCLouvain.

I would like to sincerely thank Prof. Alexandru Vlad, Prof. Jean-François Gohy, and Jean-François Statsyns, as well as members of Prof.

Vlad's laboratory, for granting me access to essential characterization facilities, which made it possible for me to carry out my experiments successfully.

I also extend my sincere thanks to the members of my doctoral jury: Prof. Alexandru Vlad, Prof. Jean-François Gohy, Prof. Torben R. Jensen, and Prof. Jiande Wang, for their time, valuable suggestions, and engagement in my work.

My warmest thanks go to my colleagues and friends in the laboratory: Dr. Igor Golub, Dr. Timothy Steenhaut, Dr. Ting Zhang, Dr. Jian Wang, Fang Xia, Nicolas Malherbe, Guillaume Esser, and Loic Rochez Laduze. All those who have supported me during my research. Thank you for the inspiring discussions, the help with experiments, and the joyful moments we shared. Your support made this long research journey both meaningful and enjoyable.

I am also grateful to Dr. Xiaodong Li and Dr. Shanshan Yan for their valuable guidance and feedback on my thesis, as well as for their support during the times when I faced challenges and uncertainty in my experiments. Their thoughtful advice helped me stay focused and motivated.

I am deeply thankful to my friends, both in Belgium and in China, Dr. Qian Qin, Dr. Tie Da, Dr. Mengmeng Wang, Xiaochun Li, Ting Wen, Yinghui Zhang, Yihua Jiang, Kejie Zhou, Zhenni He, Zhijie Zhou…… For their care, encouragement, and companionship. Your kindness and

understanding gave me strength during the challenging times of my PhD life. To those who provided advice in my studies, shared laughter in my daily life, or simply offered comforting words when I was down -thank you for being there.

My sincere thanks also go to my former colleagues, Zewei Hu and Xueao Jiang in China, who provided generous support in experimental testing and data analysis. Their assistance made it possible for me to complete several crucial parts of this work and reminded me of the warmth and power of scientific collaboration.

I gratefully acknowledge the financial support of the China Scholarship Council (CSC) for its financial support during my doctoral studies, which made it possible for me to pursue my research at UCLouvain. I also thank FNRS (Belgium) and Fédération Wallonie-Bruxelles (ARC MicroBat) for financial support.

Finally, my deepest gratitude goes to my family. To my parents, thank you for your endless love and trust, and for always supporting my choices. To my husband, Jiahao Lei, thank you for taking care of our family during my PhD years and allowing me to focus wholeheartedly on my research. To my child, your smile has been my greatest source of happiness and motivation. It is the love and support of my family that have sustained me throughout this journey and given me true peace and joy.

Author Contributions

The study was designed by the author and her supervisor, Prof. Yaroslav Filinchuk. The author conducted the majority of experimental work, including material synthesis, characterization, electrochemical testing, and other analyses, and was responsible for writing the manuscript.

The valuable contributions are as follows:

SEM images were collected by ZeWei Hu (Central South University, China); BET data were collected by Xueao Jiang (Hunan University, China) and Guillaume Esser (UCLouvain). For Chapter 6, Dr. Igor Golub made synthesis described in Chapter 6, Prof. Yaroslav Filinchuk solved crystal structures, and Joel Omale provided support for conductivity measurements (all from UCLouvain). TGA and DSC were recorded by Dr. Xiao Li (Hefei General Machinery Research Institute, China) and Jean-François Statsyns (UCLouvain); XPS data was recorded by Pierre Eloy (UCLouvain), and synchrotron XRD data was collected at the ESRF.

List of Acronyms

ASSBs	All-solid-state batteries
ASSLBs	All Solid-State Lithium Batteries
ASSSBs	All Solid-State Sodium Batteries
ATR	Attenuated total reflectance
A-LLTO	Aluminum-doped lanthanum lithium titanate
BN	Boron nitride
BCC	Body-centered cubic
BPR	Balls-Powder-Ratio
CC	Critical Current Density
CV	Cyclic voltammogram
DSC	Differential scanning calorimetry
DC	Direct current polarization
2D	Two-dimensional
$DMS{\cdot}BH_3$	Borane dimethyl sulfide complex
DFT	Density-functional theory
ESRF	European Synchrotron Radiation Facility in Grenoble
EIS	Electrochemical impedance spectroscopy
ESWs	Electrochemical stability windows
FTIR	Fourier-transform infrared spectroscopy
FCC	Face-centered cubic
GC	Galvanostatic cycling
GCD	Galvanostatic charge-discharge
HT	High-temperature
LE	Liquid electrolytes
LIBs	Lithium-ion batteries
LTO	Lithium titanate, $Li_4Ti_5O_{12}$
LT	Low-temperature
LLZO	Lithium lanthanum zirconium oxide, $Li_7La_3Zr_2O_{12}$

LMA	Lithium metal anode
LSV	Linear sweep voltammetry
MOF	Metal-organic framework
$M(BH_4)m$	Metal borohydrides (M = Li, Na, K, Mg, etc.)
MCM-41	Mesoporous silica
NASICON	Sodium superionic conductor
NMR	Nuclear magnetic resonance
OCV	Open circuit voltage
PXRD	Powder X-ray diffraction
PVDF	Polyvinylidene fluoride
PVC	Polyvinyl chloride
PAN	Polyacrylonitrile
PEO	Polyethylene oxide
QENS	Quasi-elastic neutron scattering
R_4	Tetraalkyl
R_4NBH_4	Tetraalkylammonium borohydride
SIBs	Sodium-ion batteries
SEM	Scanning Electron Microscopy
SSE	Solid-state electrolyte
SNBL	Swiss-Norwegian Beamlines at the ESRF
SR-RD	Synchrotron radiation Powder X-ray diffraction
SS	Stainless steel
TMAB	Tetramethylammonium borohydride
TEAB	Tetraethylammonium borohydride
TBAB	Tetrabutylammonium borohydride
TGA	Thermogravimetric analysis
THF	Tetrahydrofuran
XPS	X-ray photoelectron spectroscopy
$[Me_4N]$	Tetramethylammonium cation
$[Et_4N]$	Tetraethylammonium cation
$[Bu_4N]$	Tetrabutylammonium cation

Table of Contents

Abstract

Lithium-ion batteries (LIBs) are widely used in electronic devices and large-scale energy storage systems, yet the flammability of organic liquid electrolytes poses inherent safety risks. All-solid-state lithium-ion batteries (ASSLIBs), which employ non-flammable solid electrolytes, significantly improve safety, while the limited availability of lithium resources further motivates the development of all-solid-state sodium-ion batteries (ASSSIBs). Metal borohydrides have attracted extensive interest due to their solvent-free synthesis, favorable mechanical properties, low density and excellent thermal and chemical stability; however, their low room-temperature ionic conductivity, narrow electrochemical stability windows, and insufficient compatibility with metal anodes still hinder practical application.

This thesis employs structural engineering and interfacial engineering strategies to enhance ionic transport and electrochemical stability in borohydride-based solid electrolytes. A series of materials, $LiBH_4$, $Na_2B_{12}H_{12}$, $LiBH_4$-$2LiNH_2$, and R_4N-Li-BH_4 (R = methyl (Me), ethyl (Et), and butyl (Bu)), were synthesized via mechanochemical routes. Structural, thermal, and electrochemical characterizations were conducted to establish structure-property relationships, and the materials were evaluated in Li‖Li, Na‖Na, and $Li_4Ti_5O_{12}$-based all-solid-state cells.

Chapters 3 and **4** investigate the effect of zeolites on $LiBH_4$ and

$Na_2B_{12}H_{12}$. The results demonstrate that the three-dimensional porous network of zeolites forms continuous interfacial ion-conductive layers between borohydride particles, significantly enhancing both Li^+ and Na^+ conductivities. Owing to the extremely low electronic conductivity of the composites, interfacial side reactions are effectively suppressed, yielding excellent compatibility with Li and Na metal anodes.

Chapter 5 introduces two-dimensional BN into the $LiBH_4$-$2LiNH_2$ system to regulate the interfacial structure and ion transport pathways. BN enhances particle-particle contact and promotes the formation of extended interfacial pathways, resulting in a nearly three orders of magnitude increase in room-temperature Li conductivity. Li||Li symmetric cells exhibit stable plating/stripping behavior and good interfacial compatibility with LTO, with an expanded electrochemical stability window of ~3.28 V, demonstrating BN serves as an effective interfacial modifier for regulating ion transport and interfacial behavior in $LiBH_4$-$LiNH_2$-based electrolytes.

Chapter 6 further expands the borohydride family by introducing tetraalkylammonium cations (R_4N^+) to construct new organic-inorganic hybrid borohydride derivatives, R_4N-Li-BH_4. The steric and polarization effects of R_4N^+ tune the crystal structure, enabling multiple polymorphs (e.g., *Immm* and *Pnma*), which are expected to influence BH_4^- orientational dynamics and Li^+ transport behavior, reducing the Li^+ migration barrier, and improving ionic conductivity. Their structural

tunability and thermal stability highlight their potential as next-generation borohydride-based solid electrolytes.

Overall, this thesis demonstrates that structural and interfacial engineering strategies can effectively enhance ionic conductivity, electrochemical stability, and metal-anode compatibility in borohydride-based solid electrolytes, providing new insights and theoretical foundations for the design and development of advanced borohydride solid electrolyte materials.

Chapter 1 Introduction

1.1 All solid-state batteries

Energy plays a vital role in human survival and progress, serving as the foundation for the advancement of civilization. In the context of the 21st century, the confluence of energy crises, environmental concerns, declining oil resources, and environmental pollution has accelerated the search for clean and sustainable energy sources. Among these, storage and energy sources have developed rapidly in recent years. However, their effective use depends strongly on the development of safe, reliable, and cost-efficient energy storage systems, which are indispensable for the large-scale integration of renewable energy into modern society.

Among various energy storage devices, rechargeable batteries have gained widespread application due to their high cost-effectiveness, high energy density, and excellent efficiency in energy conversion and storage. They offer reliable performance, rapid response, and long cycle life, making them suitable for a wide range of applications, from portable electronics and electric vehicles to large-scale grid energy storage systems[1]. Commonly available batteries in the market include lead-acid batteries, nickel-cadmium batteries, nickel-metal hydride batteries, and lithium-ion batteries.

Lithium-ion batteries (LIBs) have emerged as the technological leaders in the battery industry, becoming the preferred chemical power source for electronic products such as laptops and mobile phones without exception. This is because lithium-ion batteries offer

advantages such as high specific capacity, high voltage platform, good cycling stability, and environmental friendliness. With the development of the electric vehicle industry and the growing power demand, lithium-ion batteries have also become one of the most promising energy systems. However, there is still a need for further improvements in energy density, safety performance, service life, and cost for lithium-ion batteries to meet the requirements[2].

Sodium-ion batteries (SIBs) are a promising substitute for LIBs thanks to the natural resources and low cost of sodium. Although their energy density is somewhat lower than that of lithium systems, SIBs are considered promising for large-scale stationary energy storage[3], Research on sodium-based solid electrolytes and all-solid-state sodium batteries is also progressing rapidly, following similar design principles to those of Li-based systems[4].

Traditional second batteries commonly employ organic liquid-based electrolytes, under extreme operating conditions, they may cause leakage and thermal aging, which can severely compromise the safety and long-term stability of batteries. In contrast, solid-state electrolytes exhibit superior thermal and mechanical stability, effectively mitigating these risks. As a result, solid-state electrolytes for Li- and Na-based batteries are becoming an important direction for future battery development.

In traditional liquid-based batteries, during charging, Li^+ ions are

extracted from the lithium-containing compounds in the cathode, migrate through the liquid electrolyte, and accumulate at the anode, where they gain electrons and are inserted into the carbon-based anode material. During discharge, the Li stored in the carbon material is oxidized to Li^+ by losing electrons, migrates back through the electrolyte, and re-intercalates into the cathode. The working principle is illustrated in **Fig. 1.1**[5]. The separator serves to physically isolate the cathode and anode materials, preventing short circuits while providing a pathway for Li^+ migration.

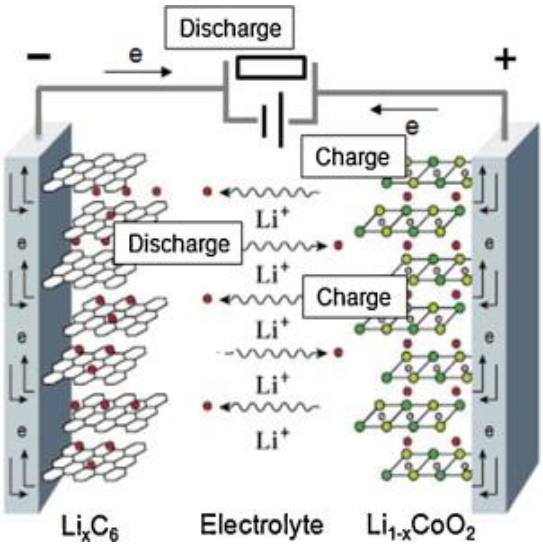

Fig. 1.1 Schematic diagram of the rechargeable Li-ion battery[5].

Alternatively, all-solid-state batteries (ASSBs) have attracted significant attention due to their enhanced safety and stability [6]. The schematic structure of an ASSB is shown in **Fig. 1.2**. Compared with conventional commercial batteries, ASSBs employ solid electrolytes

instead of organic liquid electrolytes and separators, enabling more flexible and compact cell designs with reduced weight and volume[6].

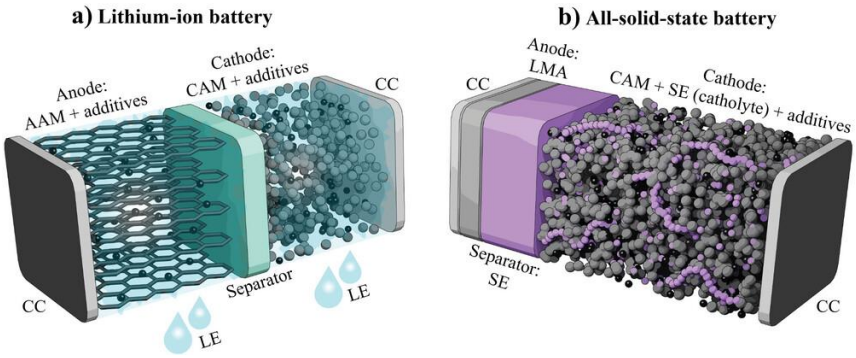

Fig. 1.2 A schematic representation of the comparison of lithium-ion battery and all-solid-state battery[6].

Current research on solid-state lithium metal batteries commonly employs two approaches for fabricating composite cathodes. In one method, the cathode active material, conductive additives, and solid electrolytes are pre-mixed in appropriate ratios, followed by dispersion with dried polyvinylidene fluoride (PVDF), solid electrolyte powders, and a solvent to form a homogeneous slurry. This slurry is then processed through coating, drying, calendaring, and cutting to obtain composite cathodes. Alternatively, the cathode active material, conductive additives, and solid electrolytes can be thoroughly milled and directly pressed onto one side of the solid electrolyte to construct the composite cathode structure.

An ideal cathode material should meet the following requirements: (1) relatively high and stable operating voltage; (2) high specific capacity; (3) good structural stability; (4) chemical compatibility with the solid electrolyte; and (5) environmental friendliness and cost-effectiveness. **Table 1.1** compares the performance of commonly used cathode materials[7].

Table 1.1 Typical cathode materials in solid-state batteries.

Cathode material	Theoretical capacity	Actual capacity	Voltage	Number of cycles	Ref.
$LiMn_2O_4$	148	100-120	3.8-4.25	300	[8]
$LiCoO_2$	274	200-210	3.0-4.6	100	[9]
$LiNi_xCo_yMn_zO_2$	285	200-210	2.7-4.3	100	[10]
$LiNiO_2$	274	140-150	2.5-4.5	100	[11]
$LiNiPO_4$	170	90-100	4.1-5.2	50	[12]
$LiNi_{0.5}Mn_{1.5}O_4$	148	105-115	3.45-4.95	100	[13]
TiS_2	275	180-190	1.6-2.7	300	[14]

Anode materials for all-solid-state batteries include lithium metal, alloy metal, and graphite. An ideal anode candidate for all-solid-state batteries is lithium metal, which can offer high energy density greater than 1,100 Wh L^{-1} and specific energy approaching 400 Wh kg^{-1} (**Fig. 1.3**). Unfortunately, many electrolytes are electrochemically and

chemically unstable against Li, and the formation of lithium dendrites can even pierce through the solid electrolyte layer, leading to short circuits in the cell[15]. At present, the use of lithium metal in all-solid-state lithium-ion batteries remains highly challenging unless the formation mechanism of lithium dendrites is thoroughly understood and effectively mitigated[16–19].

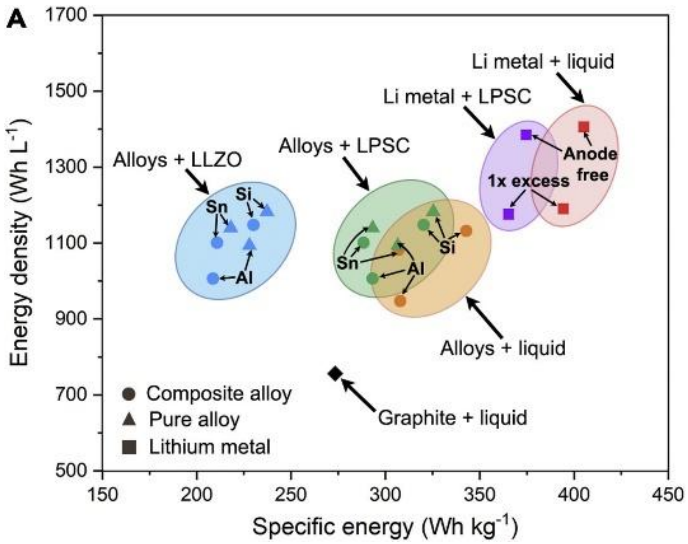

Fig. 1.3 The energy metrics comparison of alloy-based SSBs[20].

To address the challenges associated with lithium metal anodes, lithium alloys (such as Li-In, Li-Si, and Li-Al)[21–23] have been proposed as promising alternatives, owing to their enhanced safety and relatively high capacities. The charge-discharge mechanism of lithium alloys mainly involves alloying and dealloying processes ($xLi^+ + xe^- + M \rightleftharpoons Li_xM$). Among these alloy systems, Li-In has been the most widely employed. The potential of Li_xIn ($0 < x < 1$) is 0.62 V (*vs.* Li/Li^+)[24],

which is moderate enough to suppress electrolyte decomposition while simultaneously preventing the formation of lithium dendrites. [25,26]

Graphite possesses a relatively low potential toward lithium (below 0.20 V) and a theoretical capacity of 372 mAh g^{-1}, and it has already been successfully applied to commercial lithium-ion batteries with liquid electrolytes. In ASSLBs, graphite has also been effectively applied in the Li_2S-P_2S_5 system[27–30]. However, for many solid-state electrolytes, the very low potential at the graphite surface leads to reduction reactions, resulting in a large initial irreversible capacity of the cell. For example, although the Li_2S-GeS_2-P_2S_5 solid electrolyte exhibits high ionic conductivity, it is electrochemically incompatible with graphite and undergoes reduction[31].

1.2 Classification of Solid-state electrolyte

Solid-state electrolytes, also known as superionic conductors, are a new type of electrolyte. According to the composition classification of electrolytes, solid-state electrolytes include organic polymer solid-state electrolytes and inorganic solid-state electrolytes, as well as organic-inorganic composite solid-state electrolytes. Organic polymer solid-state electrolytes mainly include polyethylene oxide (PEO), polyacrylonitrile (PAN), etc. Inorganic solid-state electrolytes can be divided into various types based on their components, such as oxide electrolytes, sulfide electrolytes, and halide electrolytes, as well as hydride electrolytes. However, these pure single electrolytes often fail

to meet the requirements for the further development of solid-state batteries. Therefore, composite solid-state electrolytes have become a hot research topic. Composite solid-state electrolytes involve the combination of various inorganic solid-state electrolytes, the design of electrolyte-specific structures or morphologies, and the combination of inorganic solid-state electrolytes with organic polymer solid-state electrolytes. The following sections will provide a detailed discussion of the research status of polymer solid-state electrolytes, inorganic solid-state electrolytes, and composite solid-state electrolytes.

1.2.1 Polymer Solid-state Electrolytes

Polymer solid-state electrolytes have received widespread attention due to their lightweight, good viscoelastic properties, and excellent processability[32,33]. However, polymer solid-state electrolytes face two significant challenges, namely, low ionic conductivity at room temperature and insufficient mechanical strength[34]. Currently, polymer solid-state electrolytes can be mainly classified into two categories: (i) pure polymer electrolytes, consisting of a polymer matrix and dissolved lithium salts, and (ii) composite polymer electrolytes, in which inorganic fillers or secondary phases are introduced[35].

In 1979, Farrington[36] and co-workers first proposed using polymer-lithium salt composites as lithium-ion solid-state electrolytes for all-solid-state batteries. In pure polymer solid-state electrolytes, the ion migration mainly occurs in the amorphous region, while the unmodified

polymer matrix has high crystallinity, resulting in low ionic conductivity and making it difficult to apply in all-solid-state batteries. Therefore, most of the current research focuses on composite polymer electrolytes, which include polymer electrolytes and fillers inherent. composite polymer electrolytes have higher ionic conductivity, good flexibility, and good compatibility with the electrode[37]. Thus, research on composite solid-state electrolytes has attracted attention both domestically and internationally. Currently, the composite solid-state electrolytes mainly involve the addition of inorganic ceramic fillers into polymers. Commonly used polymer matrices include polyethylene oxide (PEO), polyacrylonitrile (PAN), polyvinyl chloride (PVC), etc.[32,38–40]. (**Fig. 1.5**) Ceramic fillers can be classified into two types: active fillers (such as Li_3N and $LiAlO_2$)[41,42] and inert fillers (Al_2O_3, SiO_2, MgO, etc.)[43–45]. Active fillers participate in lithium-ion conduction and can improve the overall lithium-ion conductivity. Inert fillers do not directly participate in lithium-ion conduction, but instead disrupt the orderliness of polymer multi-molecular segments, reduce crystallinity, and promote the ionization of lithium salt to enhance lithium-ion conductivity[46,47]. (**Fig 1.6**) However, the specific mechanism of ion migration in composite solid-state electrolytes is not yet fully understood.

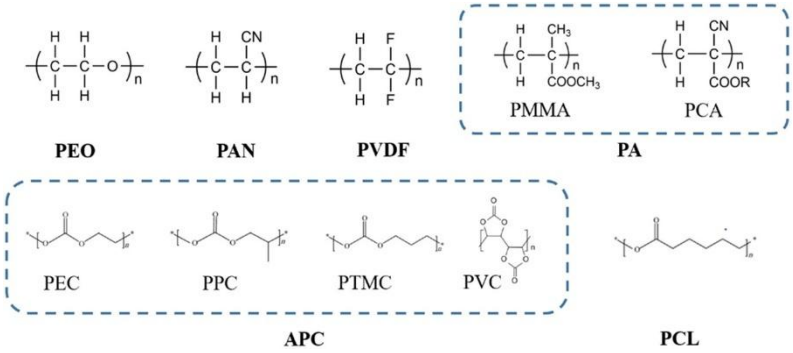

Fig. 1 .5 Structural diagram of common polymer matrices for polymer solid-state electrolyte.[32]

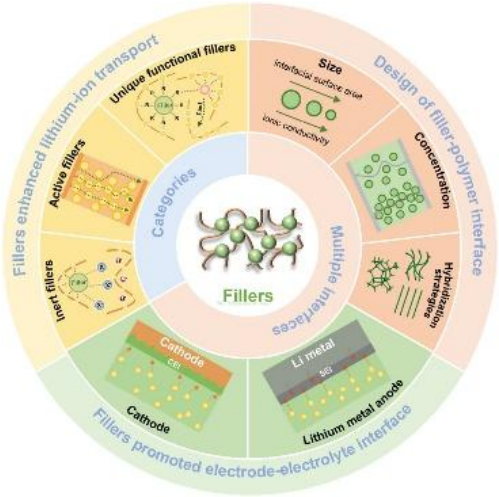

Fig. 1.6 Application of fillers for Polymer-based electrolyte in ASSLBs. [48]

1.2.2 Oxide Solid-State Electrolytes

Oxide-based solid electrolytes are characterized by their excellent chemical stability and mechanical robustness, making them promising candidates for all-solid-state batteries. Currently, various oxide solid-

state electrolytes have been developed, including NASICON-type, perovskite-type, and garnet-type.

NASICON-type solid-state electrolytes mainly include $Li_{1+x}Al_xTi_{2-x}(PO_4)_3$ (LATP) and $Li_{1+x}Al_xGe_{2-x}(PO_4)_3$ (LAGP). The advantages of these materials over other solid-state electrolytes are low cost, non-toxicity, air stability, and facile synthesis[49]. Liu *et al*[50]. prepared $Li_{1.4}Al_{0.4}Ti_{1.6}(PO_4)_3$ via a sol-gel method and achieved a high conductivity of 3.3×10^{-4} S cm^{-1} at room-temperature ionic with an activation energy of 0.30 eV, while maintaining excellent air stability. This study demonstrates that well-controlled microstructures and reduced grain-boundary resistance can substantially improve the conductivity and environmental robustness of NASICON-type electrolytes. However, NASICON-type electrolytes still suffer from poor compatibility with Li metal, which hinders their practical application in all-solid-state batteries[51].

The perovskite structure can be generally expressed as ABO_3, featuring high Li^+ conductivity and good thermal stability, but its synthesis usually requires high temperatures, resulting in significant energy consumption. The Li^+ conductivity of perovskite-type electrolytes is strongly related to the size of the constituent cations. For example, Manthiram *et al.*[52] substituted larger La^{3+} ions for Nd^{3+} in $Li_{0.34}Nd_{0.55}TiO_3$, achieving an increase of three orders of magnitude in room-temperature Li^+ conductivity compared with the parent material,

from 8.0×10^{-8} to 7.0×10^{-5} S cm^{-1}. In addition to ionic substitution, tuning the sintering atmosphere and doping to modify the crystal structure have also been demonstrated as effective strategies to enhance Li^+ conductivity. For instance, Lu *et al.*[53] synthesized quaternary $Li_{2x-y}Sr_{1-x-y}La_yTiO_3$ (x = 3y/4; y = 1/7, 2/7, 3/7, 1/2, 15/28, 4/7) solid electrolytes by a solid-state reaction method. X-ray diffraction results indicated that the structure transforms from cubic to tetragonal perovskite as the La^{3+} content increases. Electrochemical impedance spectroscopy showed that the conductivity initially increased but decreased when y exceeded a certain ratio. The $Li_{15/56}Sr_{1/16}La_{15/28}TiO_3$ electrolyte exhibited the highest room-temperature Li^+ conductivity of 4.5×10^{-4} S cm^{-1}, with very low electronic conductivity of 6.84×10^{-10} S cm^{-1} and an activation energy of 0.29 eV. Furthermore, Le *et al.*[54] synthesized aluminum-doped lanthanum lithium titanate (A-LLTO) powders with varying Li_2O contents using a simple citrate sol-gel method. The Li^+ conductivity of A-LLTO was found to be strongly influenced by the excess Li_2O content; when the excess reached 20%, the room-temperature conductivity achieved 3.17×10^{-4} S cm^{-1}. In addition, A-LLTO can serve as a protective layer to shield Li metal from oxygen, enabling Li-O_2 batteries to cycle stably for more than 100 cycles even under high current densities.

Furthermore, researchers have developed the garnet-type electrolyte $Li_7La_3Zr_2O_{12}$ (LLZO), which, in addition to its environmental stability and high Li^+ conductivity, exhibits much better stability against Li

metal than other types of oxide electrolytes. At room temperature, LLZO typically exists in a stable tetragonal phase with relatively low ionic conductivity, while at elevated temperatures it undergoes a phase transition to a stable cubic phase with significantly higher Li^+ conductivity. One important strategy to enhance the ionic conductivity is therefore to stabilize the highly conductive cubic phase at room temperature. (**Fig. 1.7**) Nevertheless, although LLZO shows good chemical stability against Li metal, internal defects within the material can still induce the formation of lithium dendrites, leading to short-circuiting. Consequently, improving the densification and enhancing the mechanical properties of LLZO-based electrolytes remain critical aspects of their development[55].

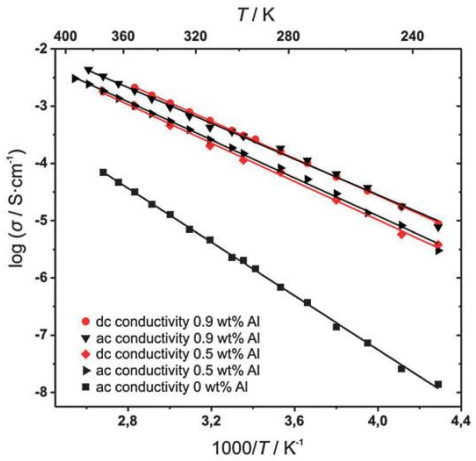

Fig. 1.7 Temperature dependence of the conductivity of LLZO samples with different Al contents[56].

Lastly, oxide-type electrolytes exhibit moderate to high ionic conductivity (10^{-4} – 10^{-3} S cm^{-1}) at room temperature and superior stability. However, their high processing temperature and interfacial limitations encourage more efforts to search for an alternative system.

1.2.3 Sulfide Solid-State Electrolytes

Sulfide-based solid electrolytes represent one of the most typical families of inorganic conductors, three representative systems have been established: the Li-P-S system, the $Li_{11-x}M_{2-x}P_{1+x}S_{12}$ (M = Ge, Sn, Si) system, and the Li_6PS_5X (X = I, Cl, Br) system. These materials exhibit excellent Li^+ conductivities on the order of 10^{-4}-10^{-3} S cm^{-1}. **Fig. 1.8** summarizes the comparative ionic conductivities of various high-conductivity sulfide-based solid electrolytes[57].

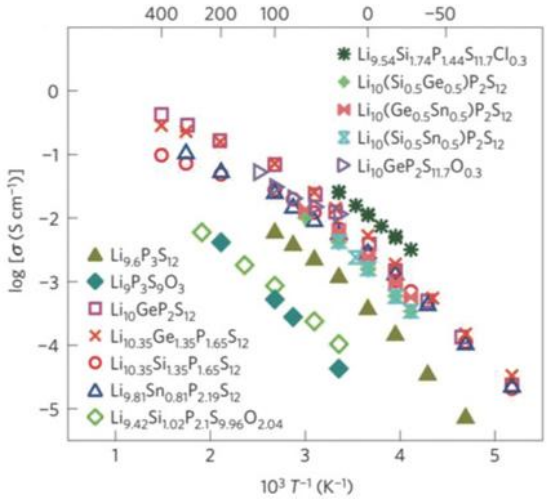

Fig.1.8 Comparison of high ionic conductivities of sulfide solid electrolytes at different temperatures[57].

Early Li-P-S solid electrolytes were typically prepared via solid-state sintering, which often resulted in inhomogeneous particle distribution and low room-temperature Li^+ conductivity. To address this limitation, various alternative synthesis processes have been developed. For instance, Liu *et al.* [58] dissolved Li_2S and P_2S_5 in a 3:1 molar ratio in anhydrous tetrahydrofuran (THF), successfully obtaining nanoporous Li_3PS_4. The nanoscale structure stabilizes the highly conductive β-Li_3PS_4 phase at room temperature, yielding a Li^+ conductivity of 1.6×10^{-4} S cm^{-1}, along with a wide electrochemical window of 5 V and excellent chemical stability against lithium metal. Phuc *et al.*[59] employed a solution-based method in which Li_2S and P_2S_5 were dissolved in ethyl acetate to form a Li_3PS_4 precursor, which was then decomposed at 160 °C to produce Li_3PS_4. This approach reduces interparticle surface resistance and achieves a room-temperature Li^+ conductivity of 3.3×10^{-4} S cm^{-1}. In addition, Chen *et al.* [60] incorporated Li_3PS_4 into a poly(ethylene oxide) (PEO) matrix to prepare a polymer composite electrolyte, PEO-2 vol% Li_3PS_4, where the PEO provides additional pathways for Li^+ migration, further enhancing the room-temperature ionic conductivity.

Despite their high conductivities comparable to liquid electrolytes, sulfide SSEs are highly sensitive to air and moisture and suffer from interfacial reactions with Li metal. These limitations highlight the need for alternative solid electrolytes for real-world applications.

1.2.4 Halide Solid-State Electrolytes

Halide-based solid electrolytes have attracted continuous attention since the 1930s[61]. Although the earliest materials showed very low Li^+ conductivity ($<10^{-7}$ S cm^{-1}), recent advances have led to halide electrolytes with high ionic conductivity, wide electrochemical stability windows, good air stability, and compatibility with high-voltage cathodes, making this family of materials highly promising for next-generation all-solid-state batteries. (**Fig. 1.9**)

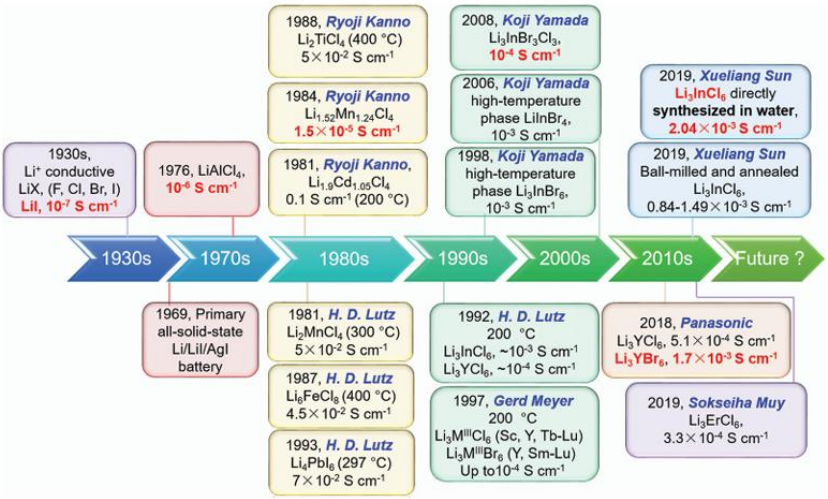

Fig. 1.9 A brief chronology of the development of halide SSEs for ASSLBs[62].

A representative classification of halide solid electrolytes is summarized in **Fig. 1.10**[63]. Recently, halide solid electrolytes (e.g., Li_3YX_6, X = Cl, Br) have emerged as highly promising candidates due to their relatively high Li^+ conductivity ($>10^{-4}$ S cm^{-1}), wide electrochemical stability window (> 4.0 V *vs* Li/Li^+), excellent air

stability, and good deformability[64–66].

Arumugam *et al.*[67] further extended the halide family to include halides with non-metallic central elements, such as the typical anti-perovskite Li_3OCl. The halides containing non-metallic elements (e.g., Li_3OCl) show relatively good stability against lithium metal but possess a narrower electrochemical stability window (2.55-3.0 V *vs.* Li/Li^+) [68]. However, metal-centered halides (e.g., Li_3YCl_6) are unstable in contact with lithium metal, yet they offer a wider electrochemical window (0.62-4.21 V *vs.* Li/Li^+)[69].

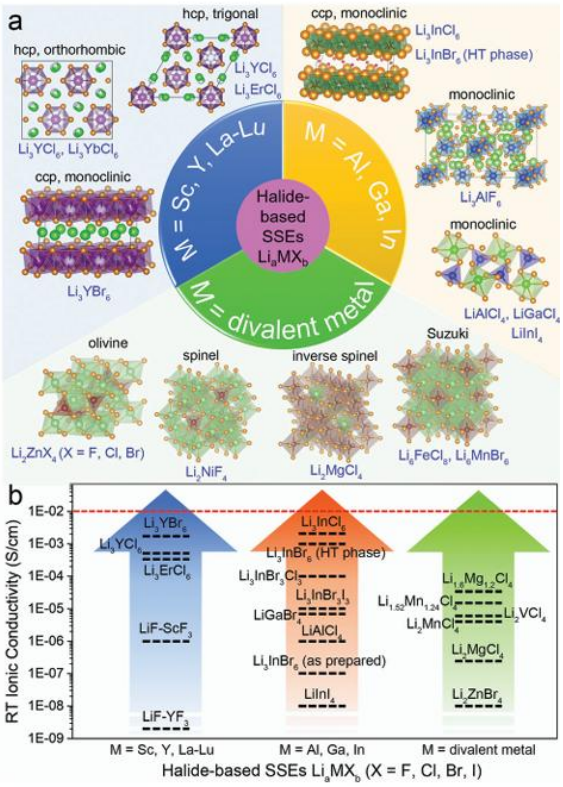

Fig.1.10 classification of existing halide electrolytes of Li_aMX_b.[63]

Overall, recent advances have greatly improved the Li^+ conductivity of halide solid electrolytes, with several compositions already reaching ~10^{-3} S cm^{-1} at room temperature. Beyond experimentally realized systems, computational studies continue to predict new halides with superionic transport. Given their structural diversity and the progress of theoretical design, halide solid electrolytes are expected to undergo rapid development toward superionic conductors in the future.

In summary, while polymer, oxide, sulfide, and halide solid electrolytes have each achieved significant progress, their intrinsic limitations, such as low room-temperature conductivity, interfacial instability, or complex processing, motivate the search for alternative systems. Among them, complex hydrides have recently emerged as promising candidates, combining high thermodynamic stability, light weight, and potential compatibility with Li/Na metal anodes.

1.3 Hydride Solid-State Electrolytes for Secondary Batteries

Secondary batteries are rechargeable systems based on reversible electrochemical reactions. Hydrides, due to their high theoretical hydrogen storage capacity, are considered highly promising solid-state hydrogen storage materials. They are typically composed of metal ions (alkali metals and alkaline earth metal ions such as Li^+, Na^+, and Mg^{2+}) and coordinating ions ($[BH_4]^-$, $[NH_2]^-$, $[AlH_4]^-$, $[AlH_6]^{3-}$, etc.). (**Fig. 1.11**)

Beyond their role in hydrogen storage, hydrides have recently attracted significant interest as solid-state electrolytes due to their excellent characteristics, including light weight, low grain boundary impedance, stability with lithium, good mechanical properties and low processing costs[70]. Currently, the hydride solid-state electrolyte family mainly includes $M(BH_4)_m$-based (M = Li, Na, Mg, etc.), $Li_2B_nH_n/Na_2B_nH_n$ (n = 10, 12)-based, and $LiCB_nH_{n+1}/NaCB_nH_{n+1}$ (n = 9, 11)-based solid-state electrolytes(**Fig. 1.11**)[71].

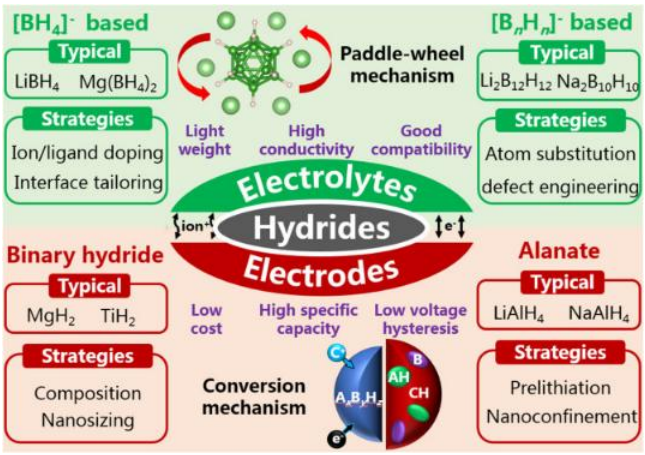

Fig. 1.11 Schematic illustration of applications of hydrides as electrode and electrolyte in SSBs. [71]

1.3.1 Origin and ionic conduction mechanism in $LiBH_4$

In 1979, Boukamp *et al.*[72] first reported Li_2NH, a lithium superionic conductor, with a room temperature ionic conductivity of 3.0×10^{-4} S cm^{-1}. It was the first fast lithium-ion conductor to be studied in the family of coordinated hydrides. However, the development of

coordinated hydride fast ion conductors was slow in the following years. It wasn't until 2007 that Masto *et al*. [73] discovered that $LiBH_4$ with a high-temperature hexagonal structure exhibited excellent ionic conductivity originating from the generation of a Li^+ metastable state located at an interstitial site surrounded by three Li^+ ions and three BH_4^- ions in the *a-b* plane, which reaches ~10^{-3} S cm^{-1} above 110 ℃ (**Fig. 1.12**). Subsequent ^{7}Li NMR studies revealed that Li^+ diffusion in the hexagonal phase occurs primarily within the *a-b* plane, where no $[BH_4]^-$ anions block the Li^+ migration pathways.[74] First-principles molecular-dynamics simulations further indicated that the reorientation of $[BH_4]^-$ anions facilitates Li^+ hopping between adjacent lattice sites, leading to fast ion transport. Cyclic-voltammetry measurements also showed that $LiBH_4$ remains electrochemically stable up to about 5.0 V (*vs* Li^+/Li), confirming its potential as a solid-state electrolyte for all-solid-state lithium batteries[75].

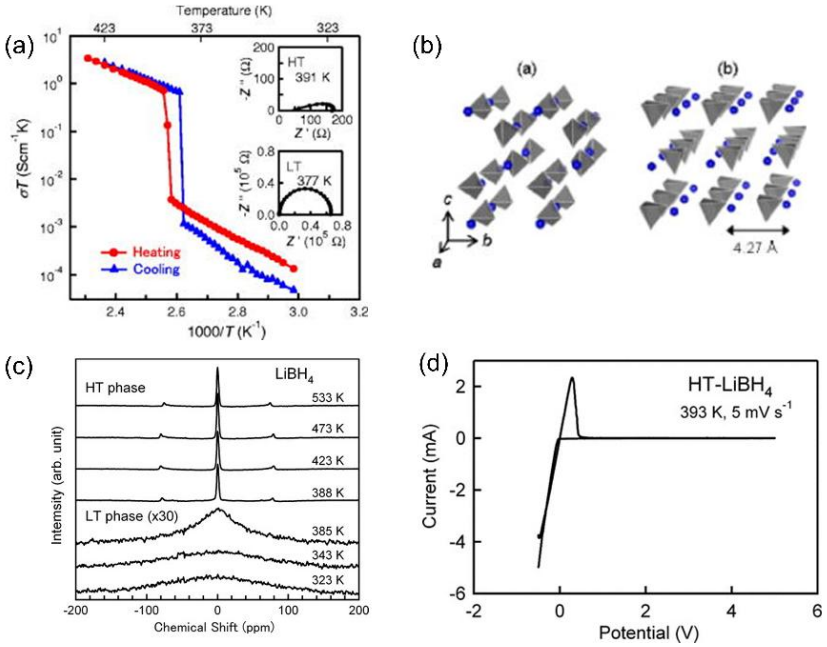

Fig. 1. 12 (a) Temperature dependence of conductivity of $LiBH_4$. **(b)** crystal structure of $LiBH_4$ of LT and HT phase. **(c)**^{7}Li NMR spectra of $LiBH_4$ at selected temperatures[73]. **(d)** Cyclic voltammograms of $LiBH_4$ sandwiched between the lithium and molybdenum electrodes taken at 390 K[75].

1.3.2 Optimization of $LiBH_4$ solid-state electrolytes

Although $LiBH_4$ shows good ionic conductivity performance over 120 ºC, the low ionic conductivity of its orthorhombic phase (~10^{-8} S cm^{-1}) results in poor room-temperature Li^+ transport. Current research on $LiBH_4$-based solid-state electrolyte materials mainly focuses on enhancing their room-temperature ionic conductivity. The most effective method include the anion/cation substitution, introduction of a second phase, and interfacial engineering. All of them aim to improve

lithium-ion mobility at lower temperatures to meet the practical demands of solid-state electrolytes.

Maekawa *et al.*[76] first stabilized the $LiBH_4$ high temperature phase to room temperature using lithium halide LiX (X = Cl, Br, and I). They found that the addition of LiX effectively reduced the activation energy of Li ion diffusion and the phase-transition temperature. Moreover, the larger the radius of the halide ions, the more significant the reduction of the phase transition temperature and the greater the enhancement of lithium-ion conductivity (**Fig. 1.13a)**. Among all compositions, the $3LiBH_4$-LiI solid solution exhibited the highest conductivity. The X-ray diffraction (XRD) pattern at room temperature proved the presence of the hexagonal $LiBH_4$ phase (**Fig. 1.13b**), and the ^7Li NMR spectra also revealed fast ionic dynamics (**Fig. 1.13c**). This improvement is attributed to the incorporation of the highly polarizable I^- anions into the $LiBH_4$ framework, which expands the lattice and weakens the electrostatic interactions between Li^+ and BH_4^-, thereby enhancing Li^+ mobility.

Sveinbjörnsson *et al.*[77] prepared $LiBH_4$-LiI solid solutions with LiI contents ranging from 6.25 to 50 % by ball milling and annealing. They observed that the phase-transition temperature decreased linearly with increasing LiI content (< 25%) and fell below room temperature when the content exceeded 12.5% (**e.g., Figure 1.13d**). At 40% LiI content, the $LiBH_4$-LiI solid solution exhibits ionic conductivity exceeding 1 ×

10^{-4} S cm^{-1} at 30 ºC (e.g., **Fig. 1.13e**). Myrdal *et al.*[78] combined density-functional theory (DFT) calculations and quasi-elastic neutron scattering (QENS) to investigate the mechanism of the $LiBH_4$-LiI solid solution system. They found a high concentration of Frenkel defects (5×10^{18} cm^{-3}) with a formation energy of 0.44 eV, and a migration barrier of only 0.20-0.30 eV. The high concentration of defects, the low formation energy, and the low diffusion energy barrier contribute to the excellent ionic conductivity of the $LiBH_4$-LiI solid solution system.

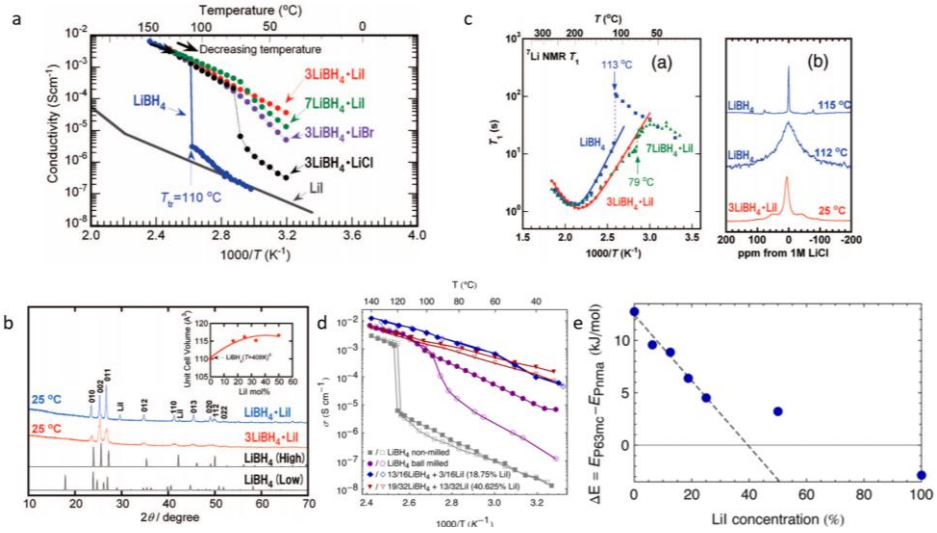

Fig. 1.13 (a) Temperature dependence conductivity of $LiBH_4$, LiI and $LiBH_4$-LiX, **(b)**XRD patterns of $LiBH_4$-LiI at room temperature, **(c)** ^{7}Li NMR spectra for $LiBH_4$ and $3LiBH_4$-LiI [76]. **(d)** LiI concentration dependence of phase-transition temperatures for the (1-x) $LiBH_{4+x}$LiI composite, (e) Temperature dependences of conductivity of $LiBH_4$ and $LiBH_4$-LiX composite[77].

Beyond halide substitution, introducing $[NH_2]^-$ ionic groups has also

effectively enhanced the conductivity of $LiBH_4$[79,80]. Matsuo *et al.*[80] synthesized the $Li_2(BH_4)(NH_2)$ and $Li_4(BH_4)(NH_2)_3$, which both exhibited a high room-temperature ionic conductivity of 2.0×10^{-4} S cm^{-1}, four to five orders of magnitude higher than those of pristine $LiBH_4$ and $LiNH_2$ (e.g., **Fig. 1.14a**). The ion diffusion activation energies of $Li_2(BH_4)$ (NH_2) and $Li_4(BH_4)$ $(NH_2)_3$ are 0.56 and 0.26 eV, respectively, confirming fast ion conduction characteristics. Meanwhile, the ^7Li NMR spectra of both materials display obvious motional narrowing at room temperature, indicating excellent lithium-ion dynamics. In addition, the ^7Li NMR spectra consists of Gaussian (representing low ionic conductivity) and Lorentzian (representing high ionic conductivity) parts (**Fig. 1. 14b**). Structure analysis (e.g., **Fig. 1. 14c**) reveals abundant Li vacancies: 18 Li (1) and 18 Li (2) vacancies in $Li_2(BH_4)$ $(NH_2)_3$; 12 Li (1), 12 Li (2), and 8 Li (3) vacancies in $Li_4(BH_4)$ $(NH_2)_3$. The smaller Li(2) sites (0.09 nm) in $Li_2(BH_4)(NH_2)$ restrict Li^+ migration, explaining its slightly lower conductivity compared to $Li_2(BH_4)(NH_2)_3$, whose larger vacancy network (0.11-0.17 nm) provides more efficient transport pathways.

Overall, introducing $[NH_2]^-$ ions increases Li^+ vacancies and lattice polarizability while enhancing anion dynamics, collectively improving the ionic conductivity of amide-borohydride solid electrolytes.

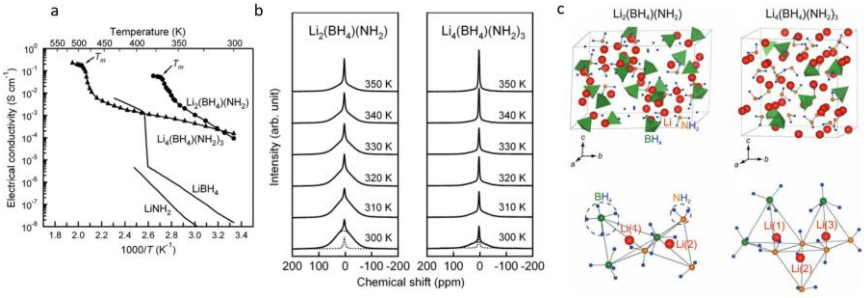

Fig. 1. 14 (a) Temperature dependences conductivity of $LiBH_4$, $LiNH_2$, $Li_2(BH_4)(NH_2)$ and $Li_4(BH_4)(NH_2)_3$, **(b)** ^7Li NMR spectra for $Li_2(BH_4)(NH_2)$ and $Li_4(BH_4)(NH_2)_3$, **(c)** Crystal structures of $Li_2(BH_4)(NH_2)$ and $Li_4(BH_4)(NH_2)_3$[81].

The introduction of cations has also proved to be an effective strategy for improving the ionic conductivity in $LiBH_4$. Ley *et al.* [82,83] prepared $LiM(BH_4)_3Cl$ (M = La, Ce, Gd) materials by high-energy ball milling, achieving ionic conductivities of 2.3×10^{-4}, 1.0×10^{-4}, and 3.5×10^{-4} S cm^{-1} at 20 ºC, respectively. They are four orders of magnitude higher than that of $LiBH_4$ under the same conditions. Nguyen *et al.*[84] further determined that lithium-ion diffusion activation energies are 0.40, 0.21, and 0.32 eV for these compounds ($LiM(BH_4)_3Cl$ (M = La, Ce, Gd)), respectively, confirming their fast ion conduction properties. Among them, $LiCe(BH_4)_3Cl$ mixed with carbon exhibited the stability against Li-ln alloy with an electrochemical window reaching 7.0 V, while the absence of further validation makes it difficult to confirm whether this reflects a true electrochemical window. In the crystal structure of the $LiM(BH_4)_3Cl$ (M = La, Gd, and Ce) compounds, three Cl atoms and three $[BH_4]^-$ groups are coordinated to each lanthanide atom to form an

octahedral coordination environment (**Fig. 1.15(a)**). $LiCe(BH_4)_3Cl$ crystalline in the cubic crystal system $I\bar{4}3m$, a = 11.7204(2) Å, and its framework consists of the lithium cations and tetranuclear anion clusters, $[Ce_4Cl_4(BH_4)_{12}]^{4-}$, with Ce-Cl and Ce-B distances of 2.961(6) and 2.74(2) Å, respectively. Combined analysis using synchrotron radiation powder X-ray diffraction (SR-PXD) data, powder neutron diffraction (PND) data, and DFT optimization demonstrated that Li occupies 2/3 d of 12d Wyckoff site in the $LiCe(BH_4)_3Cl$ structure[82]. Lee *et al.*[85] further found that the $LiCe(BH_4)_3Cl$ structure also contains a stable 6d site, which plays an important role in Li-ionic conductivity. These sites are shown in **Fig. 1.15(b).** In a related study, Roedern *et al*.[86] reported the synthesis, structure, and ion transport of the bimetallic borohydrides $LiY(BH_4)_4$ and $NaY(BH_4)_4$. Compared with their precursors, $LiY(BH_4)_4$ exhibits a room-temperature ionic conductivity of 1.26×10^{-6} S cm^{-1}, while $NaY(BH_4)_4$ reaches 6.92×10^{-7} S cm^{-1}. The authors attribute the improvement to the $[Y(BH_4)_4]^-$ complex anion framework and the pronounced unit-cell expansion (≈14% for the Li compound and ≈7.5% for the Na analogue), which likely widens Li^+ diffusion pathways and lowers migration barriers.

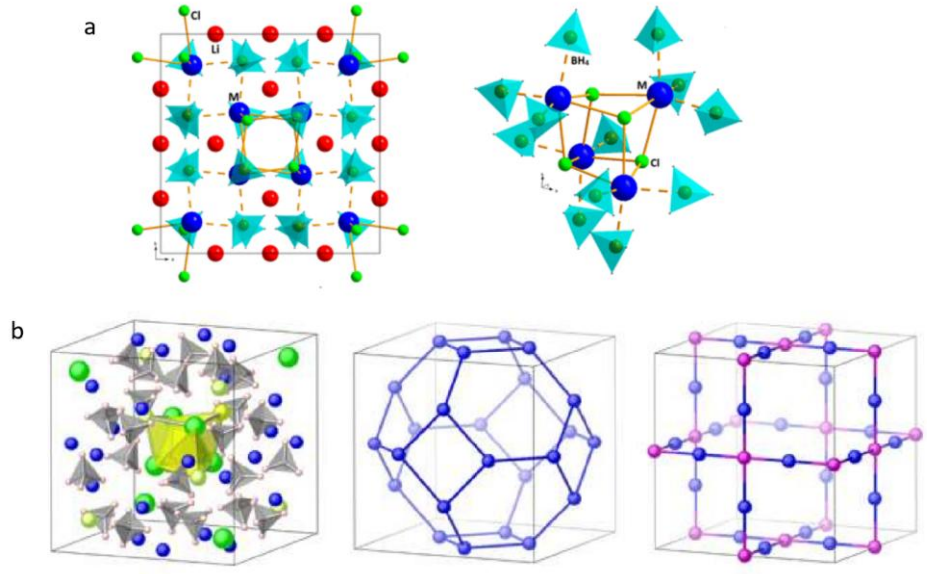

Fig. 1.15 (a) Schematic diagram of the crystal structure of $LiM(BH_4)_3Cl$ (M = La, Ce, Gd) and Isolated tetranuclear anionic clusters $[M_4Cl_4(BH_4)_{12}]^{4-}$ (M = La or Gd) with a distorted cubane M_4Cl_4 core[83]. **(b)** Schematic diagram of crystal structure of $LiCe(BH_4)_3Cl$ with Li, Ce, and Cl colored in blue, yellow, and green, respectively, 12d Wyckoff sites and their three-dimensional network and combination of 12d (in blue) and 6b (in magenta) sites and their three-dimensional network[85].

The incorporation of a second phase into the $LiBH_4$ lattice has also been explored for conductivity improvement. Zhang *et al.*[87] introduced ammonia (NH_3) into $LiBH_4$ to form the molecular complex $Li(NH_3)_nBH_4$ ($0 < n \leq 1$), introducing partial occupation of Li sites, leading to the formation of lithium vacancies within the lattice. Meanwhile, Li^+ ions in the local environment can migrate into adjacent vacant sites via a vacancy-mediated hopping mechanism, thereby

facilitating long-range ionic transport. (**Fig. 1.16**). As a result, Li (NH_3) BH_4 achieved a Li^+ conductivity of 2.21 × 10^{-3} S cm^{-1} at 40 °C, which represents a substantial improvement compared to pristine $LiBH_4$.

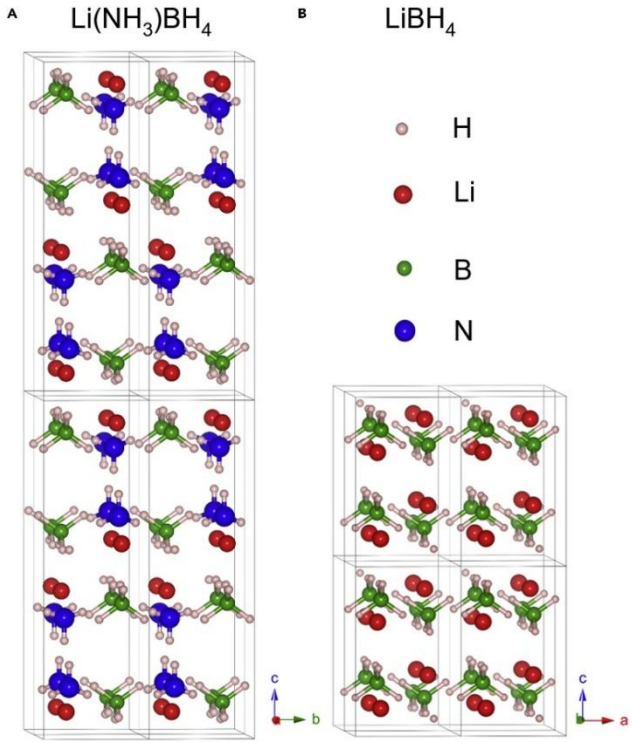

Fig. 1.16 Structure of Li (NH_3) BH_4[87].

Grinderslev *et al.*[88] synthesized a methylamine-lithium borohydride complex ($LiBH_4 \cdot CH_3NH_2$). This compound crystallizes in a monoclinic layered structure (space group *P21/c*), where CH_3 groups separate continuous $LiBH_4$ layers and create interlayer voids that act as fast-ion transport channels. At room temperature, $LiBH_4 \cdot CH_3NH_2$ exhibits a Li^+ conductivity of 1.24 × 10^{-3} S cm^{-1} with negligible electronic conduction and a stability window of ~2.1 V (*vs* Li^+/Li) and shows compatibility

with TiS_2 cathode in all-solid-state lithium batteries at 30 ℃, demonstrating the strong potential of amine-ligated borohydrides as solid electrolytes.

Interfacial engineering is also a promising approach to improve the ionic conductivity of $LiBH_4$-based solid electrolytes. Blanchard et al.[89] achieved a lithium-ion conductivity of 1.0×10^{-4} S cm^{-1} at 40 ºC by confining $LiBH_4$ with mesoporous SiO_2 MCM-41 (**Fig. 1.17)**, nearly three orders of magnitude higher than that of bulk $LiBH_4$ at the same temperature. The activation energy decreased from 0.69 and 0.53 eV (for the low- and high-temperature phases, respectively) to 0.43 eV. Choi *et al.*[90] further systematically investigated the interfacial contribution by comparing composites of $LiBH_4$ with fumed SiO_2 and Al_2O_3 prepared via high-energy ball milling. They found that both types of oxides effectively promoted interfacial ionic transport, with $LiBH_4$-Al_2O_3 composites reaching a conductivity of 2.0×10^{-4} S cm^{-1} at room temperature, surpassing that of the SiO_2 system. This enhancement was attributed to the formation of an interfacial amorphous layer and the partial stabilization of the hexagonal $LiBH_4$ phase induced by surface interactions, which demonstrated the existence of the interfacial effect. Based on these findings, Lu *et al.*[91] combined halide substitution and interfacial effects by fabricating $Li_4(BH_4)_3I$-SBA-15 via melt infiltration (**Fig. 1.17(d)**). The resulting material reached an ionic conductivity of 2.5×10^{-4} S cm^{-1} at 35 ºC and maintained a wide electrochemical stability window up to 5.0 V (*vs* Li^+/Li). More recently,

Zeng *et al.*[92] showed that nanoconfinement of $LiBH_4$ into mesoporous Al_2O_3 could stabilize the hexagonal phase near ambient temperature, achieving a conductivity of 3.2×10^{-4} S cm^{-1} at 75 ºC and showing good interfacial compatibility with Li metal.

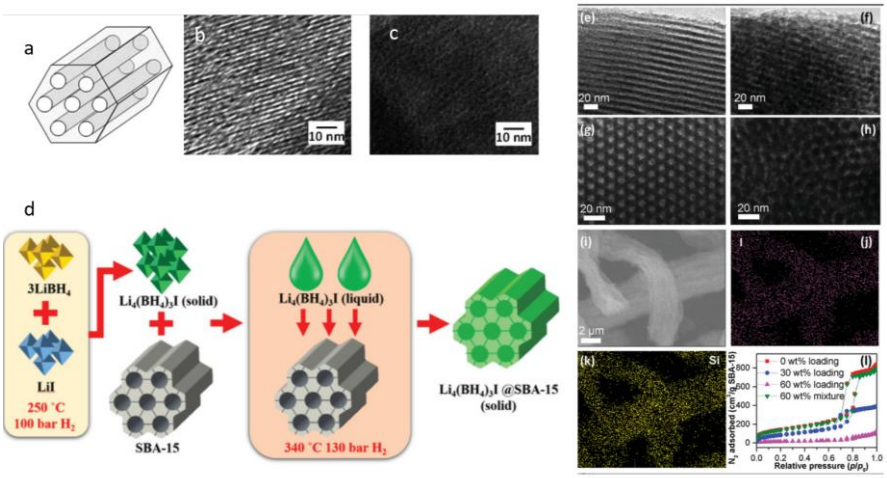

Fig. 1.17 (a) Schematic representation of MCM-41, TEM of MCM-41 **(b)** before and **(c)** after melt infiltration **(d)** A schematic diagram of the preparing process of $Li_4(BH_4)_3I$ in SBA-15, TEM of **(e,g)** SBA-15 and (f,h) $Li_4(BH_4)_3I$-SBA-15; **(i–k)** SEM-EDS mapping images of $Li_4(BH_4)_3I$-SBA-15; **(l)** nitrogen adsorption isotherms of samples[93, 90].

Beyond oxides, interfacial coupling with two-dimensional materials such as MoS_2 can also promote ion mobility. Liu *et al.*[94] reported that coupling $LiBH_4$ with MoS_2 layers enhances the ionic conductivity to ~10^{-4} S cm^{-1} at room temperature, attributed to strong interfacial coupling that induces Li^+ redistribution and creates interlayer diffusion pathways. Wu *et al.*[95] demonstrated that defect-rich BN induces tetrahedral deformation of BH_4^-, weakening Li-H interactions and

promoting subsurface Li^+ migration. The $LiBH_4$-10 wt% BN composite exhibits a Li^+ conductivity of 1.2×10^{-4} S cm^{-1} at 25 °C and an electrochemical window of 5.0 V (*vs* Li^+/Li). The $Li|LiBH_4{-}BN|LiFePO_4$ all-solid-state battery delivered stable cycling and high capacity retention, confirming the interfacial and structural benefits of BN modification (**Fig. 1.18**). Other 2D materials, g-C_3N_4, further enhance interfacial polarization and mechanical stability. For instance, Hu *et al.*[96] prepared $Li_{16}(BH_4)_{13}I_3$g-C_3N_4, which reached 3.15×10^{-4} S cm^{-1} at 30 °C and achieved an excellent long-term cycling stability in Li||Li symmetric batteries.

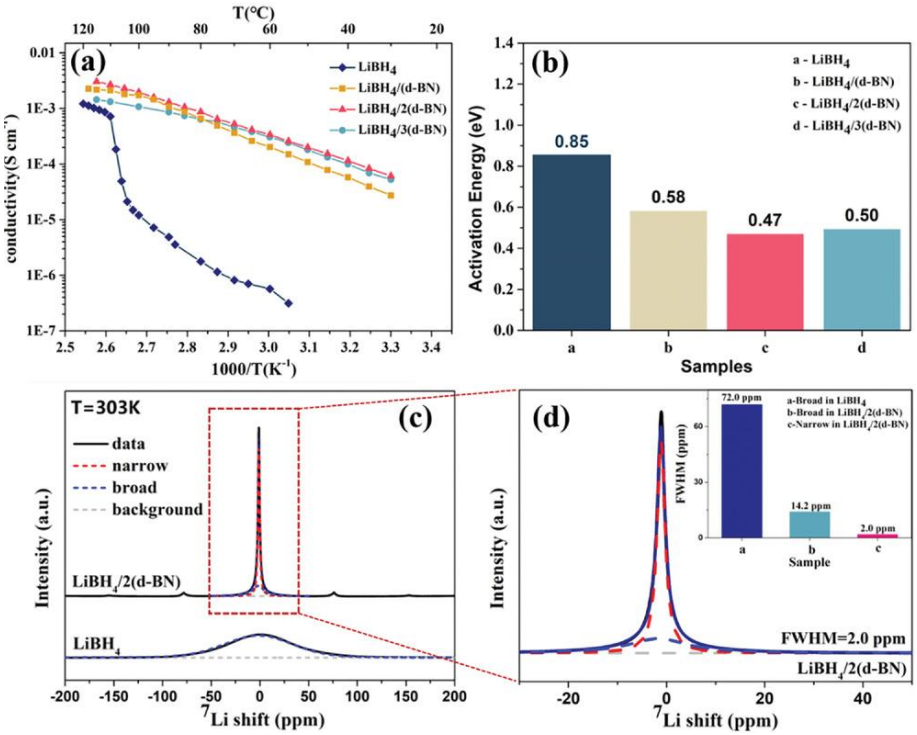

Fig. 1.18(a) Temperature-dependent conductivities of various $LiBH_4$/d-BN composites and pristine $LiBH_4$; **(b)** Activation energy of $LiBH_4$/d-BN composites and $LiBH_4$. **(c) and (d)** Li solid-state NMR spectra of $LiBH_4$/2(d-BN) and $LiBH_4$ at 303 K[95].

Nevertheless, the room-temperature ionic conductivity of most borohydrides remains relatively low, and their interfacial stability with Li/Na metal is not yet fully understood. Therefore, this thesis aims to address these challenges through rational composite design.

1.3.3 $[B_nH_n]^{2-}$ anion-based electrolytes (n = 10, 12)

$Li_2B_nH_n$/$Na_2B_nH_n$ (n = 10, 12) hydrides are intermediate products obtained after the dehydrogenation of corresponding MBH_4 (M= Li,

Na). In their nearly spherical $[B_nH_n]^{2-}$ framework, the B-B bonds exhibit higher bond energy, which provides greater chemical stability compared to MBH_4. They are not reactive toward moisture or thermal decomposition at high temperature, but tend to form stable crystalline hydrates with water[97]. **Fig. 1.19** illustrates the geometric structures of $[B_{10}H_{10}]^{2-}$ and $[B_{12}H_{12}]^{2-}$, presenting distinctive cage-like structures. $Na_2B_{12}H_{12}$ adopts an ordered monoclinic crystal structure at room temperature, and it transforms into a body-centered cubic (bcc) phase at 256 ℃ with numerous vacancies and off-center sub-lattices, enabling fast sodium ion conduction[106]. Similarly, $Na_2B_{10}H_{10}$ undergoes a transition to a disordered face-centered cubic (fcc) phase at 87 ºC, exhibiting a Na ion conductivity of 0.01 S cm^{-1} at 110 ºC, which is two orders of magnitude higher than that of ordered $Na_2B_{10}H_{10}$ and $Na_2B_{12}H_{12}$ under the same conditions[98]. In contrast, the transition temperatures of $Li_2B_{10}H_{10}$ and $Li_2B_{12}H_{12}$ are much higher, exceeding 600 K, limiting their ionic conductivity at room temperature[99]. Nevertheless, Joseph *et al.*[100] reported that ball-milled $Li_2B_{12}H_{12}$ exhibited an ionic conductivity of 3.1×10^{-4} S cm^{-1} at room temperature, with an electrochemical stability window of 6.0 V (*vs* Li^+/Li). This exceptional performance is attributed to the presence of the borane-related impurities[101]. Although these *closo*-borate hydrides exhibit high conductivity after the order-disorder transition, their transition temperatures remain relatively high. To overcome this issue, introducing both cations and anions has been shown to effectively lower

the transition temperature. He *et al.*[102] synthesized a bimetallic $LiNaB_{12}H_{12}$ material, which displayed a reduced transition temperature (488 K) compared with the single-metal $Li_2B_{12}H_{12}$ (615 K) and $Na_2B_{12}H_{12}$ (529 K), achieving an ionic conductivity of 0.79 S cm^{-1} at 550 K, outperforming single-metal $Li_2B_{12}H_{12}$ and $Na_2B_{12}H_{12}$. Yoshida *et al.*[103] prepared a composite electrolyte $Na_2B_{10}H_{10}$-$Na_2B_{12}H_{12}$ by ball milling and found that the electrolyte with optimal composition (1:3 molar ratio) exhibited a Na-ion conductivity of 3.16×10^{-4} S cm^{-1} at 303K.

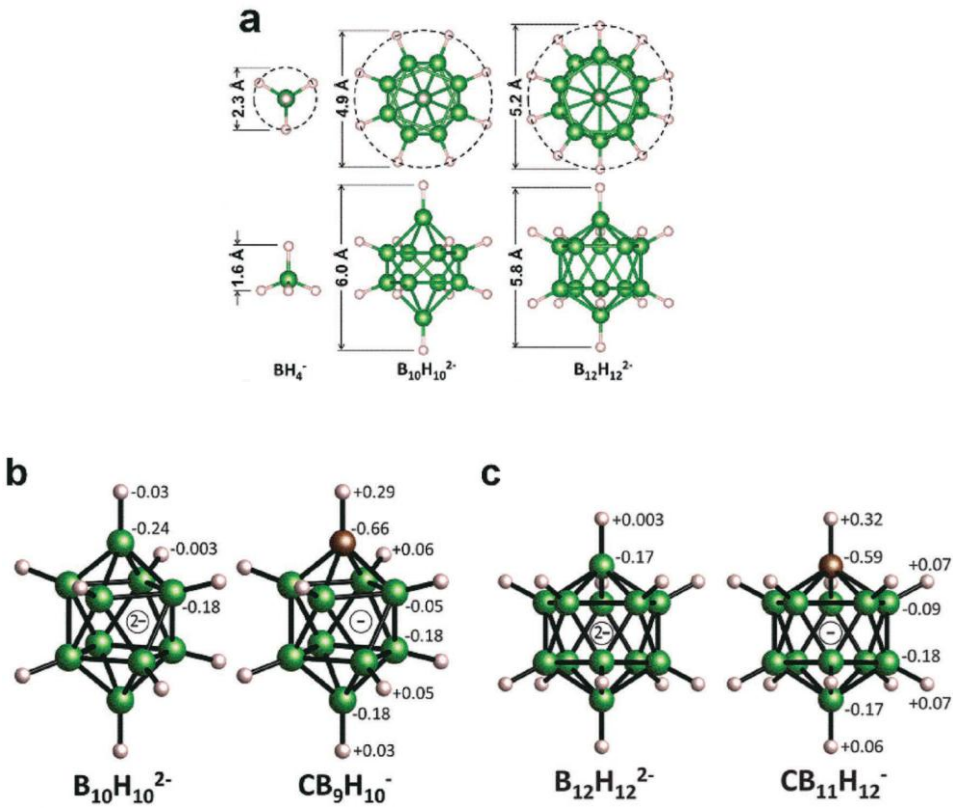

Fig. 1.19 The structures of $[BH_4]^-$, $[B_{10}H_{10}]^{2-}$, $[B_{12}H_{12}]^{2-}$, $[CB_9H_{10}]^-$ and $[CB_{11}H_{12}]^-$ anions[104].

Furthermore, He *et al.*[105] successfully synthesized a novel sodium-based solid electrolyte, $Na_3NH_2B_{12}H_{12}$, by high-energy ball milling $NaNH_2$ with $Na_2B_{12}H_{12}$. As shown in **Fig. 1.20(a)**, the crystal structure of $Na_3NH_2B_{12}H_{12}$ preserved the stable boron-cage framework, showing the ionic conductivity of 1.0×10^{-4} S cm^{-1} at 372 K, which increases with temperature following Arrhenius behavior (**Fig. 1.20(c)**). When $Na_3NH_2B_{12}H_{12}$ was employed as the solid electrolyte in $Na|Na_3NH_2B_{12}H_{12}|Na_3NH_2B_{12}H_{12}/TiS_2$ all-solid-state sodium battery, it exhibited stable charge-discharge performance (**Fig. 1.20(d)**). It also

displayed a wide electrochemical stability window of approximately 10.0 V at 10 mV s^{-1} (*vs* Na^+/Na) (**Fig. 1.20(b)**), while the high scan rates decrease the detection of electrolyte reduction or oxidation[106]. Therefore, the real stability windows are often narrower than experimentally observed. Braun *et al.* reveal that the slow kinetics at room temperature easily masked the onset of decomposition under standard electrochemical measurement conditions[107]. The ionic conductivity of $NaCB_{11}H_{12}$[108], $Na_3NH_2B_{12}H_{12}$[109], and $NaCB_9H_{10}$[110] are higher than those of precursors $NaNH_2$ and $Na_2B_{12}H_{12}$. These findings highlight that anion substitution is an effective strategy to tailor the crystal structure and ion transport properties of borohydride-based materials, thus offering a viable route for designing high-conductivity solid electrolytes.

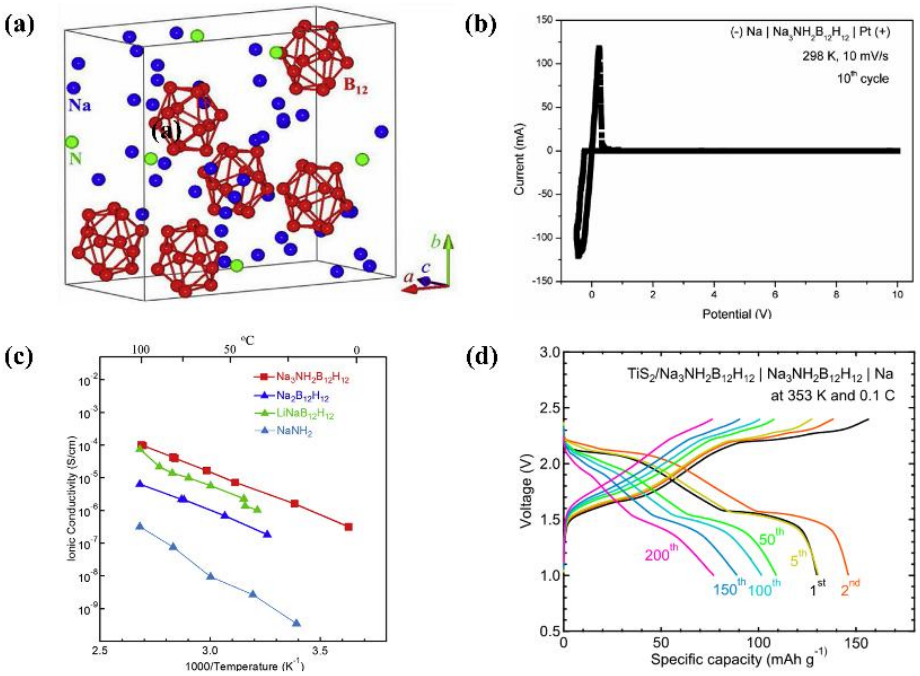

Fig.1.20 (a) Crystal structure (*Pna2₁*) of $Na_3NH_2B_{12}H_{12}$, **(b)** Cyclic voltammogram of $Na_3NH_2B_{12}H_{12}$. **(c)** Temperature-dependent ionic conductivity of $Na_3NH_2B_{12}H_{12}$. **(d)** Charge and discharge curve of all-solid-state Na | $Na_3NH_2B_{12}H_{12}$|TiS_2/$Na_3NH_2B_{12}H_{12}$ at 353 K.

1.4 Objectives of this thesis

Conventional liquid electrolytes, due to their flammability, cannot meet the requirements for developing batteries with high energy density and high safety. Complex metal borohydrides have received significant interest as solid-state electrolytes for next-generation lithium and sodium batteries. While most borohydrides have low room-temperature ionic conductivity ($<10^{-8}$ S cm^{-1}). Previous studies have demonstrated that the incorporation of inorganic oxides, like Al_2O_3 and SiO_2, into $LiBH_4$ via molten infiltration can significantly enhance its ionic conductivity [89,111–113]. Such improvements are generally attributed to the formation of interfacial regions that facilitate Li^+ transport and the partial stabilization of the high-conductivity phase[89]. Despite its proven effectiveness, molten infiltration suffers from several limitations, including the need for high-temperature equipment, hydrogen pressure, extended synthesis time, and high processing costs. These factors hinder its applicability for industrial production of all-solid-state battery systems. In contrast, mechanical ball milling offers a simple, energy-efficient, and scalable approach for preparing composite electrolytes without the need for melt processing or solvent-based methods[114]. The objective of this doctoral thesis is to enhance the ionic conductivity of borohydride-based materials by facile mechanical ball-milling, and to investigate their application as solid-state electrolytes in secondary metal batteries.

In **Chapter 3**, we investigate the influence of zeolite on the ionic conductivity of $LiBH_4$. The selection of zeolite is motivated by its exceptionally high surface area, low cost, and widespread application in catalysis[115]. We hypothesize that its three-dimensional network structure can effectively contact with $LiBH_4$ and promote the formation of efficient Li^+ transport pathways. Compared with other inorganic oxides, zeolite is expected to deliver a more pronounced enhancement in ionic conductivity due to its unique porous architecture and structural compatibility with $LiBH_4$. Furthermore, when employed as a component of solid-state electrolytes in lithium-metal batteries, zeolite offers high chemical stability and intrinsic electronic insulating properties, which can effectively suppress the growth of lithium dendrites and thereby enable improved electrochemical performance.

Based on the confirmed positive impact of zeolite on $LiBH_4$, we extended the application of zeolite to sodium-based borohydrides in **Chapter 4**. Given the low ionic conductivity of $NaBH_4$, $Na_2B_{12}H_{12}$ with a cage-like structure, was selected as the research material, and zeolite was incorporated to form composite electrolytes. This approach enables us to evaluate the role of zeolite in enhancing the ionic conductivity of large-structure borohydrides. We hypothesize that zeolite can significantly improve the ionic conductivity of $Na_2B_{12}H_{12}$ through its porous architecture and favorable interfacial interactions. Moreover, when utilized as solid-state electrolytes in sodium-metal batteries, these zeolite-containing composites are expected to exhibit superior

electrochemical performance, analogous to their lithium-based counterparts.

Chapters 3 and **4** have demonstrated that adding zeolite, a three-dimensional inorganic framework, into $LiBH_4$ and $Na_2B_{12}H_{12}$ can markedly enhance their ionic conductivity and electrochemical stability. Previous studies have reported that combining $LiNH_2$ with $LiBH_4$ yields composite electrolytes with significantly improved conductivity[116]. Therefore, in **Chapter 5**, we investigate the interfacial effects of $LiBH_4$-$LiNH_2$ composites with two-dimensional BN, a material characterized by a high surface area and intrinsically low electronic conductivity[117–119]. This study aims to couple the advantages of chemical modification with the structural features of two-dimensional materials to achieve superior ionic conductivity and electrochemical performance.

Current research on ionic substitution of cations and anions in borohydride-based solid electrolytes has so far mainly focused on inorganic metal borohydrides. However, the use of organic borohydrides has remained largely unexplored, despite their potential to offer new structural and dynamic flexibility through cation substitution. In **Chapter 6**, we try to integrate a series of R_4NBH_4 into $LiBH_4$, to figure out the relationship between cation alkyl-chain length, crystal structure, melting point, and ionic transport.

Through these systematic studies, the thesis aims to develop high-

performance borohydride-based solid-state electrolytes and broaden their practical feasibility in Li/Na ion batteries, providing innovative ideas and approaches for their future application in all-solid-state batteries.

Reference

1. Ramkumar, M. S. *et al.* Review on Li-Ion Battery with Battery Management System in Electrical Vehicle. *Adv. Mater. Sci. Eng.* **2022**, 3379574 (2022).
2. Wen, J., Yu, Y. & Chen, C. A Review on Lithium-Ion Batteries Safety Issues: Existing Problems and Possible Solutions. *Mater. Express* **2**, 197–212 (2012).
3. Zhao, C. *et al.* Solid-State Sodium Batteries. *Adv. Energy Mater.* **8**, 1703012 (2018).
4. Dong, X. et al. Solid-state electrolytes for sodium metal batteries: recent status and future opportunities. *Adv. Funct. Mater.* **34**, 2213584 (2024).
5. Hausbrand, R. *et al.* Fundamental degradation mechanisms of layered oxide Li-ion battery cathode materials: Methodology, insights and novel approaches. *Mater. Sci. Eng. B* **192**, 3–25 (2015).
6. Schmaltz, T. *et al.* A Roadmap for Solid-State Batteries. *Adv. Energy Mater.* **13**, 2301886 (2023).

7. Ma, M. *et al.* A review of all-solid-state electrolytes for lithium batteries: high-voltage cathode materials, solid-state electrolytes and electrode–electrolyte interfaces. *Mater. Chem. Front.* **7**, 1268–1297 (2023).

8. Li, S., Zhu, K., Zhao, D., Zhao, Q. & Zhang, N. Porous $LiMn_2O_4$ with Al_2O_3 coating as high-performance positive materials. *Ionics* **25**, 1991–1998 (2019).

9. Huang, Y. *et al.* Mg-Pillared $LiCoO_2$: Towards Stable Cycling at 4.6 V. *Angew. Chem.* **133**, 4732–4738 (2021).

10. Dong, S. *et al.* Enhanced Cathode Performance: Mixed Al_2O_3 and LiAlO2 Coating of $Li_{1.2}Ni_{0.13}Co_{0.13}Mn_{0.54}O^2$. *ACS Appl. Mater. Interfaces* **12**, 38153–38162 (2020).

11. Kim, J. et al. Effect of copper-doping on $LiNiO_2$ positive electrode for lithium-ion batteries. *J. Electrochem. Soc*. **167**, 090540 (2020).

12. Karthickprabhu, S. *et al.* Electrochemical and cycling performance of neodymium (Nd^{3+}) doped $LiNiPO_4$ cathode materials for high voltage lithium-ion batteries. *Mater. Lett.* **237**, 224–227 (2019).

13. Liang, J. *et al.* Recent progress on solid-state hybrid electrolytes for solid-state lithium batteries. *Energy Storage Mater.* **21**, 308–334 (2019).

14. Unemoto, A. *et al.* Stable Interface Formation between TiS_2 and $LiBH_4$ in Bulk-Type All-Solid-State Lithium Batteries. *Chem. Mater.* **27**, 5407–5416 (2015).

15. Nagao, M. *et al.* In situ SEM study of a lithium deposition and dissolution mechanism in a bulk-type solid-state cell with a Li_2S–P_2S_5 solid electrolyte. *Phys. Chem. Chem. Phys.* **15**, 18600–18606 (2013).

16. Wan, H. *et al.* Critical interphase overpotential as a lithium dendrite-suppression criterion for all-solid-state lithium battery design. *Nat. Energy* **8**, 473–481 (2023).

17. Cheng, E. J., Sharafi, A. & Sakamoto, J. Intergranular Li metal propagation through polycrystalline $Li_{6.25}Al_{0.25}La_3Zr_2O_{12}$ ceramic electrolyte. *Electrochimica Acta*. **223**, 85–91 (2017).

18. Kazyak, E. *et al.* Li Penetration in Ceramic Solid Electrolytes: Operando Microscopy Analysis of Morphology, Propagation, and Reversibility. *Matter.* **2**, 1025–1048 (2020).

19. Lee, J. *et al.* Temperature dependence of lithium anode voiding in argyrodite solid-state batteries. *ACS Appl. Mater. Interfaces* **13**, 31634–31644 (2021).

20. Lewis, J. A., Cavallaro, K. A., Liu, Y. & McDowell, M. T. The promise of alloy anodes for solid-state batteries. *Joule* **6**, 1418–1430 (2022).

21. Wen, C. J. & Huggins, R. A. Chemical diffusion in intermediate phases in the lithium-silicon system. *J. Solid State Chem.* **37**, 271–278 (1981).

22. Rao, B. M. L., Francis, R. W. & Christopher, H. A. Lithium-Aluminum Electrode. *J. Electrochem. Soc.* **124**, 1490 (1977).

23. Han, S. Y. *et al.* Porous Metals from Chemical Dealloying for Solid-State Battery Anodes. *Chem. Mater.* **32**, 2461–2469 (2020).

24. Takada, K., Aotani, N., Iwamoto, K. & Kondo, S. Solid state lithium battery with oxysulfide glass. *Solid State Ion.* **86–88**, 877–882 (1996).

25. Seino, Y., Ota, T. & Takada, K. High rate capabilities of all-solid-state lithium secondary batteries using $Li_4Ti_5O_{12}$-coated $LiNi_{0.8}Co_{0.15}Al_{0.05}O_2$ and a sulfide-based solid electrolyte. *J. Power Sources* **196**, 6488–6492 (2011).

26. Hayashi, A. *et al.* All-solid-state lithium secondary batteries using NiS–carbon fiber composite electrodes coated with Li_2S–P_2S_5 solid electrolytes by pulsed laser deposition. *ACS Appl. Mater. Interfaces* **4**, 4274–4279 (2012).

27. Visbal, H. *et al.* The effect of diamond-like carbon coating on $LiNi_{0.8}Co_{0.15}Al_{0.05}O_2$ particles for all solid-state lithium-ion batteries based on Li_2S–P_2S_5 glass-ceramics. *J. Power Sources* **314**, 85–92 (2016).

28. Ito, S. *et al.* A rocking chair type all-solid-state lithium ion battery adopting Li_2O–ZrO_2 coated $LiNi_{0.8}Co_{0.15}Al_{0.05}O_2$ and a sulfide-based electrolyte. *J. Power Sources* **248**, 943–950 (2014).

29. Seino, Y. *et al.* Synthesis of phosphorous sulfide solid electrolyte and all-solid-state lithium batteries with graphite electrode. *Solid State Ion.* **176**, 2389–2393 (2005).

30. Takeuchi, T. *et al.* Application of graphite–solid electrolyte composite anode in all-solid-state lithium secondary battery with Li_2S positive electrode. *Solid State Ion.* **262**, 138–142 (2014).

31. Takada, K. *et al.* Solid-state lithium battery with graphite anode. *Solid State Ion.* **158**, 269–274 (2003).

32. Xi, J. *et al.* Polymer-based solid electrolytes: material selection, design, and application. *Adv. Funct. Mater.* **31**, 2007599 (2021).

33. Aziz, S. B. & Abidin, Z. H. Z. Ion-transport study in nanocomposite solid polymer electrolytes based on chitosan: Electrical and dielectric analysis. *J. Appl. Polym. Sci.* **132**, (2015).

34. Borgohain, M. M., Joykumar, T. & Bhat, S. V. Studies on a nanocomposite solid polymer electrolyte with hydrotalcite as a filler. *Solid State Ion.* **181**, 964–970 (2010).

35. Fergus, J. W. Ceramic and polymeric solid electrolytes for lithium-ion batteries. *J. Power Sources* **195**, 4554–4569 (2010).

36. Hull, S. Fast ionic transport in solids. *Science* **204**, 1371–1376 (1979).

37. Li, S. *et al.* Progress and Perspective of Ceramic/Polymer Composite Solid Electrolytes for Lithium Batteries. *Adv. Sci.* **7**, 1903088 (2020).

38. Jeong, S.-K., Lee, Y.-J. & Jo, N.-J. Electrochemical Properties of PVDF-Based Nanocomposite Solid Polymer Electrolytes. *Macromol. Symp.* **249–250**, 167–173 (2007).

39. Ramesh, S. & Arof, A. K. Preparation and electrical characterization of (PVC + $KBrO_3$) polymer electrolytes for solid-state battery applications. *Ionics* **13**, 421–426 (2007).

40. Rajendran, S., Uma, T. & Mahalingam, T. Characterisation of plasticized PMMA based solid polymer electrolytes. *Ionics* **5**, 232–235 (1999).

41. Liao, M., Zhou, Y., Jiang, X. & Wan, R. In situ construction of 3D Li channels high-temperature-resistant polymer electrolyte and Li_3N-rich interface enabling stable solid-state Li metal battery. *Chem. Eng. J.* **480**, 148020 (2024).

42. Elbouazzaoui, K. *et al.* Enabling high-voltage polymer-based solid-state batteries through reinforcements with $LiAlO_2$ fillers. *Adv. Energy Mater.* **34**, 2405249 (2024).

43. Pitawala, H. M. J. C., Dissanayake, M. A. K. L. & Seneviratne, V. A. Combined effect of Al_2O_3 nano-fillers and EC plasticizer on ionic conductivity enhancement in the solid polymer electrolyte $(PEO)_9LiTf$. *Solid State Ion.* **178**, 885–888 (2007).

44. Liu, Y., Lee, J. Y. & Hong, L. Functionalized SiO_2 in poly(ethylene oxide)-based polymer electrolytes. *J. Power Sources* **109**, 507–514 (2002).

45. Kumar, R., Subramania, A., Sundaram, N. T. K., Kumar, G. V. & Baskaran, I. Effect of MgO nanoparticles on ionic conductivity and electrochemical properties of nanocomposite polymer electrolyte. *J. Membr. Sci.* **300**, 104–110 (2007).

46. Cheng, X.-B., Zhang, R., Zhao, C.-Z. & Zhang, Q. Toward safe lithium metal anode in rechargeable batteries: a review. *Chem. Rev.* **117**, 10403–10473 (2017).

47. Song, J. Y., Wang, Y. Y. & Wan, C. C. Review of gel-type polymer electrolytes for lithium-ion batteries. *J. Power Sources* **77**, 183–197 (1999).

48. Liu, S. *et al.* Filler-Integrated Composite Polymer Electrolyte for Solid-State Lithium Batteries. *Adv. Mater.* **35**, 2110423 (2023).

49. Zhao, E., Ma, F., Guo, Y. & Jin, Y. Stable LATP/LAGP double-layer solid electrolyte prepared via a simple dry-pressing method for solid state lithium ion batteries. *RSC Adv.* **6**, 92579–92585 (2016).

50. Weiss, M., Weber, D. A., Senyshyn, A., Janek, J. & Zeier, W. G. Correlating Transport and Structural Properties in $Li_{1+x}Al_xGe_{2-x}(PO_4)_3$ (LAGP) Prepared from Aqueous Solution. *ACS Appl. Mater. Interfaces* **10**, 10935–10944 (2018).

51. Zhang, Y. *et al.* Progress and Perspectives of Lithium Aluminum Germanium Phosphate-Based Solid Electrolytes for Lithium Batteries. *Adv. Funct. Mater.* **33**, 2300973 (2023).

52. Manthiram, A., Yu, X. & Wang, S. Lithium battery chemistries enabled by solid-state electrolytes. *Nat. Rev. Mater.* **2**, 16103 (2017).

53. Lu, J., Li, Y. & Ding, Y. Structure, stability, and ionic conductivity of perovskite $Li_{2x-y}Sr_{1-x-y}La_yTiO_3$ solid electrolytes. *Ceram. Int.* **46**, 7741–7747 (2020).

54. Le, H. T. T. *et al.* Citrate gel synthesis of aluminum-doped lithium lanthanum titanate solid electrolyte for application in organic-type lithium–oxygen batteries. *J. Power Sources* **274**, 1188–1199 (2015).

55. Sun, H., Kang, S. & Cui, L. Prospects of LLZO type solid electrolyte: From material design to battery application. *Chem. Eng. J.* **454**, 140375 (2023).

56. Buschmann, H. *et al.* Structure and dynamics of the fast lithium ion conductor "$Li_7La_3Zr_2O_{12}$". *Phys. Chem. Chem. Phys.* **13**, 19378–19392 (2011).

57. Lau, J. *et al.* Sulfide Solid Electrolytes for Lithium Battery Applications. *Adv. Energy Mater.* **8**, 1800933 (2018).

58. Liu, Z. *et al.* Anomalous High Ionic Conductivity of Nanoporous β-Li3PS4. *J. Am. Chem. Soc.* **135**, 975–978 (2013).

59. Phuc, N. H. H., Totani, M., Morikawa, K., Muto, H. & Matsuda, A. Preparation of Li_3PS_4 solid electrolyte using ethyl acetate as synthetic medium. *Solid State Ion.* **288**, 240–243 (2016).

60. Chen, S. *et al.* In-situ preparation of poly(ethylene oxide)/Li_3PS_4 hybrid polymer electrolyte with good nanofiller distribution for rechargeable solid-state lithium batteries. *J. Power Sources* **387**, 72–80 (2018).

61. Huggins, R. A. & Angell, C. A. Temperature–conductance curves of solid salts. III. Halides of lithium. *J. Am. Chem. Soc.* **98**, 6170–6175 (1976).

62. Li, X. *et al.* Progress and perspectives on halide lithium conductors for all-solid-state lithium batteries. *Energy Environ. Sci.* **13**, 1429–1461 (2020).

63. Li, X. *et al.* Progress and perspectives on halide lithium conductors for all-solid-state lithium batteries. *Energy Environ. Sci.* **13**, 1429–1461 (2020).

64. Asano, T. *et al.* Solid Halide Electrolytes with High Lithium-Ion Conductivity for Application in 4 V Class Bulk-Type All-Solid-State Batteries. *Adv. Mater.* **30**, 1803075 (2018).

65. Yang, S., Kim, S. Y. & Chen, G. Halide Superionic Conductors for All-Solid-State Batteries: Effects of Synthesis and Composition on Lithium-Ion Conductivity. *ACS Energy Lett.* **9**, 2212–2221 (2024).

66. Wang, K. *et al.* A cost-effective and humidity-tolerant chloride solid electrolyte for lithium batteries. *Nat. Commun.* **12**, 4410 (2021).

67. Manthiram, A., Yu, X. & Wang, S. Lithium battery chemistries enabled by solid-state electrolytes. *Nat. Rev. Mater.* **2**, 16103 (2017).

68. Gulino, V. *et al.* Phase Stability and Fast Ion Conductivity in the Hexagonal $LiBH_4$–LiBr–LiCl Solid Solution. *Chem. Mater.* **31**, 5133–5144 (2019).

69. Wang, S. *et al.* Lithium Chlorides and Bromides as Promising Solid-State Chemistries for Fast Ion Conductors with Good

Electrochemical Stability. *Angew. Chem. Int. Ed.* **58**, 8039–8043 (2019).

70. Manthiram, A., Yu, X. & Wang, S. Lithium battery chemistries enabled by solid-state electrolytes. *Nat. Rev. Mater.* **2**, 1–16 (2017).

71. Pang, Y., Liu, Y., Yang, J., Zheng, S. & Wang, C. Hydrides for solid-state batteries: A review. *Mater. Today Nano* **18**, 100194 (2022).

72. Boukamp, B. A. & Huggins, R. A. Ionic conductivity in lithium imide. *Phys. Lett. A* **72**, 464–466 (1979).

73. Matsuo, M., Nakamori, Y., Orimo, S., Maekawa, H. & Takamura, H. Lithium superionic conduction in lithium borohydride accompanied by structural transition. *Appl. Phys. Lett.* **91**, 224103 (2007).

74. Ikeshoji, T. *et al.* Fast-ionic conductivity of Li^+ in $LiBH_4$. *Phys Rev B* **83**, 144301 (2011).

75. Matsuo, M. & Orimo, S. Lithium Fast-Ionic Conduction in Complex Hydrides: Review and Prospects. *Adv. Energy Mater.* **1**, 161–172 (2011).

76. Maekawa, H. *et al.* Halide-Stabilized $LiBH_4$, a Room-Temperature Lithium Fast-Ion Conductor. *J. Am. Chem. Soc.* **131**, 894–895 (2009).

77. Matsuo, M. *et al.* Effect of heat treatment on the lithium ion conduction of the $LiBH_4$–LiI solid solution. *J. Phys. Chem. C* **117**, 19996–20001 (2013).

78. Filinchuk, Y., Chernyshov, D. & Dmitriev, V. Diffuse and doubly split atom occupation in hexagonal $LiBH_4$. *Appl. Phys. Lett.* **95**, 221901 (2009).

79. Yan, Y. *et al.* A lithium amide–borohydride solid-state electrolyte with lithium-ion conductivities comparable to liquid electrolytes. *Adv. Energy Mater.* **7**, 1700294 (2017).

80. Matsuo, M. *et al.* Complex Hydrides with $(BH_4)^-$ and $(NH_2)^-$ Anions as New Lithium Fast-Ion Conductors. *J. Am. Chem. Soc.* **131**, 16389–16391 (2009).

81. Matsuo, M. *et al.* Complex Hydrides with $(BH_4)^-$ and $(NH_2)^-$ Anions as New Lithium Fast-Ion Conductors. *J. Am. Chem. Soc.* **131**, 16389–16391 (2009).

82. Sørby, M. H. *et al.* $LiCe(BH_4)_3Cl$, a new lithium-ion conductor and hydrogen storage material with isolated tetranuclear anionic clusters. *Chem. Mater.* **24**, 3635–3643 (2012).

83. Sørby, M. H. *et al.* New Li ion conductors and solid-state hydrogen storage materials: $LiM(BH_4)_3Cl$ (M = La, Gd). *J. Phys. Chem. C* **116**, 16140–16146 (2012).

84. Nguyen, J., Fleutot, B. & Janot, R. Investigation of the stability of metal borohydrides-based compounds LiM(BH4)3Cl (M = La, Ce, Gd) as solid electrolytes for Li-S batteries. *Solid State Ion.* **315**, 26–32 (2018).

85. Kim, S. *et al.* Lithium ion disorder and conduction mechanism in $LiCe(BH_4)_3Cl$. *J. Phys. Chem. C* **120**, 24650–24657 (2016).

86. Sørby, M. H. *et al.* Solid-state synthesis, structural characterization and ionic conductivity of bimetallic alkali-metal

yttrium borohydrides $MY(BH_4)_4$ (M = Li and Na). *J. Mater. Chem. A* **4**, 15272–15279 (2016).

87. Zhang, T. *et al.* Ammonia, a Switch for Controlling High Ionic Conductivity in Lithium Borohydride Ammoniates. *Joule* **2**, 1522–1533 (2018).

88. Grinderslev, J. B. *et al.* Methylamine lithium borohydride as electrolyte for all-solid-state batteries. *Angew. Chem. Int. Ed.* **61**, e202203484 (2022).

89. Blanchard, D. *et al.* Nanoconfined $LiBH_4$ as a fast lithium ion conductor. *Adv. Funct. Mater.* **25**, 184–192 (2015).

90. Choi, Y. S., Lee, Y.-S., Oh, K. H. & Cho, Y. W. Interface-enhanced Li ion conduction in a LiBH4–SiO2 solid electrolyte. *Phys. Chem. Chem. Phys.* **18**, 22540–22547 (2016).

91. Qiu, P. *et al.* A high-rate and long-life sodium metal battery based on a $NaB_3H_8{\cdot}xNH_3$@NaB_3H_8 composite solid-state electrolyte. *Angew. Chem. Int. Ed.* **63**, e202401480 (2024).

92. Zeng, S. *et al.* Stabilization of fast lithium-ionic conduction phase of nanaoconfined $LiBH_4$ for lithium metal solid-state batteries. *Chem. Commun.* **61**, 929–932 (2025).

93. Blanchard, D. *et al.* Nanoconfined $LiBH_4$ as a Fast Lithium Ion Conductor. *Adv. Funct. Mater.* **25**, 184–192 (2015).

94. Liu, Z. *et al.* Lithium migration pathways at the composite interface of $LiBH_4$ and two-dimensional MoS_2 enabling superior ionic conductivity at room temperature. *Phys. Chem. Chem. Phys.* **22**, 4096–4105 (2020).

95. Wu, Z. *et al.* Defective Boron Nitride Inducing the Lithium-ion Migration on the Sub-Surface of $LiBH_4$. *Adv. Funct. Mater.* **32**, 2205677 (2022).

96. Hu, L. *et al.* Interface Modification and Halide Substitution To Achieve High Ionic Conductivity in $LiBH_4$-Based Electrolytes for all-Solid-State Batteries. *ACS Appl. Mater. Interfaces* **14**, 1260–1269 (2022).

97. Li, H.-W., Akiba, E. & Orimo, S. Comparative study on the reversibility of pure metal borohydrides. *J. Alloys Compd.* **580**, S292–S295 (2013).

98. Udovic, T. J. *et al.* Exceptional superionic conductivity in disordered sodium decahydro-closo-decaborate. *Adv. Mater.* **26**, 7622–7626 (2014).

99. Asakura, R. *et al.* Fast lithium-ion conduction in atom-deficient closo-type complex hydride solid electrolytes. *Chem. Mater.* **30**, 3792–3798 (2018).

100. Zhang, Y. *et al.* Bi-functional $Li_2B_{12}H_{12}$ for energy storage and conversion applications: solid-state electrolyte and luminescent down-conversion dye. *J. Mater. Chem. A* **3**, 17361–17368 (2015).

101. Orimo, S. *et al.* The renaissance of hydrides as energy materials. *Nat. Rev. Mater.* **1**, 16091 (2016).

102. He, L. *et al.* Synthesis of a Bimetallic Dodecaborate $LiNaB_{12}H_{12}$ with Outstanding Superionic Conductivity. *Chem. Mater.* **27**, 5483–5486 (2015).

103. Yoshida, K. *et al.* Fast sodium ionic conduction in $Na_2B_{10}H_{10}$-$Na_2B_{12}H_{12}$ pseudo-binary complex hydride and application to a bulk-type all-solid-state battery. *Appl. Phys. Lett.* **110**, 103901 (2017).

104. Cuan, J. *et al.* Borohydride-Scaffolded Li/Na/Mg Fast Ionic Conductors for Promising Solid-State Electrolytes. *Adv. Mater.* **31**, 1803533 (2019).

105. He, L. *et al.* $Na_3NH_2B_{12}H_{12}$ as high performance solid electrolyte for all-solid-state Na-ion batteries. *J. Power Sources* **396**, 574–579 (2018).

106. Asakura, R. *et al.* Electrochemical Oxidative Stability of Hydroborate-Based Solid-State Electrolytes. *ACS Appl. Energy Mater.* **2**, 6924–6930 (2019).

107. Braun, H., Łodziana, Z., Battaglia, C. & Remhof, A. Electrochemical reductive stability of lithium hydridoborate solid-state electrolytes. *J. Mater. Sci. Mater. Energy* **2**, 2 (2026).

108. Tang, W. S. *et al.* Unparalleled lithium and sodium superionic conduction in solid electrolytes with large monovalent cage-like anions. *Energy Environ. Sci.* **8**, 3637–3645 (2015).

109. Sadikin, Y., Brighi, M., Schouwink, P. & Černý, R. Superionic Conduction of Sodium and Lithium in Anion-Mixed Hydroborates $Na_3BH_4B_{12}H_{12}$ and $(Li_{0.7}Na_{0.3})_3BH_4B_{12}H_{12}$. *Adv. Energy Mater.* **5**, (2015).

110. Tang, W. S. *et al.* Liquid-like ionic conduction in solid lithium and sodium monocarba-closo-decaborates near or at room temperature. *Adv. Energy Mater.* **6**, 1502237 (2016).

111. Zheng, F. *et al.* Enhanced Li ion conductivity in $LiBH_4$–Al_2O_3 mixture via interface engineering. *J. Phys. Chem. C* **121**, 24669–24676 (2017).

112. Choi, Y. S., Lee, Y.-S., Oh, K. H. & Cho, Y. W. Interface-enhanced Li ion conduction in a $LiBH_4$ –SiO_2 solid electrolyte. *Phys. Chem. Chem. Phys.* **18**, 22540–22547 (2016).

113. Maier, J. Conductor–insulator interfaces in solid electrolytes. *Prog. Solid State Chem.* **23**, 171–263 (1995).

114. Kato, A. *et al.* High ionic conductivity of liquid-phase-synthesized Li_3PS_4 solid electrolyte, comparable to that obtained via ball milling. *ACS Appl. Energy Mater.* **4**, 251–258 (2021).

115. Li, M., Chi, X. & Yu, J. Zeolite-Based Electrolytes: A Promising Choice for Solid-State Batteries. *PRX Energy* **1**, 031001 (2022).

116. Zhao, W. *et al.* Li-Ion Conductivity Enhancement of $LiBH_4 \cdot xNH_3$ with *In Situ* Formed Li_2O Nanoparticles. *ACS Appl. Mater. Interfaces* **13**, 31635–31641 (2021).

117. Angizi, S. *et al.* Boron nitride-integrated lithium batteries: exploring innovations in longevity and performance. *Energy Environ. Mater.* **7**, e12777 (2024).

118. Wu, J. *et al.* Electrolyte with boron nitride nanosheets as leveling agent towards dendrite-free lithium metal anodes. *Nano Energy* **72**, 104725 (2020).

119. Shi, L., Xu, A. & Zhao, T. First-Principles Investigations of the Working Mechanism of 2D h-BN as an Interfacial Layer for the Anode of Lithium Metal Batteries. *ACS Appl. Mater. Interfaces* **9**, 1987–1994 (2017).

Chapter 2 Characterization and measurement

Abstract

The physical and chemical properties of the different materials, including structure, components, dynamics *et al*. have been characterized via various analytical techniques, such as X-ray diffraction (XRD), synchrotron X-ray diffraction, infrared spectroscopy (FTIR), etc. Electrochemical impedance spectroscopy (EIS), linear sweep voltammetry, and galvanostatic cycling performance with different current densities were conducted with assembled symmetrical cells to investigate the electrochemical properties of as-prepared electrolytes.

2.1 Mechanical Ball-milling

Mechanical ball-milling is a typical synthesis method to prepare solid materials, largely avoiding the use of solvents. During the process, the powder samples are placed in a sealed jar together with small metal shaker balls. When the jar rotates, the balls hit the powders against the jar walls, creating strong impacts and friction, which help the solid materials to mix and react with each other. Compared with other synthesis methods, mechanical ball-milling is also easier to scale up for large-scale production, making it suitable for practical applications in energy materials.

In this thesis, we employed a planetary ball mill (XQM-0.4A, Changsha) for all sample preparation (**Fig.2.1**). Since our materials are

highly sensitive to air and moisture, all milling procedures were carried out inside an argon-filled glovebox. For each ball-milling process, the milling speed, duration time, and ball-to-powder ratio were carefully adjusted to achieve good mixing and reaction. To prevent excessive milling and overheating, short break times were added between the milling cycles.

Fig. 2.1 The photograph of planetary ball mill (XQM-0.4A, Changsha).

2.2 Powder X-ray Diffraction

X-ray diffraction is commonly used to analyze the structure and composition of materials. In X-ray diffraction, a regular array of spherical waves adds constructively in a few specific directions, determined by Laue equations.

In this thesis, powder X-ray diffraction (PXRD) measurements were carried out with an Incoatec X-ray generator (mixed Mo Kα radiation, weighted average λ = 0.71073 Å) operated at 50 kV and 1000 μA and a MAR345 image plate detector. Air sensitive samples are filled into glass capillaries in an argon glovebox. Measured samples were not reused for other characterization techniques. The data were integrated by the Fit2D software (ESRF) using a calibration with a standard LaB_6 sample.

2.3 Synchrotron X-ray Diffraction

Synchrotron X-ray diffraction was used to study the structural evolution of the samples as a function of temperature (T). Compared to X-ray diffraction, synchrotron radiation has several advantages for high-resolution diffraction measurements, such as a much more intense, highly collimated beam, tunable wavelengths, and excellent monochromatization. It is the electromagnetic radiation emitted typically by electrons moving close to the speed of light when they change the direction of their movement.

In this thesis, the diffraction data were collected at the European Synchrotron Radiation Facility (ESRF, Grenoble, France), at Swiss-Norwegian Beam Lines, BM01, and at the high-resolution powder diffraction beamline, ID22.

Compared to conventional *ex-situ* measurements, *in-situ* diffraction provides a third parameter-temperature (T), in addition to the diffraction intensity and 2θ position. This allows us to directly follow the evolution of diffraction patterns as the temperature changes. The collected diffraction data were subsequently analyzed to identify the phase composition and structural changes. Moreover, the high-quality synchrotron data were further refined and modeled using the FOX and FullProf software packages to determine the crystal structure and refine atomic positions by Rietveld method. These analyses provided reliable structural insights supporting the discussion of phase formation and ionic transport mechanisms.

2.4 Nuclear Magnetic Resonance

Nuclear Magnetic Resonance (NMR) spectroscopy is an analytical technique that investigates the structure, dynamics, and interactions of molecules by the magnetic properties of certain atomic nuclei. In this work, liquid-state ^{11}B NMR spectroscopy was employed to probe the chemical environment of boron species. Placing the sample in a strong magnetic field causes its atomic nuclei to align with the field. The sample is then subjected to a radiofrequency pulse, causing the nuclei to absorb energy and transition to a higher energy state. When the nuclei return to their original state, they release energy in the form of electromagnetic radiation, which is detected and quantified by the NMR instrument.

2.5 Fourier Transform Infrared Spectroscopy

Fourier Transform Infrared Spectroscopy (FTIR) is an analytical technique that combines computer technology with infrared spectroscopy to determine the infrared absorption spectra of samples for identification purposes. Due to the ability of molecules in the sample to absorb infrared light through energy level transitions, FTIR analysis can provide information about the functional groups and chemical structures of unknown substances in powdered samples. FTIR analysis is characterized by high sensitivity, high measurement accuracy, and high resolution, making it widely used in scientific research.

Infrared spectra were collected between 400 and 4000 cm^{-1} by FTIR with an attenuated total reflectance accessory (ATR/FTIR) in an Argon glovebox.

2.6 Differential Scanning Calorimetry

Differential Scanning Calorimetry (DSC) analysis was conducted to evaluate the thermal stability of the samples. Approximately 10 mg samples were placed into sealed alumina holders with lids. The samples were subjected to heating under an Ar atmosphere with the desired temperature range at a rate of 5 ℃ per minute.

2.7 Thermogravimetric Analysis

Thermogravimetric Analysis (TGA) is used for the investigation of the changes in the physical and chemical properties of materials

induced by heat. Measurements are usually performed either as a function of temperature at constant heating rate, or as a function of time at a constant temperature by considering the mass loss. In this work, experiments were conducted using a *NETZSCH STA 409 PC* analyzer. Typically, 5-10 mg of samples was loaded in an alumina pan and heated from room temperature to 300 ℃, at a rate of 5 ℃ per min.

2.8 Nitrogen Physisorption

Nitrogen physisorption measurements are performed on the Micromeritics TriStar Surface Area and Porosity Analyzer. As samples were dried before storage, as described in Section 2.2.1, no further activation was performed before measurements. Sample preparation was performed in an argon glovebox and transferred to the Analyzer shortly before the measurement in an airtight glass physisorption tube. In a typical measurement, between 50 mg and 100 mg of samples were measured. Measurement temperatures were carried out at 77 K, cooled by liquid nitrogen. In nitrogen physisorption, the sample-containing tube is degassed under vacuum before the experiment. Step by step, a small amount of nitrogen is introduced into the tube and absorbed onto the sample. By comparing the amount of introduced nitrogen and the relative nitrogen pressure (p/p_0, where p and p_0 are the equilibrium and saturation pressure of nitrogen at 77 K) the volume of adsorbed nitrogen can be calculated. Similar steps can be performed in the desorption process, yielding a desorption isotherm curve. Although these

measurements are performed below atmospheric pressures and at a low temperature, the measured volumes will be converted to standard temperature and pressure (STP, T=273.15K and *p*=1 bar). This STP is used in the practical environment of the synthesis.

2.9 Scanning Electron Microscopy

Scanning electron microscopy (SEM) is one of the most widely used electron microscopy techniques, capable of providing high-quality images with excellent spatial resolution. When a sample is exposed to a high-energy electron beam, information about its morphology, structure, composition, grain orientation, and crystallography can be obtained.

In this thesis, the surface of samples was coated with a thin layer of gold or carbon and fixed onto the sample holder using conductive adhesive tape. They were then quickly transferred into the SEM chamber to minimize exposure to air before measurement. The SEM measurements in this work were carried out at an accelerating voltage of 10 kV and an emission current of 10 μA.

2.10 X-ray Photoelectron Spectroscopy

X-ray photoelectron spectroscopy (XPS) is a surface-sensitive analytical technique used to determine the elemental composition, chemical states, and electronic states of the elements within a material. In this work, XPS analyses were carried out on an ESCALAB 250 Xi

spectrometer with Al Kα X-ray source (λ=0.83401nm) under a base pressure of 5×10 10 Torr. The sample was initially cold-pressed into a pellet inside an argon-filled glove box and then mounted on a sample holder, which was transferred using a special container from the glove box to the XPS facility to prevent air exposure. The Ar^+ ion sputtering was conducted at 2000 eV (400 μm spot size) using a sputtering area of 2.5mm×2.5mm to obtain the XPS depth profiles.

2.11 Electrochemical Impedance Spectroscopy

Electrochemical impedance spectroscopy (EIS) is an efficient and non-destructive technique used to characterize the ionic conductivity of solid electrolytes in solid-state batteries. The ionic conductivity of SSEs is measured by electrochemical impedance spectroscopy (EIS). Nyquist plots are recorded in the frequency range between 7 MHz and 100 mHz with an AC voltage of 100 mV. In this work, the EIS measurement results were obtained by using Biologic SP-300. The SSEs are pressed into pellets with a diameter of 9 mm and a thickness of 0.6-1.0 mm, approximately under the cold pressure of 600 MPa. The measurement pellets are prepared in a symmetric cell which consists of two blocked electrodes (stainless steel, SS) and one SSE, to assemble SS|SSE|SS using a Swagelok mold (**Fig. 2.2**). EIS measurements were carried out from 30 ℃ to 80 ℃ with 0.33 ℃ min^{-1} at an interval of 10 ℃. Each temperature point was required for a holding of 30 minutes to ensure

data reproducibility of the measurement. The ionic conductivities of SSEs are determined using Eqn (1)

$$\sigma = \frac{L}{RS} \qquad (1)$$

where $\boldsymbol{L}$ (in cm) is the thickness of the SSEs, $\boldsymbol{R}$ (in Ω) is the value of bulk resistance extracted from the complex EIS plots, and $\boldsymbol{S}$ (in cm ^{2}) is the area of the SEEs.

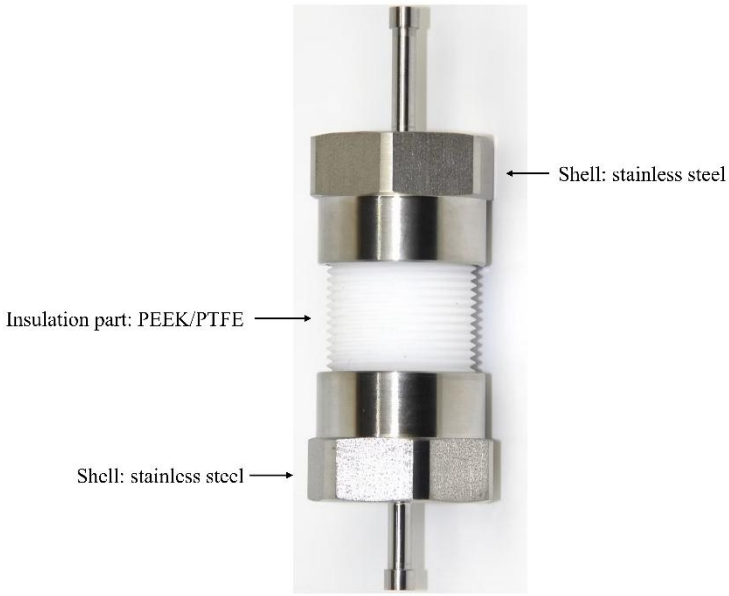

Fig. 2.2 The photograph of the Swagelok cell for EIS.

The activation energy E_a can be calculated according to the Nernst-Einstein equation and the Arrhenius equation (2).

$$\ln \sigma T = \frac{E_a}{K_B T} + C \qquad (2)$$

Where $\boldsymbol{\sigma}$ is conductivity, C is the pre-exponential factor, K_B is Boltzmann's constant, and T is the temperature (K).

2.12 Direct Current (DC) Polarization

The electronic conductivity of the complex electrolyte was obtained by Direct Current (DC) polarization. For the DC test, solid-state electrolyte pellets were covered by two stainless steel electrodes on both sides at a DC voltage of 500 mV. Electronic conductivity can be calculated by Eqs (1) and (3).

$$R = \frac{U}{I} \qquad (3)$$

2.13 Linear Sweep Voltammetry (LSV)

The electrochemical stability of the SSE is investigated by linear sweep voltammetry (LSV). LSV is conducted for the [SS|SSEs|SS] CR2032 coin cell. For all LSV measurements, the cells took a 3-hour rest period at the desired temperature and then were subjected to measurements by Biologic SP-300. LSV measurements were conducted within a voltage range from open circuit potential to 4.0 V versus Li^+/Li (Na^+/Na) at a scanning rate of 0.1 mV s^{-1}.

2.14 Galvanostatic Cycling Test

Galvanostatic cycling is a common electrochemical technique used to study the performance of batteries by monitoring the voltage response of a system under a constant current.

In a lithium (or sodium) symmetric cell, both the anode and cathode are lithium (or sodium) metal foils, and the solid-state electrolyte is sandwiched between them. This setup is widely used to evaluate the stability of solid electrolytes, interfacial resistance, and lithium/sodium plating-stripping behavior without interference from cathode materials.

In this work, lithium (or sodium) symmetric cells were assembled inside an argon-filled glovebox to prevent exposure to air and moisture. After assembly, the cells were kept at room temperature for 5 h to ensure sufficient contact between the electrolyte and the electrodes. The cycling tests were then carried out under constant current conditions to assess the interfacial compatibility and overall cycling stability of the solid-state electrolytes.

Assembling Li or Na-metal cells with a cathode is essential for studying the practical electrochemical performance of solid-state electrolytes under real operating conditions. Typically, the cathode active material, solid electrolyte, and conductive carbon were mixed in a certain ratio to prepare a composite cathode. The composite cathode, solid-state electrolyte, and lithium metal were then symmetrically assembled to fabricate the all-solid-state battery (**Fig. 2.3**). $Li_4Ti_5O_{12}$ (LTO) is commonly selected as the cathode material in borohydride-based studies because of its moderate operating voltage around 1.55 V *vs*. Li^+/Li. It exhibits negligible volume change during lithium insertion and extraction, which helps maintain a stable electrode-electrolyte

interface throughout cycling.

Fig. 2.3 Diagram of fabricating the all-solid-state battery.

Chapter 3 Zeolite-Integrated $LiBH_4$ Solid Electrolytes with Enhanced Ionic Conductivity for Li batteries

Abstract

Solid-state batteries are widely regarded as a cornerstone of next-generation energy storage technologies, offering intrinsic safety and the potential for superior energy density through the safe utilization of lithium metal anodes compared to conventional liquid-electrolyte systems. Among the diverse solid-state electrolyte candidates, lithium borohydride ($LiBH_4$) has attracted considerable attention owing to its excellent thermodynamic stability against Li metal. However, its practical application is severely constrained by its extremely low room-temperature ionic conductivity (~10^{-8} S cm^{-1}) and poor phase stability. Here, we design a $LiBH_4$-zeolite composite via a facile ball-milling route to exploit strong interfacial interactions between $LiBH_4$ and the mesoporous framework. Compared with conventional oxide additives (Al_2O_3, SiO_2, ZrO_2), zeolite provides abundant surface sites and interconnected nanochannels that stabilize the interfacial Li^+ environment and facilitate fast ion transport. The optimized composite electrolyte delivers a room-temperature ionic conductivity of 1.49×10^{-5} S cm^{-1}, three orders of magnitude higher than pristine $LiBH_4$ and increases further to 1.53×10^{-4} S cm^{-1} at 80°C. Additionally, it exhibits a wide electrochemical stability window (0.22-2.86 V *vs.* Li/Li^+), negligible electronic conductivity （~10^{-10} S cm^{-1}）, and exceptional interfacial compatibility with lithium metal, enabling stable cycling over 200 hours at 0.1 mA cm^{-2}. When coupled with a $Li_4Ti_5O_{12}$ cathode, the composite solid electrolyte enables the all-solid-state cell to deliver

near-theoretical specific capacities at 100 °C with low polarization. These findings demonstrate that zeolite scaffolds can regulate $LiBH_4$ ion transport and interfacial stability, providing a scalable and cost-effective route toward high-performance solid-state batteries.

3.1 Introduction

The development of solid-state electrolytes represents a paradigm shift in lithium-ion battery technology, as they address the intrinsic limitations of conventional liquid electrolytes, including flammability, poor thermal stability, and incompatibility with high-energy-density lithium metal anodes[1]. By eliminating volatile organic solvents, solid-state electrolytes not only enhance safety but also enable the integration of advanced electrode materials, thereby paving the way for batteries with higher energy densities and longer lifespans[2–5]. Among the various candidates, lithium borohydride ($LiBH_4$) has emerged as a particularly attractive material[6,7]. In its high-temperature hexagonal phase, $LiBH_4$ exhibits high ionic conductivity exceeding 10^{-3} S cm^{-1} (above 393K), along with a wide electrochemical stability window and low density.[8] These intrinsic properties highlight its potential as an alternative to both liquid electrolytes and conventional oxide- or sulfide-based solid electrolytes. However, its practical application remains severely limited by the extremely low ionic conductivity at room temperature (~10^{-8} S cm^{-1}) and poor compatibility with high-voltage cathodes, arising from the highly reductive nature of the BH_4^- anion.

To overcome these challenges, extensive strategies have been proposed to optimize the ionic conductivity and stability of $LiBH_4$-based electrolytes. Anion substitution ([I^-], [Cl^-], [Br^-])[9–12], has been shown to stabilize the high-temperature hexagonal phase at lower temperatures. Incorporation of neutral molecules such as NH_3 or

CH_3NH_3[13–16] can also enhance the ionic conductivity of $LiBH_4$, however, their operating temperature must be carefully controlled due to instability above 60 °C. Another widely explored approach is the introduction of nanoscale scaffolds or insulating oxides to confine $LiBH_4$ within nanoscale domains, thereby reducing diffusion barriers and stabilizing its conductive phase. For instance, incorporating $LiBH_4$ into mesoporous SiO_2[17–20] or Al_2O_3[21,22] through melting has been shown to improve lithium-ion mobility, albeit through high-cost and complex processes. The $LiBH_4$-SiO_2 composite, in particular, achieves high ionic conductivity due to the formation of a conductive interfacial layer[23]. Collectively, these studies underscore the critical role of interfacial interactions on the electrochemical behavior of $LiBH_4$.

Zeolites, with their uniform pore sizes, high surface areas, and interconnected channels, have been extensively employed in catalysis[24] and gas adsorption[25]. They are also inherently attractive for energy storage applications because of their abundance, low processing cost, and scalability. Moreover, zeolites exhibit excellent thermal and chemical stability, making them suitable as additives or separators in electrolyte systems[26–28]. Their intrinsically low electronic conductivity further contributes to safety by suppressing lithium dendrite formation[29]. Despite these advantages, the application of zeolites in solid-state batteries remains underexplored, with the only prior report involving LiX zeolite membranes in Li-air batteries[30]. This knowledge gap highlights the untapped potential of zeolite-based composites for

addressing the challenges of ionic transport and interfacial stability in solid-state electrolytes.

In this chapter, we investigate the effect of integrating mesoporous Y-type zeolites with $LiBH_4$ via a simple ball-milling process. The optimized composite, 720-$LiBH_4$ (1:2), achieves an impressive lithium-ion conductivity of ~10^{-4} S cm^{-1} at 80 °C and demonstrates stable cycling in symmetric Li||Li cells. The enhanced performance is attributed to the homogeneous dispersion of $LiBH_4$ within the zeolite framework, which facilitates the formation of a conductive interfacial layer. Furthermore, the $Li_4Ti_5O_{12}$|720-$LiBH_4$ (1:2) |Li all-solid-state battery exhibits excellent cycling performance at both 80 °C and 100 °C. This chapter establishes interfacial engineering as a baseline design strategy, providing a reference framework for the subsequent exploration of more advanced and intrinsically driven modification approaches in later chapters.

3.2 Results and discussions

Structural characterization

Table 3.1 List of samples.

Sample	Zeolite type	Zeolite: $LiBH_4$ Mass Ratio
760-$LiBH_4$(1:3)	760	1:3
760-$LiBH_4$(1:2)	760	1:2
760-$LiBH_4$(1:1)	760	1:1
760-$LiBH_4$(2:1)	760	2:1
720-$LiBH_4$(1:3)	720	1:3
720-$LiBH_4$(1:2)	720	1:2
720-$LiBH_4$(1:1)	720	1:1
720-$LiBH_4$(2:1)	720	2:1

The $LiBH_4$-zeolite composite electrolytes were synthesized through a one-step ball-milling process (**Table 3.1**). The structural features of 720-$LiBH_4$ and 760-$LiBH_4$ composites with different weight ratios after 4 hours of ball-milling were systematically investigated. **Table S3.1** summarizes the physical differences between the two kinds of zeolites (720 and 760). Notably, the key difference between zeolite 720 and 760 is that Zeolite 720 has a lower Si/Al ratio and a higher specific surface area. **Figs. S3.1 and S3.2** present SEM images and corresponding EDS mappings of pristine zeolites 720 and 760, showing flake-like morphologies with diameters of ~500 nm. The selection of zeolite as

the host matrix, instead of conventional mesoporous SiO_2, is due to its superior structural robustness under mechanochemical conditions. The amorphous and thin-walled framework of mesoporous SiO_2 may undergo significant pore collapse when subjected to the intense shear and impact forces during ball-milling.

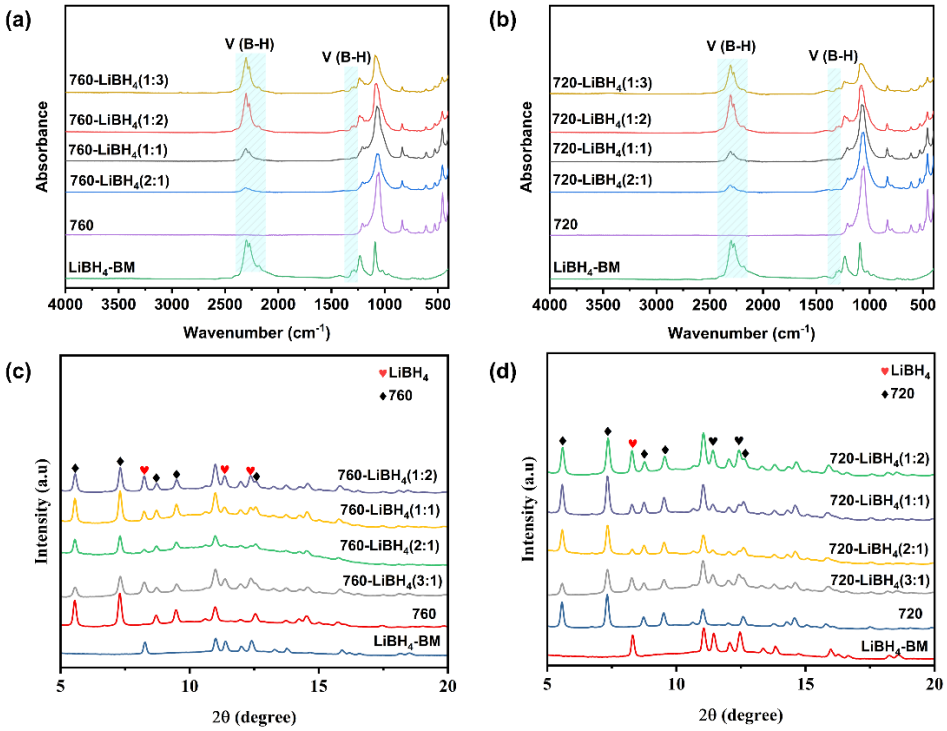

Fig. 3.1. (a-b) FTIR spectroscopy and **(c-d)** XRD pattern of zeolite-$LiBH_4$ composites and $LiBH_4$.

The FTIR absorbance spectra of the zeolite-$LiBH_4$ composites with different mass ratios, together with those of pure $LiBH_4$ and the zeolites 720 and 760, are shown in **Figs. 3.1(a) and 3.1(b)**. $LiBH_4$-BM exhibits characteristic [BH_4^-] stretching vibrations between 2000 and 2500 cm^{-1}, with bending modes at ≈1121 and 1089 cm^{-1}. For zeolite 720 and 760,

broad Si-O-H bands are observed in the 500-1300 cm^{-1} region[31]. In the zeolite-$LiBH_4$ (2:1) composite, the B-H stretching bands broaden significantly compared to $LiBH_4$-BM, suggesting that [BH_4^-] units reside in a more heterogeneous local environment, likely due to partial confinement within zeolite pores. As the $LiBH_4$ content increases, zeolite-related bandsolids (500-1300 cm^{-1}) weaken progressively, indicating the physical coverage of zeolite by $LiBH_4$ and enhanced interfacial interactions within the zeolite-$LiBH_4$ composites.

XRD results further corroborate these findings (**Fig. 3.1(c) and 1(d)**). All ball-milled mixtures retain the features of the raw materials, with distinct $LiBH_4$ peaks and broad reflections from the zeolites 720 and 760. No new phases were detected, implying no chemical reaction between $LiBH_4$ and the zeolite during milling. However, the diffraction peaks of $LiBH_4$ are significantly attenuated in the zeolite-$LiBH_4$ (2:1) composite compared to $LiBH_4$-BM[32]. This attenuation, together with the broad reflections from the zeolite, indicates that $LiBH_4$ is highly dispersed and may exist in a disordered or nanocrystalline state within the zeolite host. These observations confirm that ball milling generates intimate contact between $LiBH_4$ and the zeolite framework.

Conductivity of zeolite-$LiBH_4$ Composites

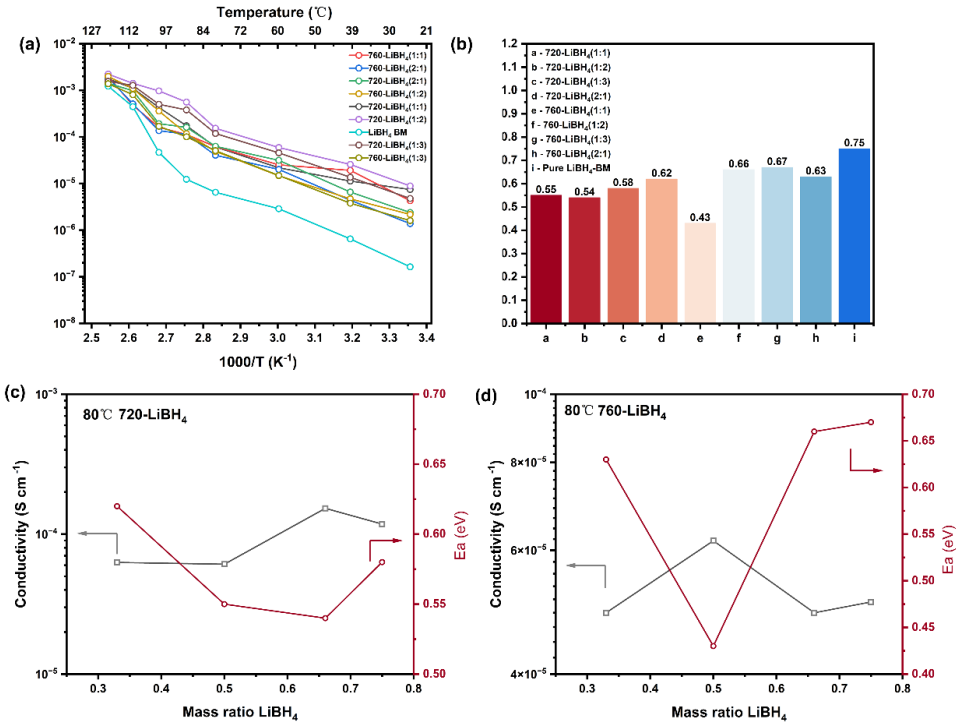

Fig. 3.2. (a) Temperature-dependent conductivities of zeolite-$LiBH_4$ materials with different mass ratios as well as $LiBH_4$-BM; **(b)** calculated activation energy of zeolite-$LiBH_4$ materials and $LiBH_4$-BM;**(c)** -**(d)** ionic conductivities and composition-dependent activation energy of zeolite (720,760)-$LiBH_4$ with different mass ratio (X).

The ionic conductivity was evaluated using cold-pressed pellets (9 mm diameter, 0.5-1.0 mm thickness) by electrochemical impedance spectroscopy (EIS) over a range of temperatures. Nyquist plots collected over 25-120 °C (**Fig. S3.3**) show typical semicircles at high frequency and linear tails at low frequency. $LiBH_4$-BM exhibits a large semicircle corresponding to ~15,091 Ω at 80 °C, reflecting its high resistance, the calculated ionic conductivity only reaches ~10^{-6} S cm^{-1}. In contrast, 720-$LiBH_4$ composites with mass ratios of 1:1, 1:2, 1:3, and

2:1 show much lower resistances of ~1069, 840, 946, and 3041 Ω, respectively, among which the 1:2 composition exhibits the lowest impedance. Similarly, 760-$LiBH_4$ composites with mass ratios of 1:1, 1:2, 1:3, and 2:1 exhibit resistances of ~2286, 2243, 1524, and 4323 Ω, respectively. The reduced semicircle diameters clearly indicate that zeolite incorporation significantly lowers the resistance of $LiBH_4$.

A detailed comparison of the ionic conductivities at different zeolite-to-$LiBH_4$ mass ratios revealed that the optimal composition varied between the two zeolites. The results are summarized in **Fig. 3.2(a)** and **Table S3.2**. At 40 ℃, the incorporation of zeolite significantly enhanced the ionic conductivity of $LiBH_4$, even at low loading. For instance, 720-$LiBH_4$ and 760-$LiBH_4$ with a mass ratio of 1:3 exhibited conductivities of 1.36×10^{-5} S cm^{-1} and 3.79×10^{-6} S cm^{-1}, respectively.

Increasing the zeolite content further improved conductivity, with 720-$LiBH_4$ (1:2) achieving the highest value of 2.21×10^{-5} S cm^{-1} at 40 °C, comparable to the conductivity reported for $LiBH_4$ infiltrated in mesoporous Al_2O_3[33]. In contrast, $LiBH_4$-BM displayed a much lower conductivity of 6.48×10^{-7} S cm^{-1}, only slightly higher than that of pristine $LiBH_4$. All zeolite-$LiBH_4$ composites, therefore, exhibited superior conductivity compared with $LiBH_4$-BM, with the 720-$LiBH_4$ (1:2) sample delivering the highest ionic conductivity. However, excessive zeolite loading led to reduced ionic conductivity, likely due to the insulating nature of zeolites, which hinders Li^+ transport

pathways. For example, at a 2:1 mass ratio, the conductivity of 760-$LiBH_4$ declined slightly. This behavior can be rationalized by considering the distribution of $LiBH_4$ within the zeolite framework: at low zeolite content, $LiBH_4$ fills the pores and forms a continuous interfacial network, while at excessive zeolite content, $LiBH_4$ becomes isolated within the framework, disrupting conduction pathways. Consequently, the ionic conductivity of zeolite-$LiBH_4$ composites increases with zeolite addition up to an optimal ratio, beyond which it decreases due to overloading.

Previous studies have demonstrated that the ionic conductivity of $LiBH_4$ can be enhanced by incorporating oxide compounds such as SiO_2 and Al_2O_3.[6,19,34,35] However, the degree of enhancement varies depending on the chemical composition and the structural characteristics of the insulating additives. Hiroki *et al.*[35] highlighted that the morphology and interface structure of Al_2O_3 significantly impact the lithium ion conductivity. In this work, zeolites proved highly effective in increasing the conductivity of $LiBH_4$. At 80 °C, the 760-$LiBH_4$ composite achieved its maximum conductivity of 6.19×10^{-5} S cm^{-1} at a 1:1 mass ratio, whereas the 720-$LiBH_4$ composite reached 1.53×10^{-4} S cm^{-1} at a 1:2 ratio, the highest value among all zeolite-$LiBH_4$ composites, approximately two orders of magnitude higher than that of $LiBH_4$-BM （6.49×10^{-6} S cm^{-1}）. By contrast, $LiBH_4$-BM exhibited an initial conductivity of ~10^{-7} S cm^{-1} at 25 ℃, which sharply increased to ~10^{-3} S cm^{-1} near 120 ℃ due to its phase transition. At

elevated temperatures, the ionic conductivity of the zeolite-$LiBH_4$ composites approached that of $LiBH_4$-BM, indicating that $LiBH_4$ itself dominates the charge transport in this regime.

The effect of ball-milling duration on the conductivity of the composites was further investigated. Taking 720-$LiBH_4$ (1:2) as an example, the ionic conductivity initially increased and then decreased with prolonged milling. As shown in **Fig. S3.4**, the sample milled for 4 hours exhibited the highest ionic conductivity of 1.53×10^{-4} S cm^{-1} at 80 °C, surpassing those obtained at both shorter and longer milling durations. Comparison with other zeolite-$LiBH_4$ composite systems further confirms that 720-$LiBH_4$ (1:2) milled for 4 hours demonstrates the most pronounced enhancement in ionic conductivity due to their higher surface area and the greatest potential for practical application in this study.

Based on EIS results at various temperatures, the activation energies (E_a) of the composites in the low-temperature (LT) zone (25-110 ℃) were determined by linear fitting of the data shown in **Fig. 3.2b** using the Arrhenius equation (**eq 1**). The E_a of the zeolite-$LiBH_4$ composites ranged from 0.49 to 0.70 eV, all substantially lower than that of $LiBH_4$-BM (0.75 eV). This reduction in energy barrier highlights the role of the zeolite framework in promoting Li^+ diffusion. Among the 720-$LiBH_4$ composites, the lowest activation energy (0.54 eV) was observed for 720-$LiBH_4$ (1:2) (**Fig. 3.2(c)**), while the 760-$LiBH_4$ composite exhibited its minimum (0.43 eV) at a 1:1 ratio, consistent with its

highest ionic conductivity. (**Fig. 3.2(d)**) These results suggest that physical properties such as specific surface area and Si/Al ratio affect not only the ionic conductivity but also the activation energy. Based on the above results, 720-$LiBH_4$ (1:2), which combined the highest ionic conductivity with the lowest activation energy, was selected along with pristine $LiBH_4$ for subsequent electrochemical performance evaluations.

BET and TGA analysis

This conductivity enhancement is attributed to the structural characteristics revealed by nitrogen adsorption/desorption isotherms (**Fig. 3.3**). After incorporating $LiBH_4$ into the zeolite scaffold, the nitrogen adsorption amounts are remarkably decreased. The adsorption isotherms of 720-$LiBH_4$ (1:2) and 760-$LiBH_4$ (1:2) presented distinct hysteresis loops in the P/P_0 range 0.7-1.0, which is indicative of combined mesoporous and microporous structures in the zeolite-$LiBH_4$ composites. The Brunauer-Emmett-Teller (BET) surface area of 720-$LiBH_4$ (1:2) is 74.11 $m^2\ g^{-1}$, which is higher than that of 760-$LiBH_4$ (1:2) (51.52 $m^2\ g^{-1}$) but lower than that of pristine zeolite CVB720 and CVB760 of 804 $m^2\ g^{-1}$ and 754 $m^2\ g^{-1}$, respectively.(**Fig. S3.5**). The Barrett-Joyner-Halenda (BJH) pore-size distribution revealed average pore sizes of ~3.05 and 2.68 nm for 760-$LiBH_4$ (1:2) and 720-$LiBH_4$ (1:2), respectively (**Fig. 3.3(b)**). These unique structural features, particularly the preserved mesoporosity and relatively high surface area, are expected to enhance the electrolyte-electrode interface and thereby facilitate ionic conduction.

Thermogravimetric analysis (TGA) was performed to evaluate the thermal stability of 720-$LiBH_4$ (1:2) (**Fig. S3.6**). The composite exhibited negligible weight loss below 100 °C, indicating stable thermal behavior in this range. Optical images further reveal that the 720-$LiBH_4$ (1:2) pellet maintained a fully solid state without visible softening or melting at 80 ℃ (**Fig. S3.7**). These observations collectively demonstrate the favorable thermal stability of 720-$LiBH_4$ (1:2).

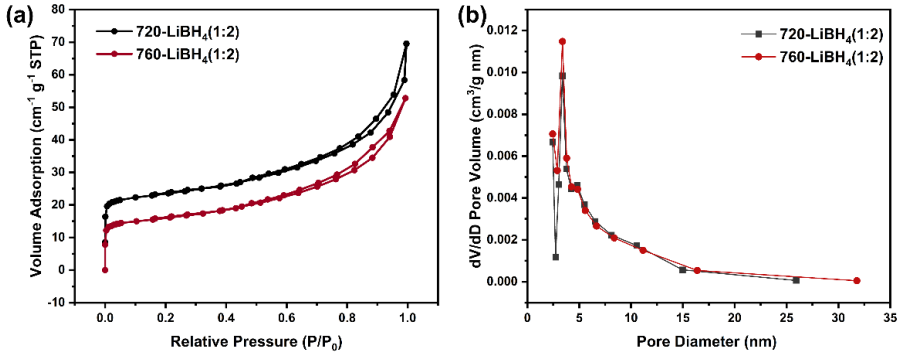

Fig. 3.3 (a) Nitrogen physisorption isotherms for 720-$LiBH_4$ (1:2) and 760-$LiBH_4$ (1:2); **(b)** pore-size distribution plots for 720-$LiBH_4$ (1:2) and 760-$LiBH_4$ (1:2).

Electrochemical performance for solid-state electrolyte

To evaluate the practical electrochemical performance of 720-$LiBH_4$(1:2) in Lithium batteries, we firstly assessed the electrochemical properties of the 720-$LiBH_4$ (1:2) composite, its electronic conductivity, and Li^+ transference number were measured using a symmetric stainless-steel cell. As shown in **Fig. 3.4(a)**, the steady-state current

under a polarization voltage of 0.5 V for 30,000 s at 80 °C yielded an electronic conductivity of 6.16×10^{-10} S cm^{-1}. This value is nearly six orders of magnitude lower than the Li^+ ionic conductivity, confirming negligible electronic conductivity in the composite. The calculated Li^+ transference number exceeded 0.999, indicating that Li^+ migration overwhelmingly dominates the overall conductivity. Such extremely low electronic conductivity is highly advantageous for suppressing lithium dendrite growth at the negative electrode and improving the cycling stability of solid-state batteries.

To explore the application potential of 720-$LiBH_4$ (1:2) as a solid-state electrolyte in lithium-based batteries, its electrochemical stability and compatibility with Li metal were examined. **Fig. 3.4(b)** shows the LSV curves of the Li|720-$LiBH_4$ (1:2) |SS cell recorded from open-circuit voltage (OCV) to 4.0 V at a scan of 0.1 mV s^{-1} at 80 ℃. The anodic scan shows the onset of oxidation at ~ 2.86 V (*vs.* Li^+/Li), which is wider than that of pristine $LiBH_4$ (~ 2.0 V) (*vs.* Li^+/Li)[33] and higher than the value reported for $LiBH_4$-MgO composite (2.3 V *vs.* Li^+/Li)[36]. In the cathodic scan, reduction occurs at ~ 0.22 V (*vs.* Li^+/Li). These results indicate that 720-$LiBH_4$ (1:2) remains electrochemically stable within the potential range from 0.22 to 2.86 V (*vs.* Li^+/Li), thereby making it suitable for integration with a wider variety of cathode materials in all-solid-state batteries.

The lithium dendrite suppression capability and cycling stability of the 720-$LiBH_4$ (1:2) composite were further evaluated by galvanostatic

charge-discharge (GCD) testing using a symmetric Li|720-$LiBH_4$ (1:2) |Li cell at 80 °C. As shown in **Fig. 3.4(c)**, the voltage profile of the Li|720-$LiBH_4$ (1:2) |Li cell exhibited remarkable long-term stability, maintaining a consistently low overpotential of ~10 mV and stable cycling for over 270 hours without noticeable voltage fluctuations at a current density of 0.1 mA cm^{-2}. In contrast, the Li|$LiBH_4$-BM|Li symmetric cell failed after only 15 h due to severe interfacial instability and short-circuiting, demonstrating its poor interfacial compatibility. These results suggest that the incorporation of zeolite into $LiBH_4$ effectively mitigates interfacial instability between $LiBH_4$ and lithium metal, thereby significantly improving interfacial compatibility. More impressively, at a higher current density of 0.5 mA cm^{-2} (**Fig. 3.4(d)**), the Li|720-$LiBH_4$ (1:2) |Li symmetric cell maintained stable cycling for over 160 h, further confirming the robust and stable interface formed between lithium metal and the zeolite-$LiBH_4$ composite electrolyte. To determine the maximum sustainable operating current density, the critical current density (CCD) was measured (**Fig. S3.8**). The CCD for the symmetric Li|720-$LiBH_4$ （1:2） |Li cell reached 2.8 mA cm^{-2} at 80 °C, which is higher than those reported for many other borohydride composite solid electrolytes[34,37,38].This excellent dendrite suppression capability and high CCD underscore the promise of 720-$LiBH_4$ (1:2) as an ideal model system for studying interfacial stabilization in borohydride-based solid electrolytes.”

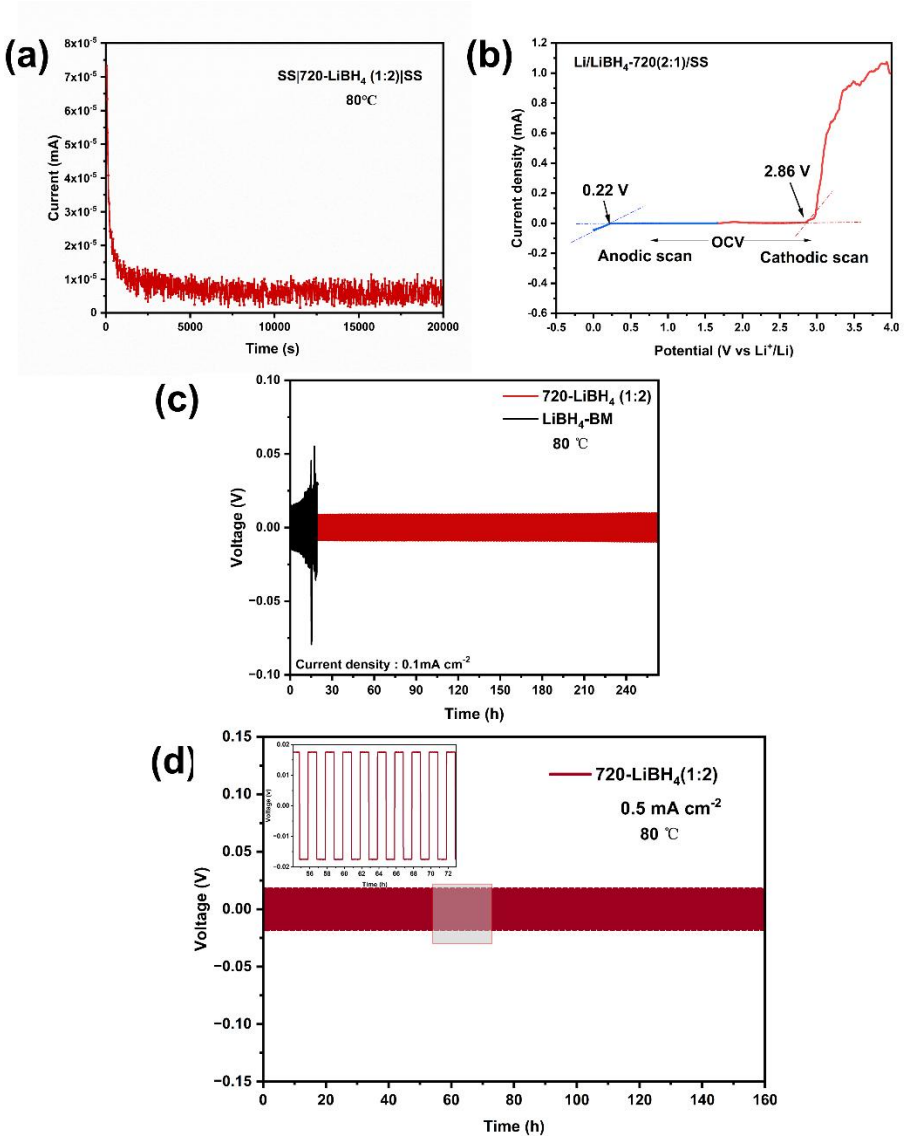

Fig. 3.4. (a) DC polarization curve of the as-prepared 720-$LiBH_4$ (1:2) composite; **(b)** LSV curve of 720-$LiBH_4$ (1:2); Galvanostatic Li plating/stripping profiles of the Li|720-$LiBH_4$ (1:2)|Li cell (red) and the Li|$LiBH_4$-BM|Li cell (black) at 80 °C: **(c)** at 0.1 mA cm^{-2} and (d) at 0.5 mA cm^{-2}.

Finally, to explore the practical applicability of 720-$LiBH_4$ (1:2) as a solid-state electrolyte in Li-metal batteries, its electrochemical

performance was investigated in a full-cell configuration using $Li_4Ti_5O_{12}$ (LTO) as the cathode and lithium metal as the anode. Galvanostatic charge-discharge tests were conducted at 80 °C and 100 °C under a current density of 0.1 C (1C= 175mAh g^{-1}), and the results are shown in **Fig. 3.5**. At 80 °C, the LTO|720-$LiBH_4$ (1:2) |Li cell exhibited typical charge-discharge behavior. The initial discharge capacity reached 164.4 mAh g^{-1}, corresponding to 94% of the theoretical capacity of LTO, albeit with a relatively large polarization. However, the reversible specific capacity decreased to approximately 80 mAh g^{-1} after 10 cycles, likely due to interfacial resistance accumulation and incomplete Li^+ transport pathways at this moderate temperature. Notably, when the operating temperature was increased to 100 ℃, the electrochemical performance was significantly improved. At the same current density, the LTO|720-$LiBH_4$(1:2) |Li cell displayed well-defined and flat charge/discharge plateaus at approximately 1.55 V with much lower polarization. The discharge capacity remained close to the theoretical value of ~172 mAh g^{-1} for up to 8 cycles, indicating excellent Li^+ transport kinetics and stable electrode–electrolyte interfaces at elevated temperature. These results demonstrate the good short-term interfacial compatibility of 720-$LiBH_4$ (1:2) with LTO electrodes, while further improvements in cycling performance are expected through electrode and interface optimization.

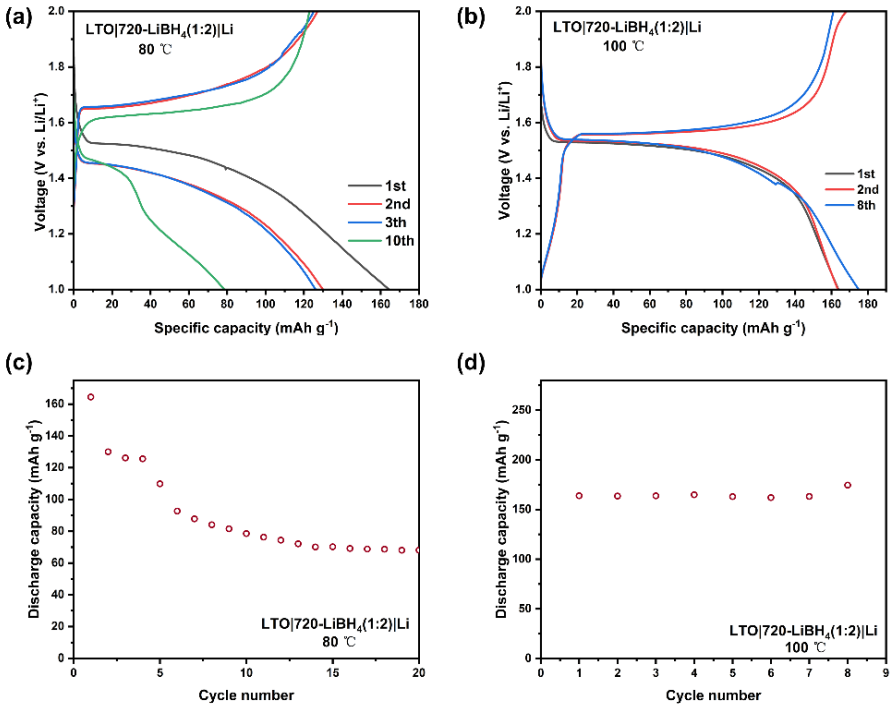

Fig. 3. 5. (a) Discharge-charge curves at 1st, 2nd, 3rd, and 10th cycle at 0.1 C at 80 °C and **(c)** cycling performance; **(b)** Discharge-charge curves at 1st, 2nd, and 8th cycle at 0.1 C at 100 °C and **(d)** cycling performance.

3.3 Conclusions

In summary, we have developed a series of zeolite-$LiBH_4$ composite solid-state electrolytes through a simple ball-milling approach. The results demonstrate that both the zeolite type and mass ratio play decisive roles in governing the ionic conductivity of $LiBH_4$-based electrolytes. Compared with conventional oxide additives, zeolite provides a more ordered and interactive framework and moderate

zeolite loading promotes the formation of continuous Li^+ transport pathways, thereby enhancing conductivity and lowering the activation energy for Li^+ migration. Among the investigated compositions, the 720-$LiBH_4$ (1:2) composite exhibited the best performance, delivering an ionic conductivity of approximately 1.53×10^{-4} S cm^{-1} at 80 °C, excellent interfacial stability against lithium metal, and long-term cycling stability exceeding 200 hours. Notably, this composite also showed outstanding compatibility with the $Li_4Ti_5O_{12}$ cathode, retaining near-theoretical discharge capacities at elevated temperatures. These findings highlight zeolite-modified $LiBH_4$ as a promising solid electrolyte platform for high-performance solid-state lithium metal batteries. Looking ahead, the exploration of alternative zeolite frameworks and further optimization of composite architectures may yield even greater improvements in ionic conductivity, electrochemical stability, and cathode compatibility. This study thus provides valuable insights into the design of borohydride-based solid electrolytes for next-generation energy storage systems.

3.4 Experiment section

Synthesis

Commercial Y zeolites (CVB720 and CVB760) were obtained from Zeolyst International. CVB720 and CVB760 have the Si/Al ratio of 30 and 60, respectively. $LiBH_4$ was bought from Aladdin, purity > 95%.

$LiBH_4$ was used as received without further purification. Zeolite Y type): CVB 720 and CVB 760 zeolites were dried under dynamic vacuum at 250 ℃ for 12 hours before use.

Zeolite-$LiBH_4$ composite was synthesized by Ball-milling. 720-$LiBH_4$ and 760-$LiBH_4$ were prepared with different kinds of mass ratios (A: B) of 1:1, 1:2, 1:3, and 2:1. For each experiment, 0.8g of the mixture was loaded into a stainless-steel milling jar in a glove box filled with argon. The ball-to-sample weight ratio was kept at 13:1. Two compositions of $LiBH_4$ and 720, 760 were mechanically milled at 400 rpm for 4 hours with a planetary ball mill (XQM-0.4A, Changsha). All samples were milled in cycles of 3 min milling followed by 2 min breaks to overcome heating effects. For comparison, $LiBH_4$ was ball-milled (named $LiBH_4$-BM) under the same conditions to evaluate the effect of mechanochemical treatment on the Li-ion conductivity. After milling treatment, the mixtures were collected in an Argon-filled glove box for further structural and property characterizations. All manipulations of the samples during the experiment were conducted

within an Argon atmosphere in a glove box ($p(O_2) < 0.1$ ppm, $p(H_2O) < 0.1$ ppm)

Characterization

X-ray diffraction (XRD) measurements were carried out with two Incoatec X-ray generators (mixed Mo Kα radiation, weighted average λ = 0.71073 Å) with mar345 operated at 50 kV and 1000 μA. XRD sample preparation is performed in an Argon glovebox. A small number of samples were placed in the 0.7mm glass capillary tubes and transferred to the diffractometer. Measured samples were not reused for other characterization techniques. The data were integrated by the Fit2D software (ESRF) to analyze.

Infrared spectra were collected between 400 and 4000 cm^{-1} by FTIR with an attenuated total reflectance accessory (ATR/FTIR) on a Bruker α II spectrometer in an Argon-filled glovebox. SEM observations were conducted on an FEI Sirion 200 equipped with an EDS analysis unit. The morphology of the zeolite samples was characterized with a scanning electron microscope (SEM, ZEISS Gemini 300, Germany).
TGA analysis was performed on a NETZSCH STA 449 F3 Jupiter instrument equipped with a stainless-steel oven, housed inside an argon-filled glovebox. Measurements were performed at a heating rate of 5 K min^{-1} under constant Ar flow (total flow of 100 mL min^{-1}), from 25 to 300 °C.

The surface areas (S_{BET}) and total pore volumes (Vp) of composites were obtained by N_2 adsorption at 77k in a JW-BK200C automatic surface analyzer (JWGB Sci & Tech, Beijing). The specific surface areas of composites were derived by fitting with a Brunauer-Emmett-Teller isotherm, and the total pore volume was obtained from the absorbed volume of nitrogen at p/p_0=0.95.

Electrochemical Test

The ionic conductivity of solid-state electrolytes (SSEs) was measured by electrochemical impedance spectroscopy (EIS). Nyquist plots were recorded in the frequency range between 7 MHz and 100 mHz with an AC voltage of 100 mV. The SSEs were pressed into pellets with a diameter of 9 mm and a thickness of 0.5~1.0 mm approximately under the pressure of 600 MPa. The measurement pellets were prepared in a symmetric cell which consists of two blocked electrodes (stainless steel, SS) and one SSE, to assemble SS|SSE|SS. All measurements were carried out within the temperature range from 25 to 120 ℃ with 0.33 ℃ min^{-1} at an interval of 10 ℃. Each temperature point was required for a holding of 30 minutes to ensure data reproducibility of the measurement. The ionic conductivities of SEEs are determined using Eq. (1)

$$\sigma = \frac{L}{RS} \quad (1)$$

Where L (in cm) is the thickness of the SSEs, R (in Ω) is the value of bulk resistance extracted from the complex EIS pots and S (in cm^2)

is the area of the SSEs. The electrochemical stability of SSEs was investigated by linear sweep voltammetry (LSV). LSV was conducted for the SS|SSE|Li coin cell at a sweep rate of 0.1 mV s^{-1} over a potential range of open circuit potential (OCV) to 4.0 V and OCV to 0 V (*vs.* Li/Li^{+}).

The electronic conductivities of 720-$LiBH_4$ were evaluated by a CHI660e (Shanghai Chenhua Co. Ltd) electrochemical workstation via direct-current (DC) polarization. For DC tests, pellets were covered by two stainless steel electrodes on both sides with a DC voltage of 0.5 V at 80 ℃. The resistance R can be calculated by the working voltage and steady current. Then electronic conductivity can be obtained by eq. (1) and (2).

$$R = \frac{U}{I} \qquad (2)$$

The activation energy E_a can be calculated according to the Nernst-Einstein equation and the Arrhenius equation (3).

$$\ln \sigma T = \frac{E_a}{K_B T} + C \qquad (3)$$

Where σ is conductivity, C is the pre-exponential factor, K_B is Boltzmann's constant, and T is the temperature (K).

The stability of 720-$LiBH_4$ (1:2) against Li metal was evaluated by assembling symmetric Li|720-$LiBH_4$ (1:2) |Li cells at a current density of 0.1 mA cm^{-2} and 0.5 mA cm^{-2} at 80 ℃. For all-solid-state batteries assemblies, Li foil (9 mm) was used as the counter electrode. The working cathodes material was prepared by hand grinding of 720-

$LiBH_4$ (1:2), $Li_4Ti_5O_{12}$ (LTO) and Super P with a mass ratio of 40: 40: 20 for 20 min. Typically, 60 mg of 720-$LiBH_4$ (1:2) powder was pressed into a pellet at 500 MPa, then 4 mg of working cathode material was pressed on the side of the electrolyte, and 9 mm diameter Li foil was covered on the other side in turn. Li|720-$LiBH_4$ (1:2) |LTO cells were galvanostatic charged and discharged in a potential range from 1.0 V to 2.0 V (*vs* Li^+/Li) by using Neware battery test systems.

3.5 Support information

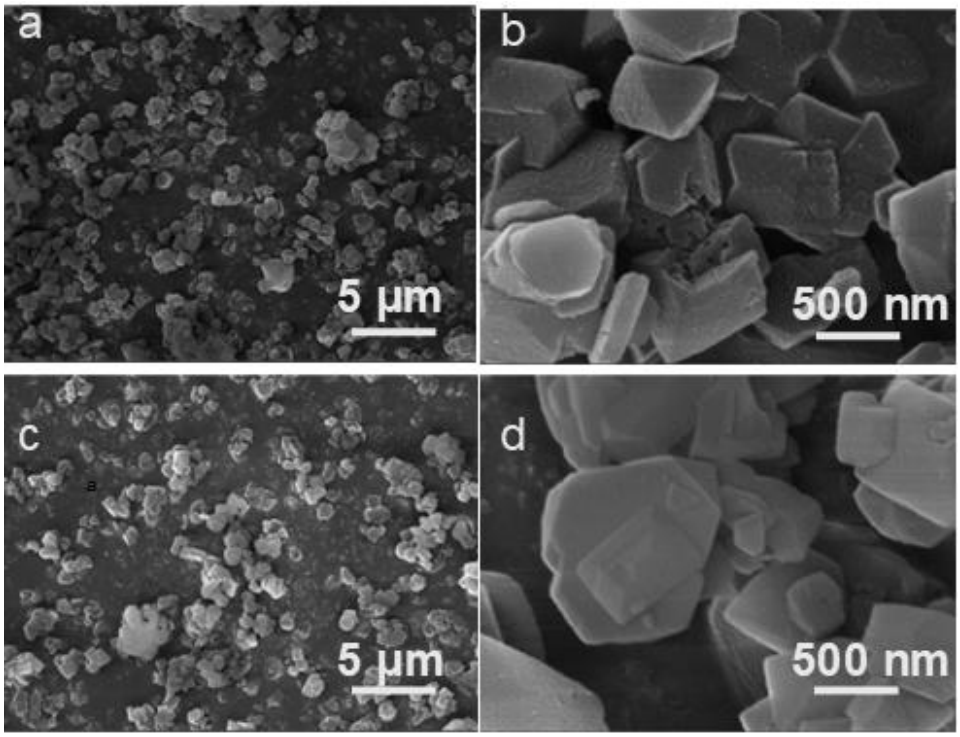

Fig. S3.1. SEM image of zeolite (a-b) 720 and (c-d) 760.

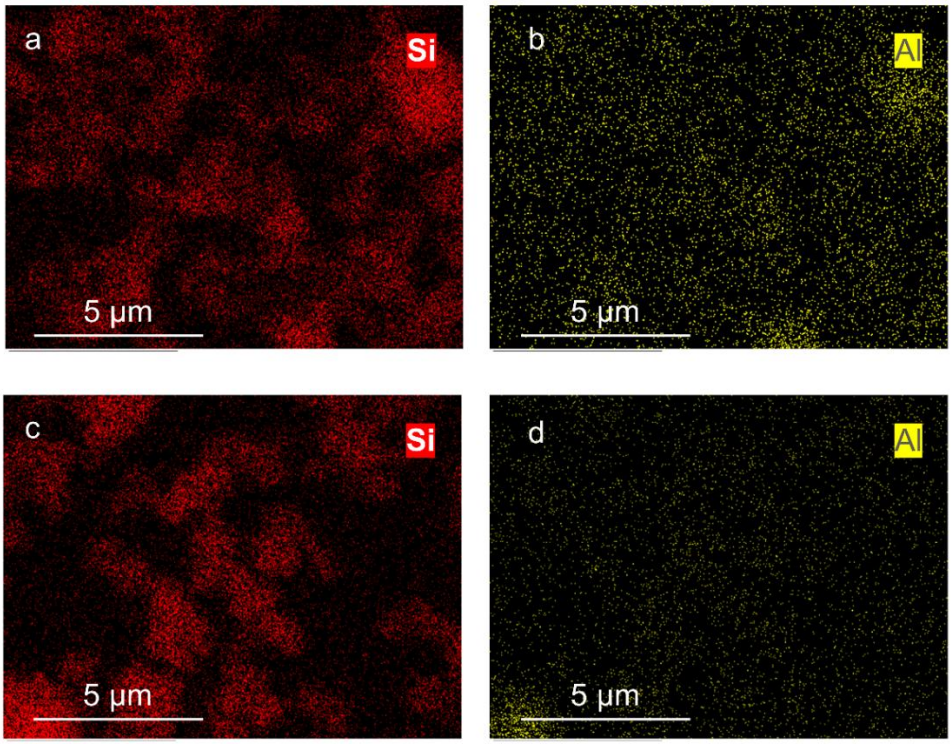

Fig. S3.2. EDS mapping of (a-b) 720 and (c-d) 760.

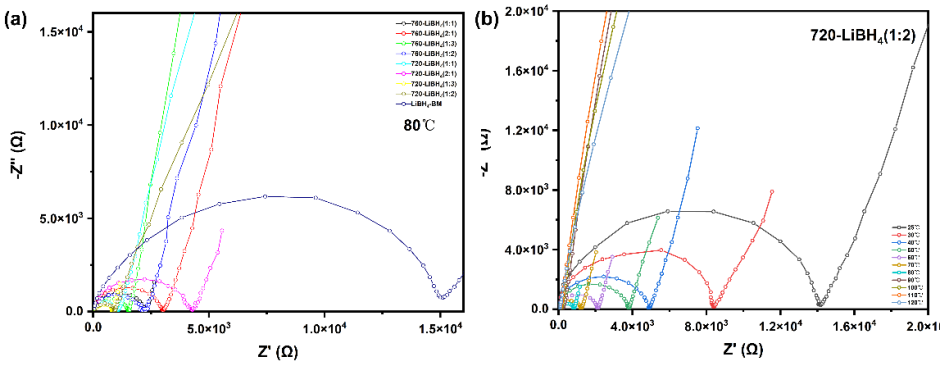

Fig. S3.3. (a) EIS plot of 720-$LiBH_4$ (1:2) materials at different temperatures; **(b)** EIS plot of $LiBH_4$-BM and zeolite-$LiBH_4$ composites at 80 ℃.

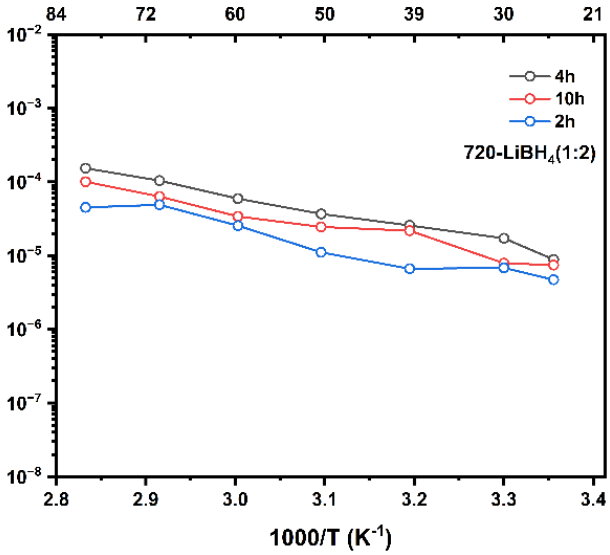

Fig. S3.4. Temperature-dependent ionic conductivity for 720-$LiBH_4$ (1:2) for various ball-milling time.

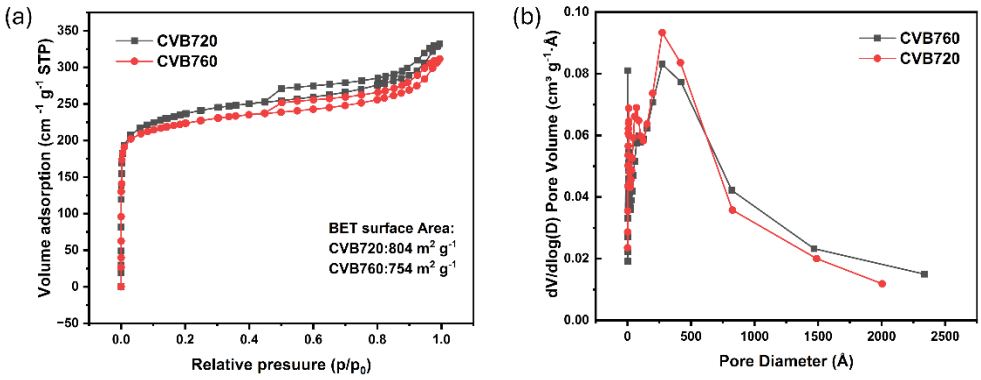

Fig. S3.5 (a) Nitrogen physisorption isotherms for CVB720 and CVB760. (b) Pore diameter of CVB720 and CVB760.

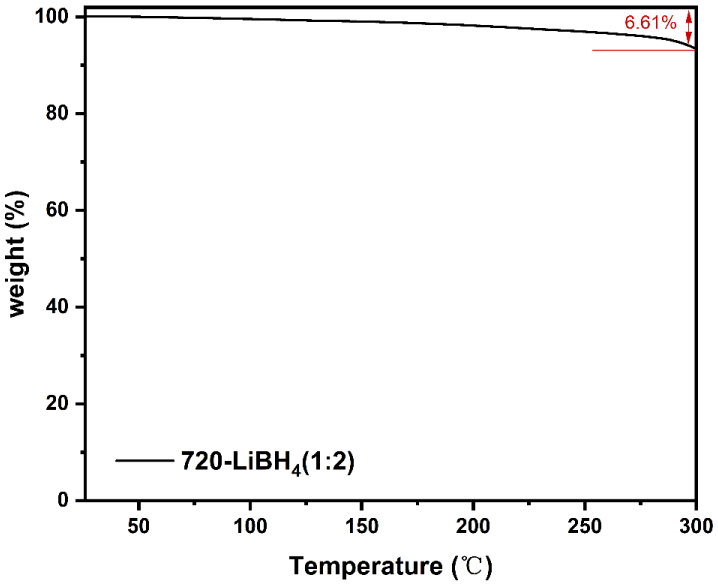

Fig. S3.6. TGA curve of 720-$LiBH_4$ (1:2) from RT to 300 ℃.

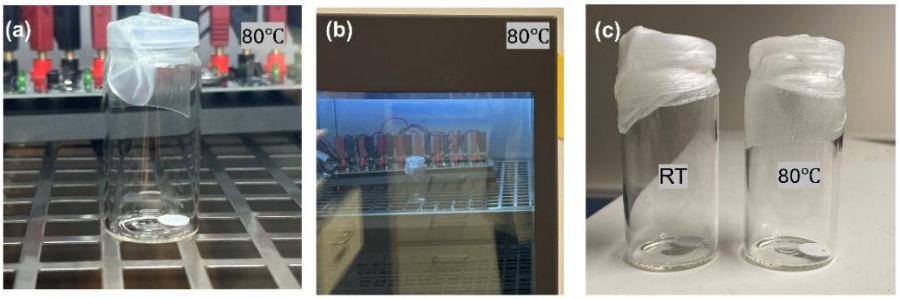

Fig. S3.7. Optical photo of 720-$LiBH_4$ (1:2) pellets at RT and 80 ℃. It remains solid state during the heating process from room temperature to 80 ℃.

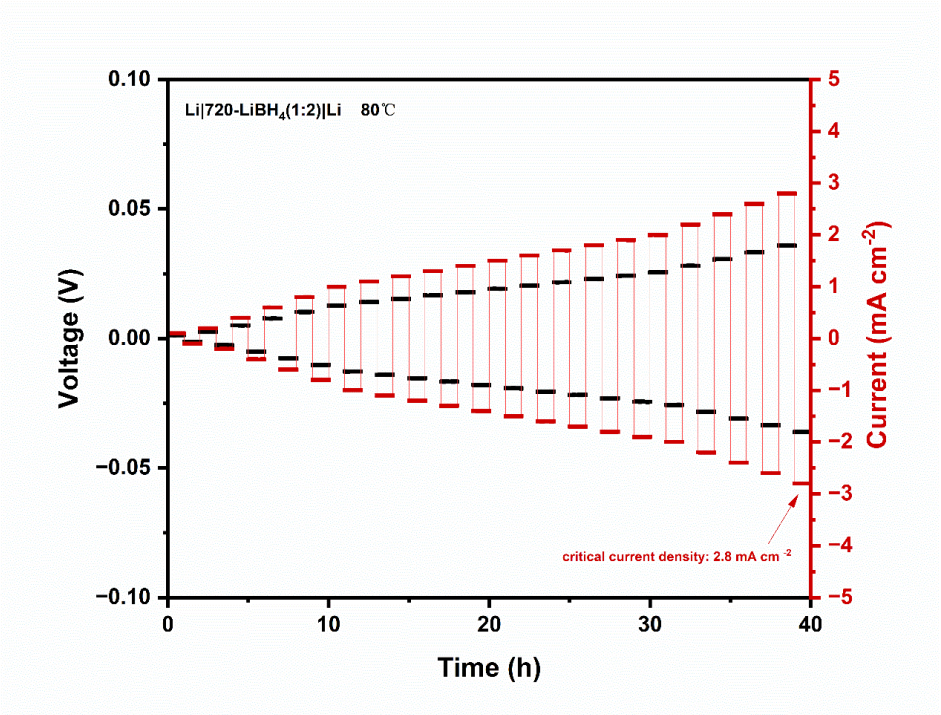

Fig. S3.8. Critical current density test of the Li|720-$LiBH_4$ (1:2) |Li cell at 80 ℃.

Table S3.1. Physical properties of zeolite 720 and 760.

	Crystallinity[a]	SiO_2/Al_2O_3	Si/Al[a]	Si/Al[b]	S_{BET}[a]	S_{meso}[a]	S_{BET}[c]	$V_{micropore,}$[b]
		ratio	ratio(X)	ratio(X)	m^2/g	m^2/g	m^2/g	cm^3/g
CBV720	71	30	16.0	13.0	840	267	785.3	0.273
CBV760	64	60	28.0	30.0	805	261	783.2	0.250

[a] 10.1016/j.micromeso.2020.110114, 10.1002/cphc.202000062; [b]10.1021/jp953006x, ICP calculated for HY (FAU zeolite) with formula $H_x(AlO_2)_x(SiO_2)_{192-x}$; [c] 10.1080/09593330.2019.1650833;

Table S3.2. Ionic conductivities of samples at different temperatures.

Sample	$\sigma_{40°C}$ (S cm^{-1})	$\sigma_{60°C}$ (S cm^{-1})	$\sigma_{80°C}$ (S cm^{-1})	$\sigma_{100°C}$ (S cm^{-1})	$\sigma_{120°C}$ (S cm^{-1})
720-$LiBH_4$(1:1)	1.13×10^{-5}	2.18×10^{-5}	6.10×10^{-5}	4.26×10^{-4}	1.76×10^{-3}
720-$LiBH_4$(1:2)	2.57×10^{-5}	5.93×10^{-5}	1.53×10^{-4}	9.67×10^{-4}	2.22×10^{-3}
720-$LiBH_4$(1:3)	1.36×10^{-5}	4.53×10^{-5}	1.18×10^{-4}	5.00×10^{-4}	1.55×10^{-3}
720-$LiBH_4$(2:1)	6.55×10^{-6}	3.14×10^{-5}	6.28×10^{-5}	1.92×10^{-4}	1.41×10^{-3}
760-$LiBH_4$(1:1)	1.91×10^{-5}	2.52×10^{-5}	6.10×10^{-5}	1.61×10^{-4}	1.99×10^{-3}
760-$LiBH_4$(1:2)	8.41×10^{-6}	1.46×10^{-5}	4.89×10^{-5}	3.59×10^{-4}	1.98×10^{-3}
760-$LiBH_4$(1:3)	7.54×10^{-6}	1.49×10^{-5}	5.07×10^{-5}	1.69×10^{-4}	1.38×10^{-3}
760-$LiBH_4$(2:1)	4.38×10^{-6}	2.00×10^{-5}	4.03×10^{-5}	1.36×10^{-4}	1.87×10^{-3}
$LiBH_4$-BM	6.48×10^{-7}	2.87×10^{-6}	6.49×10^{-6}	4.65×10^{-5}	1.23×10^{-3}

3.6 References

1. Manthiram, A., Yu, X. & Wang, S. Lithium battery chemistries enabled by solid-state electrolytes. *Nat. Rev. Mater.* **2**, 1–16 (2017).

2. Wan, H. *et al.* Critical interphase overpotential as a lithium dendrite-suppression criterion for all-solid-state lithium battery design. *Nat. Energy* **8**, 473–481 (2023).

3. De Kort, L. M. *et al.* Designing Highly Conductive Sodium-Based Metal Hydride Nanocomposites: Interplay between Hydride and Oxide Properties. *Adv. Funct. Mater.* **33**, 2209122 (2023).

4. Kim, J.-S., Kim, D. W., Jung, H. T. & Choi, J. W. Controlled Lithium Dendrite Growth by a Synergistic Effect of Multilayered Graphene Coating and an Electrolyte Additive. *Chem. Mater.* **27**, 2780–2787 (2015).

5. Zou, Z. *et al.* Mobile Ions in Composite Solids. *Chem. Rev.* **120**, 4169–4221 (2020).

6. Zhu, M. *et al.* In Situ Formed Li–B–H Complex with High Li-Ion Conductivity as a Potential Solid Electrolyte for Li Batteries. *ACS Appl. Mater. Interfaces* **11**, 14136–14141 (2019).

7. Matsuo, M., Nakamori, Y., Orimo, S., Maekawa, H. & Takamura, H. Lithium superionic conduction in lithium borohydride

accompanied by structural transition. *Appl. Phys. Lett.* **91**, 224103 (2007).

8. Takahashi, K. *et al.* All-solid-state lithium battery with $LiBH_4$ solid electrolyte. *J. Power Sources* **226**, 61–64 (2013).

9. Hu, L. *et al.* Interface Modification and Halide Substitution To Achieve High Ionic Conductivity in $LiBH_4$ -Based Electrolytes for all-Solid-State Batteries. *ACS Appl. Mater. Interfaces* **14**, 1260–1269 (2022).

10. Gulino, V., de Kort, L., Ngene, P., de Jongh, P. & Baricco, M. Combined Effect of Halogenation and SiO_2 Addition on the Li-Ion Conductivity of $LiBH_4$. *Inorganics* **11**, 459 (2023).

11. Maekawa, H. *et al.* Halide-Stabilized $LiBH_4$, a Room-Temperature Lithium Fast-Ion Conductor. *J. Am. Chem. Soc.* **131**, 894–895 (2009).

12. Gulino, V. *et al.* Phase Stability and Fast Ion Conductivity in the Hexagonal $LiBH_4$–LiBr–LiCl Solid Solution. *Chem. Mater.* **31**, 5133–5144 (2019).

13. Yan, Y. *et al.* Ammonia-assisted fast Li-ion conductivity in a new hemiammine lithium borohydride, $LiBH_4 \cdot 1/2NH_3$. *Chem. Commun.* **56**, 3971–3974 (2020).

14. Yan, Y. *et al.* A Lithium Amide-Borohydride Solid-State Electrolyte with Lithium-Ion Conductivities Comparable to Liquid Electrolytes. *Adv. Energy Mater.* **7**, 1700294 (2017).

15. Liu, H. *et al.* Incorporation of Ammonia Borane Groups in the Lithium Borohydride Structure Enables Ultrafast Lithium Ion Conductivity at Room Temperature for Solid-State Batteries. *Chem. Mater.* **32**, 671–678 (2020).

16. Zhao, W. *et al.* Li-Ion Conductivity Enhancement of $LiBH_4 \cdot x\ NH_3$ with *In Situ* Formed Li_2O Nanoparticles. *ACS Appl. Mater. Interfaces* **13**, 31635–31641 (2021).

17. Blanchard, D. *et al.* Nanoconfined $LiBH_4$ as a Fast Lithium Ion Conductor. *Adv. Funct. Mater.* **25**, 184–192 (2015).

18. Lefevr, J., Cervini, L., Griffin, J. M. & Blanchard, D. Lithium Conductivity and Ions Dynamics in $LiBH_4/SiO_2$ Solid Electrolytes Studied by Solid-State NMR and Quasi-Elastic Neutron Scattering and Applied in Lithium–Sulfur Batteries. *J. Phys. Chem. C* **122**, 15264–15275 (2018).

19. Gulino, V., De Kort, L., Ngene, P., De Jongh, P. & Baricco, M. Combined Effect of Halogenation and SiO_2 Addition on the Li-Ion Conductivity of LiBH4. *Inorganics* **11**, 459 (2023).

20. Ngene, P., Adelhelm, P., Beale, A. M., De Jong, K. P. & De Jongh, P. E. $LiBH_4$/SBA-15 Nanocomposites Prepared by Melt Infiltration under Hydrogen Pressure: Synthesis and Hydrogen Sorption Properties. *J. Phys. Chem. C* **114**, 6163–6168 (2010).

21. Zettl, R. *et al.* Conductor–Insulator Interfaces in Solid Electrolytes: A Design Strategy to Enhance Li-Ion Dynamics in Nanoconfined $LiBH_4/Al_2O_3$. *J. Phys. Chem. C* **125**, 15052–15060 (2021).

22. Zeng, S. *et al.* Stabilization of fast lithium-ionic conduction phase of nanaoconfined $LiBH_4$ for lithium metal solid-state batteries. *Chem. Commun.* **61**, 929–932 (2025).

23. Gulino, V., Barberis, L., Ngene, P., Baricco, M. & de Jongh, P. E. Enhancing Li-Ion Conductivity in $LiBH_4$-Based Solid Electrolytes by Adding Various Nanosized Oxides. *ACS Appl. Energy Mater.* **3**, 4941–4948 (2020).

24. Shamzhy, M., Opanasenko, M., Concepción, P. & Martínez, A. New trends in tailoring active sites in zeolite-based catalysts. *Chem. Soc. Rev.* **48**, 1095–1149 (2019).

25. Kosinov, N., Gascon, J., Kapteijn, F. & Hensen, E. J. M. Recent developments in zeolite membranes for gas separation. *J. Membr. Sci.* **499**, 65–79 (2016).

26. Barbosa, J. C. *et al.* Metal–organic frameworks and zeolite materials as active fillers for lithium-ion battery solid polymer electrolytes. *Mater. Adv.* **2**, 3790–3805 (2021).

27. Ding, Z. *et al.* Integrate multifunctional ionic sieve lithiated X zeolite-ionic liquid electrolyte for solid-state lithium metal batteries with ultralong lifespan. *Chem. Eng. J.* **433**, 133522 (2022).

28. Ding, Z. *et al.* A flexible solid polymer electrolyte enabled with lithiated zeolite for high performance lithium battery. *Nano Res.* **16**, 9443–9452 (2023).

29. Hong, M. *et al.* Ultrafast Sintering of Solid-State Electrolytes with Volatile Fillers. *ACS Energy Lett.* **6**, 3753–3760 (2021).

30. Chi, X. *et al.* A highly stable and flexible zeolite electrolyte solid-state Li–air battery. *Nature* **592**, 551–557 (2021).

31. Chang, C.-Y., Shen, Z.-Y. & Lee, M.-T. In-situ Removal of Ammonia from Water of Live Transports of Fish. *J. Adv. Agric. Technol. Vol* **6**, (2019).

32. Lang, J., Gerhauser, A., Filinchuk, Y., Klassen, T. & Huot, J. Differential Scanning Calorimetry (DSC) and Synchrotron X-ray Diffraction Study of Unmilled and Milled $LiBH_4$: A Partial

Release of Hydrogen at Moderate Temperatures. *Crystals* **2**, 1–21 (2012).

33. Zeng, S. *et al.* Stabilization of fast lithium-ionic conduction phase of nanaoconfined $LiBH_4$ for lithium metal solid-state batteries. *Chem. Commun.* **61**, 929–932 (2025).

34. Ngene, P., Adelhelm, P., Beale, A. M., De Jong, K. P. & De Jongh, P. E. $LiBH_4$/SBA-15 Nanocomposites Prepared by Melt Infiltration under Hydrogen Pressure: Synthesis and Hydrogen Sorption Properties. *J. Phys. Chem. C* **114**, 6163–6168 (2010).

35. Mizuochi, H. *et al.* Effects of Oxide Morphology on Lithium-Ion Conductivity of $LiBH_4$–Al_2O_3 Composites. *ACS Appl. Energy Mater.* **8**, 518–528 (2025).

36. Gulino, V. *et al.* Room-Temperature Solid-State Lithium-Ion Battery Using a $LiBH_4$–MgO Composite Electrolyte. *ACS Appl. Energy Mater.* **4**, 1228–1236 (2021).

37. Gao, Y. *et al.* Amorphous Dual-Layer Coating: Enabling High Li-Ion Conductivity of Non-Sintered Garnet-Type Solid Electrolyte. *Adv. Funct. Mater.* **31**, 2009692 (2021).

38. Zeng, S. *et al.* Realizing fast Li-ion conduction of Li_3PO_4 solid electrolyte at low temperature by mechanochemical formation of lithium-containing dual-shells. *Mater. Adv.* **4**, 2780–2784 (2023).

Chapter 4 Zeolite-Modified $Na_2B_{12}H_{12}$ Solid-State Electrolytes for Sodium-based batteries

Abstract

Solid-state sodium batteries are promising for large-scale energy storage due to the abundance and low cost of sodium. Among various solid electrolytes, *closo*-type complex hydrides such as $Na_2B_{12}H_{12}$ have shown high Na^+ conductivity, reaching 0.1 S cm^{-1} at 256 °C during a phase transition. However, achieving high conductivity near room temperature remains challenging. In this work, we developed a zeolite-$Na_2B_{12}H_{12}$ composite designed to enhance Na^+ conduction through interfacial engineering. Inspired by our previous zeolite-$LiBH_4$ system, zeolite addition enables efficient Na^+ migration through better dispersion and interfacial pathways. The optimized composite achieved a high ionic conductivity of 2.04×10^{-5} S cm^{-1} at room temperature and ~10^{-3} S cm^{-1} at 90 °C. Moreover, it exhibited stable long-term cycling in a Na‖Na symmetric cell at 80 °C, showing good compatibility with sodium metal. These results demonstrate that zeolite incorporation is a simple and effective strategy to enhance both the conductivity and interfacial stability of complex hydride electrolytes, providing new insights for the development of high-performance solid-state sodium batteries.

4.1 Introduction

Solid-state sodium batteries (SSSBs) have been regarded as potential candidates for large-scale storage devices due to their rich resource

distribution and low cost of sodium compared to Li metal[1]. However, the development of high-performance solid electrolytes remains a critical barrier to the implementation of safe and efficient SSSBs. Conventional oxide- and sulfide-based electrolytes, such as NaSICON[2], Na_3PS_4[3], and Na_3PSe_4[4], offer promising ionic conductivities but often suffer from limitations such as high processing temperatures, moisture sensitivity, and interfacial instability with sodium metal. Consequently, alternative solid electrolytes that combine high ionic conductivity, good chemical stability, and facile synthesis are urgently needed.

Among the various candidates, complex hydrides based on *closo*-type boron clusters have recently attracted attention as potential solid electrolytes for alkali-metal batteries[5–10]. Notably, $Na_2B_{12}H_{12}$ has been reported to have a superior Na^+ ion conductivity of 0.1 S cm^{-1} at 256 °C following a phase transition from its monoclinic to disorder body-centered cubic (bcc) phase[11]. Nevertheless, at near-ambient temperatures, $Na_2B_{12}H_{12}$ stabilizes in an ordered monoclinic phase with very low Na^+ conductivity (10^{-7}-10^{-8} S cm^{-1}), severely restricting its practical application. Thus, stabilizing the disordered structure or creating fast-ion conduction pathways at lower temperatures has become a key challenge.

To address this issue, several approaches have been proposed to enhance Na^+ mobility in *closo*-hydrides. Mechanical milling can reduce crystallite size and partially stabilize the high-temperature phase of

$Na_2B_{12}H_{12}$, thereby improving conductivity[12]. Other research on $Na_2B_{12}H_{12}$ mainly focuses on its polymorphic phase transitions, ionic conductivity, and composite formation with other borohydrides. For example, $Na_3NH_2B_{12}H_{12}$ can achieve 1.0×10^{-4} S cm^{-1} at 99 °C[13], and $Na_3BH_4B_{12}H_{12}$ can stabilize a high conductivity of 10^{-3} S cm^{-1} at room temperature[14]. Moreover, halide anion-substitution is also reported to markedly increase the conductivity of $Na_2B_{12}H_{12}$, as in $Na_2B_{12}H_{12-x}I_x$ with ionic conductivity approaching ~10^{-1} S cm^{-1} at 360 K[15]. While these methods can improve conductivity, they often involve anion substitution or limited structural modification. A simpler and broadly applicable method is therefore desirable.

Interfacial engineering using oxide or porous scaffold has recently emerged as a promising alternative for improving the electrochemical properties of borohydrides[16–19], However, its effectiveness strongly depends on the chemical compatibility between the hydride and the oxide scaffold. For example, early studies on $NaBH_4$ nanoconfined in mesoporous silica (MCM-41) reported only minor conductivity improvement due to extensive oxidation of BH_4^- at the silica pore walls, forming insulating borates that suppresses ion transport[20]. While recent studies on lithium closo-borates demonstrate that large, highly stable polarizable $[B_{12}H_{12}]^{2-}$ anion interacts more gently with oxide surfaces, enabling $Li_2B_{12}H_{12}$-Al_2O_3[21] to achieve a high lithium-ion conductivity 2.73×10^{-5} S cm^{-1} at 30 °C while maintaining a wide electrochemical window (~3.8V *vs*. Li^+/Li). These observations imply that *closo*-borates

may be suited for oxide-based interface engineering, yet this concept remains largely unexplored for sodium borohydrides.

Building on the insights gained in **Chapter 3,** where zeolite frameworks significantly enhance Li^+ conductivity in $LiBH_4$. In this chapter, we extended this approach to a large *closo*-type anion $B_{12}H_{12}^{2-}$. It is noted that the complete removal of diglyme from solution-synthesized $Li_2B_{12}H_{12}$ is challenging due to the strong coordination between Li^+ and ether molecules. Therefore, $Na_2B_{12}H_{12}$ was selected as a model system. Zeolites offer several advantages as an oxide scaffold: high specific surface area, tunable acidity, structural rigidity, and well-defined pore architectures. These features collectively allow dense hydride–oxide interfacial contact without inducing chemical degradation, providing ideal conditions to probe interface-assisted Na^+ transport.

In this work, we investigate zeolite-$Na_2B_{12}H_{12}$ composites prepared via mechanochemical synthesis using zeolites CVB720 and CVB760, with different SiO_2/Al_2O_3 ratios and surface areas. Notably, the zeolite-$Na_2B_{12}H_{12}$ composite achieved a conductivity of 2.04×10^{-5} S cm^{-1} at room temperature and ~10^{-3} S cm^{-1} at 90 °C. Besides, it exhibits excellent electrochemical stability (>3.94 V) and stable Na plating/stripping over extended cycling at 80 °C. Combining structural, spectroscopic, surface, and electrochemical analyses, we reveal a unified mechanism of interface-induced activation that governs fast-ion

conduction in *closo*-type hydride-oxide composites. This study reveals a simple route to activate fast Na^+ transport in *closo*-type hydrides, providing new insights for the design of high-performance and cost-effective solid-state sodium electrolytes.

4.2 Results and discussions

Table 4.1 Sample of composites.

Sample	Zeolite type	Zeolite: $Na_2B_{12}H_{12}$ (Mass Ratio)
760-$Na_2B_{12}H_{12}$(1:1)	760	1:1
760-$Na_2B_{12}H_{12}$(1:2)	760	1:2
720-$Na_2B_{12}H_{12}$(1:1)	720	1:1
760-$Na_2B_{12}H_{12}$(1:2)	720	1:2

$Na_2B_{12}H_{12}$ material was prepared by the reaction of $NaBH_4$ and DMS BH_3 in diglyme solvent at 160 ℃, following the previous reported procedures (**Fig. 4.1(a)**). Solid-state ^{11}B NMR was conducted to verify the boron species in $Na_2B_{12}H_{12}$. The main double peak at ~15 ppm is attributed to $B_{12}H_{12}^{2-}$ (**Fig. 4.2(b)**), which was consistent with previous literature[22,23]. These results demonstrate the successful synthesis of phase-pure $Na_2B_{12}H_{12}$.

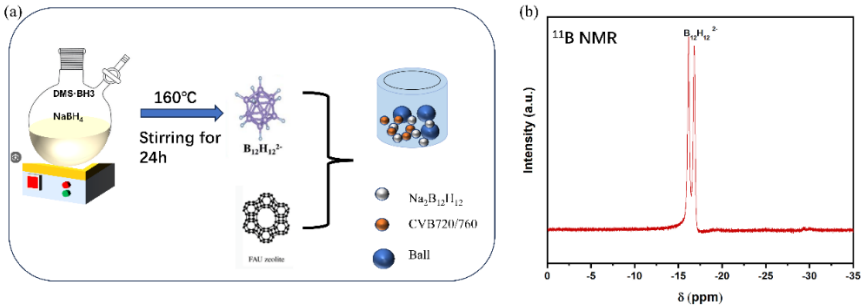

Fig. 4.1(a) Schematic illustration of the synthesis of $Na_2B_{12}H_{12}$ and zeolite- $Na_2B_{12}H_{12}$ composites; **(b)** ^{11}B NMR spectra of $Na_2B_{12}H_{12}$.

The composition of zeolite-$Na_2B_{12}H_{12}$ composites was further examined by FTIR spectroscopy and PXRD pattern (**Fig. 4.2**). The FTIR spectra (**Fig. 4.2 (a)**) of both pristine $Na_2B_{12}H_{12}$ and its zeolite composites display the typical B-H stretching vibration bands, and B-H bending modes of $Na_2B_{12}H_{12}$ are located at 2403 and 700 cm^{-1}, 1074 cm^{-1} is the vibration of a B-B bond that belongs to the boron cage[23]. No new absorption bands are observed upon compositing with zeolite, indicating that during the mechanochemical ball-milling synthesis of the composite samples, the structure of the $B_{12}H_{12}^{2-}$ anion remained unchanged. Peaks at 1300 and 500 cm^{-1} identify the presence of zeolite 720 and 760. Compared to CVB720, CVB760, and pure $Na_2B_{12}H_{12}$. Importantly, no B-O vibration band is detected between 900-1100 cm^{-1}, indicating that no interfacial reaction or oxidation occurred between $Na_2B_{12}H_{12}$ and the zeolite framework. This behavior differs sharply from the previously reported $NaBH_4$-MCM-41 composite prepared by a melt-infiltration process, in which molten $NaBH_4$ readily reacts with

the siliceous surface[24].

The XRD pattern of zeolite-$Na_2B_{12}H_{12}$ composites is shown in **Fig. 4.2(b)**, with the diffraction peaks of zeolites and a strong peak at 2θ = 6.96°, which is related to $Na_2B_{12}H_{12}$. These results mean that zeolite introduction does not change the boron-hydride $[B_{12}H_{12}]^{2-}$ framework during ball-milling. Instead, it introduces physical mixing and interfacial contact without inducing chemical reactions or new crystalline phases. This demonstrates that the mechanochemical process primarily modifies the microstructure and interfacial environment rather than affecting the intrinsic anion framework. The following section explores how such structural modification affects ionic conductivity.

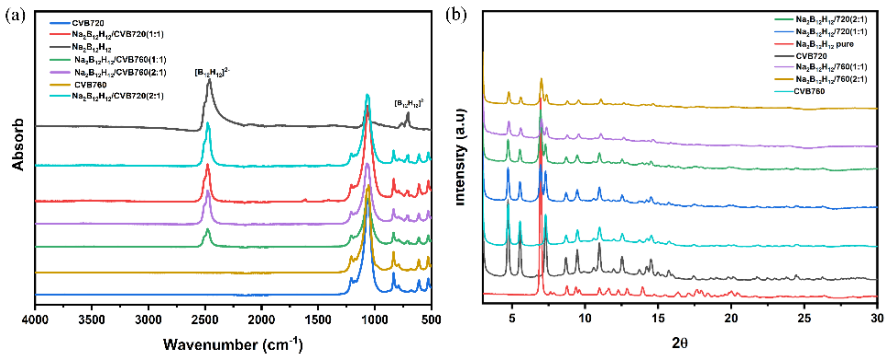

Fig. 4.2 (a) FTIR spectroscopy of zeolite- $Na_2B_{12}H_{12}$ and pure $Na_2B_{12}H_{12}$. **(b)** XRD pattern.

Ionic conductivity of zeolite-$Na_2B_{12}H_{12}$

The ionic conductivities of pristine $Na_2B_{12}H_{12}$ and the zeolite-

$Na_2B_{12}H_{12}$ composites were first evaluated by EIS in the temperature range of 25-90 °C. As shown in **Fig. S4.1** and **Fig. 4.3,** the impedance data of pure $Na_2B_{12}H_{12}$ consists of a semicircle in a high frequency region at 40 °C, indicating that the resistance value is over 500 kΩ. When the temperature increased to 80 ℃, the value of resistance was still 19 kΩ, indicating poor ionic transport. In contrast, the diameters of semicircles in the EIS spectra of zeolite- $Na_2B_{12}H_{12}$ composites are much smaller than that of pure $Na_2B_{12}H_{12}$. At 80 ℃, 720-$Na_2B_{12}H_{12}$(1:2) resistance is only 180 Ω, demonstrating that zeolite incorporation greatly enhances ionic mobility.

The temperature-dependent ionic conductivities of pure $Na_2B_{12}H_{12}$ and zeolite- $Na_2B_{12}H_{12}$ composites were summarized in **Fig. 4.4(a)** and **Table S4.1**. At room temperature, pure $Na_2B_{12}H_{12}$ displayed a significantly lower ionic conductivity of 9.07×10^{-8} S cm^{-1} at 40℃, whereas all zeolite- $Na_2B_{12}H_{12}$ composites showed an enhanced ionic conductivity compared to pure $Na_2B_{12}H_{12}$. Among them, 720-$Na_2B_{12}H_{12}$(1:2) shows the best performance, achieving the ionic conductivity of 2.04×10^{-5} S cm^{-1} at the ambient temperature, which is nearly three orders of magnitude over pure $Na_2B_{12}H_{12}$ and the conductivity up to 1.29×10^{-3} S cm^{-1} at 90 ℃. In contrast, the conductivity of $NaBH_4$-MCM41 composite[20] is only 10 times higher than that of $NaBH_4$. Other zeolite-$Na_2B_{12}H_{12}$ composites also show significant improvements; the 760-$Na_2B_{12}H_{12}$ (1:2) sample reaches 1.03 $\times$ 10^{-5} S cm^{-1} at room temperature and 7.33 $\times$ 10^{-4} S cm^{-1} at 90 °C,

while the 720-$Na_2B_{12}H_{12}$ (1:1) composite exhibits a conductivity of 5.15×10^{-6} S cm^{-1} at room temperature and 4.14×10^{-5} S cm^{-1} at 90 °C. The 760-based 1:1 composite shows slightly lower conductivity among all composites. This similar tendency was observed in the zeolite-$LiBH_4$ system in **Chapter 3**, where 720-based composites outperformed those using 760. This correlation highlights the key role of the zeolite's surface area: the higher specific surface area of zeolite 720 provides more active interfaces and continuous Na^+ transport pathways, thus facilitating interfacial ion migration and enhancing overall conductivity.

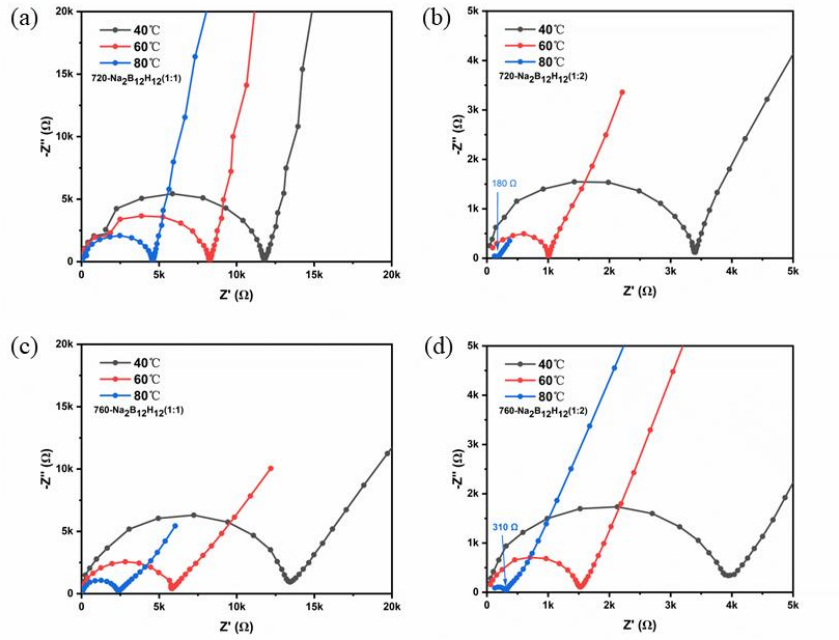

Fig. 4.3 EIS plots of zeolite- $Na_2B_{12}H_{12}$ composites

The activation energies for Na^+ conduction were calculated from the

Arrhenius plots and are shown in **Fig. 4.4 (b)**. The pure $Na_2B_{12}H_{12}$ shows the highest activation energy (*Ea*) of 0.75 eV, consistent with its poor conductivity. In comparison, the zeolite-$Na_2B_{12}H_{12}$ composites exhibit significantly lower *Ea* values: 0.35 eV for 720-$Na_2B_{12}H_{12}$ (1:1), 0.41 eV for 760-$Na_2B_{12}H_{12}$ (1:1), 0.58 eV for 760-$Na_2B_{12}H_{12}$ (1:2), and 0.60 eV for 720-$Na_2B_{12}H_{12}$ (1:2). Interestingly, although the 720(1:2) sample has a slightly higher activation energy than that of its 1:1, it still displays the highest conductivity over the entire temperatures range. This behavior indicates that Na^+ transport in the composite is no longer governed only by bulk migration barriers. Instead, the dominant contribution arises from a percolating interfacial transport network formed between $Na_2B_{12}H_{12}$ and the high-surface-area zeolite scaffold. Therefore, owing to its superior ionic conductivity and favorable activation energy, the 720-$Na_2B_{12}H_{12}$ composite with a 1:2 mass ratio was selected for subsequent electrochemical measurements, as it provides an optimal balance between ionic transport efficiency and energy barrier, thereby motivating further investigation of its interfacial conduction mechanism.

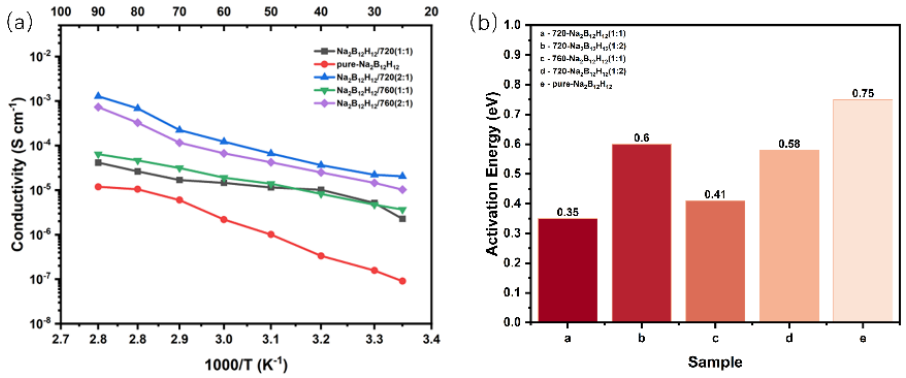

Fig. 4.4 (a) Temperature-independent conductivity of pure $Na_2B_{12}H_{12}$ and zeolite-$Na_2B_{12}H_{12}$ composites. **(b)** *Ea* value of pure $Na_2B_{12}H_{12}$ and zeolite-$Na_2B_{12}H_{12}$ composites.

The surface chemical composition was performed using X-ray photoelectron spectroscopy (XPS) on 720-$Na_2B_{12}H_{12}$ (1:2) composite. The high-resolution B 1s spectrum (**Fig. S4.2**) exhibits a single peak centered at ≈ 187.7 eV, corresponding to the $B_{12}H_{12}^{2-}$ anion. It is unlike the reported $Li_2B_{12}H_{12}$-Al_2O_3, which showed a B-O bond due to the interaction between $Li_2B_{12}H_{12}$ and Al_2O_3[21]. No additional features are detected at higher binding energy in the 720-$Na_2B_{12}H_{12}$ (1:2) composite. This shows that no oxidation or chemical reaction occurs between -$Na_2B_{12}H_{12}$ and the zeolite surface during the composite formation process. Collectively, it reveals the chemical stability between $Na_2B_{12}H_{12}$ and zeolite, thereby excluding the formation of any intermediate phases at the interface that could account for the enhanced Na^+ conductivity in the composites.

To further verify the interfacial effect responsible for the improved

ionic conductivity. Brunauer-Emmett-Teller (BET) analysis was conducted for the 720-$Na_2B_{12}H_{12}$ (1:2) composite in **Fig. 4.5**. The specific surface area of the pristine zeolite 720 was measured in **Chapter 3** to be 804 m^2 g^{-1}, while that of the composite decreased markedly to 10.17 m^2 g^{-1}. The reduction in surface area indicates that particles have fully covered the zeolite surface, forming continuous interfacial contact. In reactive systems such as $NaBH_4$-MCM-41, similar coverage would aggravate interfacial oxidation. However, in the chemically stable zeolite-$Na_2B_{12}H_{12}$ system, increased interfacial area directly translates into more continuous and energetically favorable Na^+ migration pathways. The BET results thus confirm the physical infiltration model proposed by XPS and conductivity data, showing that dense interfacial layers are the structural origin of enhanced Na^+ conduction.

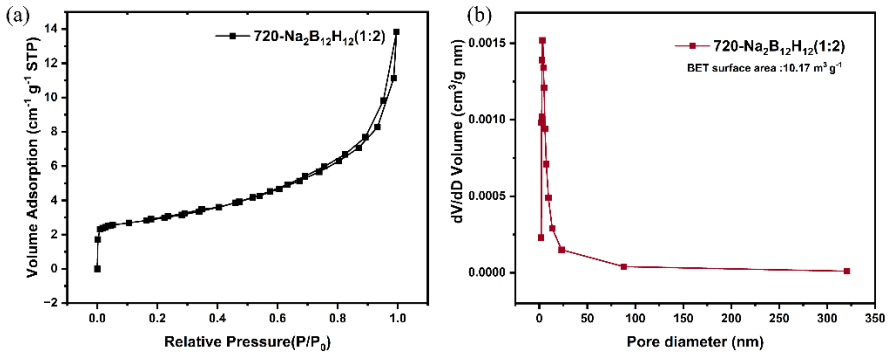

Fig. 4.5 (a) Nitrogen physisorption isotherms for 720-$Na_2B_{12}H_{12}$ (1:2); **(b)** pore-size distribution plots for 720-$Na_2B_{12}H_{12}$ (1:2)

In addition to conductivity, both electrochemical stability and electronic insulation properties also need to be considered for promising electrolytes in Na-based batteries. The electrochemical potential window of 720-$Na_2B_{12}H_{12}$(1:2) and pure $Na_2B_{12}H_{12}$ were examined by Linear sweep voltammetry (LSV) **(Fig. 4.6(a))**. Measurements were conducted using a Na|720-$Na_2B_{12}H_{12}$(1:2) |SS coin cell, at a scanning rate of 0.1 mV s^{-1} and over a voltage range from open-circuit voltage (OCV) to 4.0 V at 80 ℃. The LSV curve shows that the current remains negligible up to 3.94 V (*vs* Na^+/Na), indicating 720-$Na_2B_{12}H_{12}$(1:2) shows a broad electrochemical stability window and excellent oxidative stability. This value is slightly higher than that of $Na_2B_{12}H_{12}$ (3.85 V) and $NaB_{11}H_{14}$ (2.6 V)[25]. Even though $Na_3NH_2B_{12}H_{12}$ has been reported to have a wide electrochemical window of 0-10 V,[13] its actual stability range may be smaller, as that value was not determined through oxidation measurements starting from OCP. This suggests that 720-$Na_2B_{12}H_{12}$(1:2) composite is suitable for employing a high-voltage cathode in sodium-based batteries. The electronic conductivity (σ_e) of the sample 720-$Na_2B_{12}H_{12}$(1:2) at 80 ℃ was determined to be 1.15 × 10^{-6} S cm^{-1} based on DC polarization measurements (**Fig. 4.6(b)**), which is approximately 3 orders of magnitude lower than σ (Na^+). Therefore, the 720-$Na_2B_{12}H_{12}$(1:2) composite is an ion conductor, and the electron conductivity is negligible, which will effectively suppress the growth of dendrites.

To further evaluate the structural stability of the composite

electrolyte, in-situ XRD was carried out on the 720- $Na_2B_{12}H_{12}$ (1:2) sample from 20 °C to 100 °C (**Fig. S4.3**). The diffraction patterns exhibit no noticeable change in peak position, intensity, or width across the entire temperature range. The main reflections of $Na_2B_{12}H_{12}$ remain constant, and no new peaks corresponding to decomposition or phase transformation are detected. This result indicates that both the $[B_{12}H_{12}]^{2-}$ framework and the composite structure are thermally stable below 100 °C.

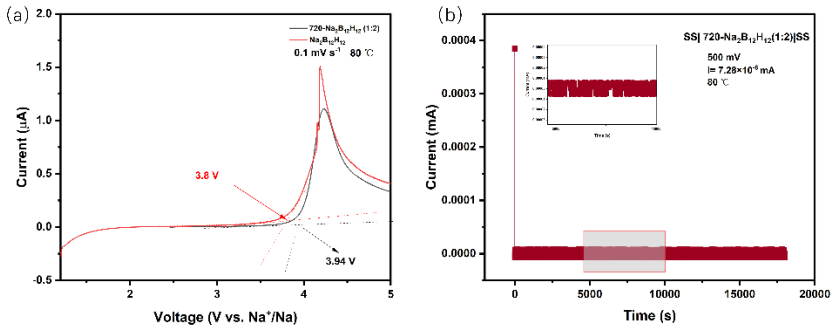

Fig. 4.6 (a) LSV curve of pure $Na_2B_{12}H_{12}$ and 720-$Na_2B_{12}H_{12}$(1:2) composite. **(b)** DC curve of 720- $Na_2B_{12}H_{12}$(1:2).

The Na dendrite suppression capability of 720-$Na_2B_{12}H_{12}$(1:2) was evaluated using the galvanostatic cycling (GC) test of a Na|720-$Na_2B_{12}H_{12}$(1:2) |Na symmetric cell at 80 °C with a current density of 0.1 mA $cm^{-2,}$ with 1 hour plating/stripping intervals as shown in **Fig. 4.7(a)**. The cell exhibits fully reversible sodium plating and stripping with a stable overpotential of approximately 125 mV. Remarkably, the

voltage remains nearly constant at 125 mV over 60 hours of continuous cycling without any noticeable increase or short-circuiting. This excellent stability demonstrates the good interfacial compatibility between the composite electrolyte and the sodium metal anode, as well as the ability of 720-$Na_2B_{12}H_{12}$(1:2) to effectively suppress sodium dendrite growth during cycling. To further evaluate the interfacial stability of the composite electrolyte, electrochemical impedance spectroscopy (EIS) was performed on the Na|720- $Na_2B_{12}H_{12}$(1:2) |Na symmetric cell before and after galvanostatic cycling (**Fig. 4.7**). The Nyquist plots exhibit a single semicircle in the high-frequency region, corresponding to the combined bulk and interfacial resistance of the cell. Before cycling, the total resistance was approximately 900 Ω, which only slightly increased to 930 Ω after 60 hours of continuous Na plating/stripping at 80 °C. This negligible change displays that the composite electrolyte maintains intimate interfacial contact with the sodium metal anode, without significant formation of interphase or side reactions during cycling. Together with the stable overpotential of ~125 mV observed in the galvanostatic test, these results demonstrate the excellent chemical and electrochemical compatibility of the 720-$Na_2B_{12}H_{12}$(1:2) composite with sodium metal, as well as its stability under cycling. Thus, the composite exhibits both high ionic conductivity and outstanding interfacial stability, fulfilling the essential requirements for solid-state sodium batteries.

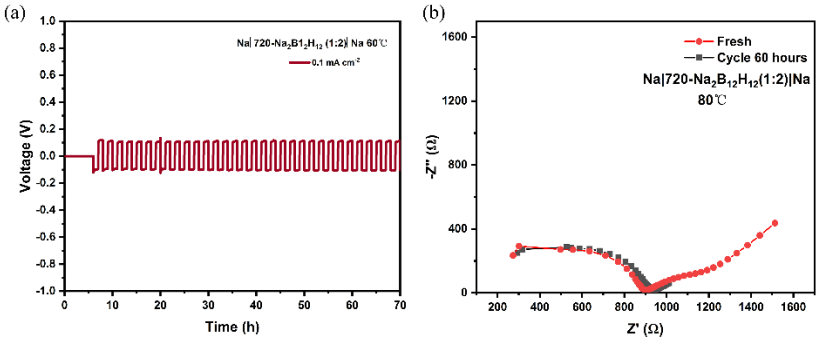

Fig. 4.7 (a) Galvanostatic Na plating/stripping profiles of the Na|720-$Na_2B_{12}H_{12}$(1:2) |Na cell at 80 °C. **(b)** EIS curve of Na|720-$Na_2B_{12}H_{12}$(1:2) |Na before and after cycling for 60 hours.

4.3 Conclusion

In summary, a series of zeolite-$Na_2B_{12}H_{12}$ composites was successfully synthesized and systematically investigated as potential solid-state electrolytes for sodium batteries. Structural analyses evidence that no chemical reaction or phase transformation occurred between $Na_2B_{12}H_{12}$ and zeolite during the mechanochemical process. Instead, the incorporation of zeolite markedly enhanced Na^+ transport through interfacial effects. Among the prepared samples, the 720-$Na_2B_{12}H_{12}$ (1:2) composite exhibited the highest ionic conductivity of 1.29×10^{-3} S cm^{-1} at 90 °C, which is about three orders of magnitude higher than that of pure $Na_2B_{12}H_{12}$, and a reduced activation energy of 0.60 eV. The improvement in ionic conductivity is mainly attributed to the enlarged interfacial area and continuous Na^+ migration pathways provided by the high specific surface area and three-dimensional porous architecture of zeolite 720.

Electrochemical measurements further verified the excellent stability and interfacial compatibility of the composite electrolyte. The 720-$Na_2B_{12}H_{12}$(1:2) sample showed a wide electrochemical window of 3.94 V (*vs.* Na^+/Na) and a low electronic conductivity of approximately 10^{-6} S cm^{-1}. In the Na|SSEs|Na symmetric cell, stable and reversible sodium plating/stripping was achieved at 80 °C with an overpotential of about 125 mV, which remained constant over 60 hours of cycling without short-circuiting. This behavior indicates good interfacial contact between the composite electrolyte and the sodium metal anode and suggests effective suppression of interfacial instability under the tested conditions.

Overall, this study reveals that the introduction of zeolite is not only beneficial for $LiBH_4$-based systems but is also highly effective for $Na_2B_{12}H_{12}$ and other *closo*-type complex hydrides. The zeolite incorporation strategy offers a promising route to enhance both Na^+ conductivity and interfacial stability, providing valuable insights for the design of cost-effective and high-performance solid electrolytes for next-generation sodium-based solid-state batteries.

4.4 Experiment section

Synthesis

The synthesis procedure to obtain preparation of $Na_2B_{12}H_{12}$ is

adapted from Wang et al[22]. It should be noted that this process requires utmost caution for safety. Commercial $NaBH_4$ (95%, Alfa Aesar) powder was directly used without further purification. 0.38 g of $NaBH_4$ was dissolved in 20 mL anhydrous diglyme in a 100mL Schlenk flask. Then, 5.4 mL borane dimethyl sulfide complex ($DMS{\cdot}BH_3$) was added dropwise to the solution, which was attached to a Schlenk line. After stirring for 24 hours at 160 ℃, the mixture was dried at 200℃ for 24 hours and cooled down to room temperature. And then it should be washed by diglyme (3 × 5mL) and filtered. The solid product was finally vacuum dried at 80 ℃ for 12 hours to remove the diglyme residue. The final white product was transferred into an argon-filled glove box.

Zeolite Y type (from Zeolyst): CVB720 (SiO_2/Al_2O_3 mole ratio: 30) and CVB760 (SiO_2/Al_2O_3 mole ratio: 60). Zeolite was dried under dynamic vacuum at 250℃ for 12 hours prior to use. Zeolite- $Na_2B_{12}H_{12}$ composites were synthesized by Ball-milling:720-$Na_2B_{12}H_{12}$ and 760-$Na_2B_{12}H_{12}$ were prepared with different kinds of mass ratios of 1:1 and 1:2. For each experiment, 0.8 g of the mixture was loaded into a stainless-steel milling jar in a glove box filled with argon. The ball-to-sample weight ratio was kept at 13:1. Two compositions of $Na_2B_{12}H_{12}$ and 720, 760 were mechanically milled at 400 rpm for 4h with a planetary ball mill (XQM-0.4A, Changsha). All samples prepared were milled for 3 min, and 2 min breaks were taken to overcome heating effects. All manipulations of the samples during the experiment were

conducted within an Argon atmosphere in a glove box ($p(O_2) < 0.1$ ppm, $p(H_2O) < 0.1$ ppm)

XRD patterns were collected by an MAR345 image plate detector with Mo Ka radiation ($\lambda = 0.71072$ Å). NMR spectra were measured on Bruker Avance 500 spectrometer at 160.46 MHz for ^{11}B. FTIR spectra were recorded by the attenuated total reflectance (ATR) on Bruker a II spectrometer in an argon-filled glovebox. The X-ray photoelectron spectroscopy (XPS) measurements were performed on ESCALAB 250Xi, and the sample was prepared in an Ar-filled glovebox. After well sealing, the sample stage is transferred to the chamber to avoid contact with air as much as possible.

Sodium ionic conductivities were measured with electrochemical impedance spectroscopy (EIS) in a frequency range from 7 MHz to 100 mHz by pressing samples into a solid pellet with a diameter of 0.6-1.0 mm in a sandwich structure of two stainless steels. The conductivity was calculated by the following equation:

$$\sigma = \frac{L}{RS} \qquad (1)$$

Where R represents the resistance of EIS, S represents contact area of SSE, and L is the thickness of the SSE (0.6~0.9 mm). The activation energy can be calculated by the Arrhenius equation:

$$\ln \sigma T = \frac{E_a}{K_B T} + C \qquad (2)$$

Linear sweep voltammetry (LSV) measurements were conducted on an electrochemical workstation (EC Lab) with a scanning rate of 0.1 mV S^{-1} and a voltage range from open circuit potential to 5.0 V. The composite samples were pressed into a pellet under 600 MPa, then sandwiched by Na metal foil and stainless steel into a CR2032 coin cell.

The DC polarization was measured by two pieces of stainless steels (SS) electrodes with a constant voltage of 0.5 V for 13,000 s. The electronic conductivity can be calculated by following equation:

$$R = \frac{V}{I} \qquad (3)$$

Cell assembly

Symmetric Na|zeolite-$Na_2B_{12}H_{12}$|Na cell was evaluated by galvanostatic discharge/charge measurements using EC-LAB at 80 °C with a current density of 0.1 mA cm^{-2}.

4.5 Support information

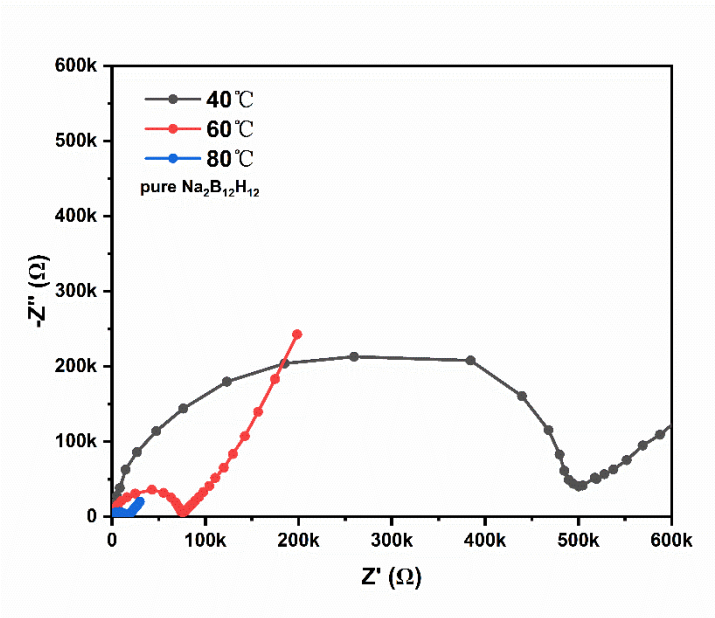

Fig S4.1 EIS plots of pure $Na_2B_{12}H_{12}$ at 40 ℃, 60 ℃, and 80 ℃.

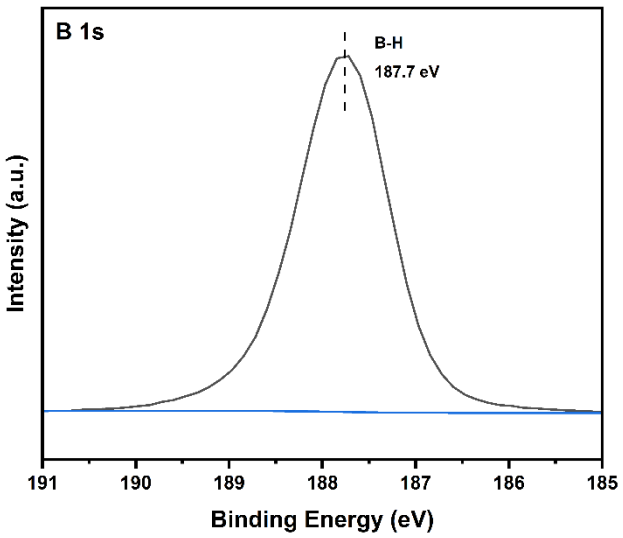

Fig. S4.2 B1s XPS spectra of 720-$Na_2B_{12}H_{12}$ (1:2) composite.

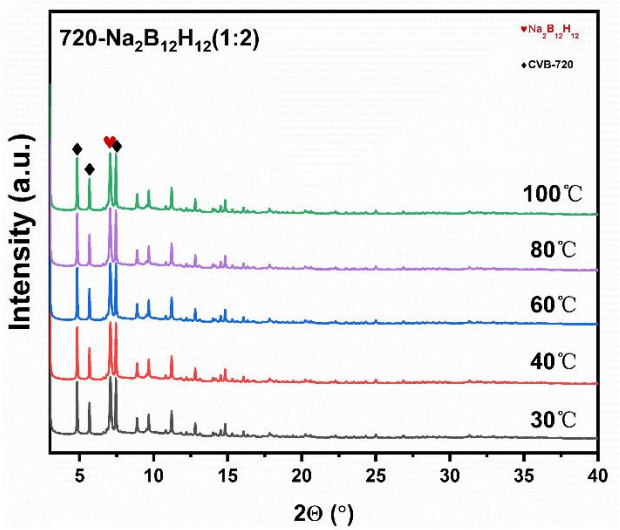

Fig. S4.3 Synchrotron *In-situ* XRD of 720- $Na_2B_{12}H_{12}$(1:2) from 30-100℃.

Table S4.2. Ionic conductivities of samples at different temperatures.

Sample	720-$Na_2B_{12}H_{12}$(1:1)	720-$Na_2B_{12}H_{12}$(1:2)	760-$Na_2B_{12}H_{12}$(1:1)	760-$Na_2B_{12}H_{12}$(1:2)	$Na_2B_{12}H_{12}$
$\sigma_{25℃}$ ($S\ cm^{-1}$)	2.27×10^{-6}	2.04×10^{-5}	3.65×10^{-6}	1.02×10^{-5}	9.07×10^{-8}
$\sigma_{30℃}$ ($S\ cm^{-1}$)	5.15×10^{-6}	2.21×10^{-5}	4.72×10^{-6}	1.46×10^{-5}	1.57×10^{-7}
$\sigma_{40℃}$ ($S\ cm^{-1}$)	1.02×10^{-5}	3.63×10^{-5}	8.22×10^{-6}	2.51×10^{-5}	3.35×10^{-7}
$\sigma_{50℃}$ ($S\ cm^{-1}$)	1.15×10^{-5}	6.62×10^{-5}	1.40×10^{-6}	4.21×10^{-5}	1.01×10^{-6}
$\sigma_{60℃}$ ($S\ cm^{-1}$)	1.46×10^{-5}	1.23×10^{-4}	1.90×10^{-6}	6.69×10^{-5}	2.19×10^{-6}
$\sigma_{70℃}$ ($S\ cm^{-1}$)	1.69×10^{-5}	2.24×10^{-4}	3.12×10^{-6}	1.16×10^{-4}	6.00×10^{-6}
$\sigma_{80℃}$ ($S\ cm^{-1}$)	2.63×10^{-5}	6.86×10^{-4}	4.63×10^{-6}	3.26×10^{-4}	1.05×10^{-5}
$\sigma_{90℃}$ ($S\ cm^{-1}$)	4.14×10^{-5}	1.29×10^{-3}	6.39×10^{-55}	7.33×10^{-4}	1.19×10^{-5}

4.6 References

1. Palomares, V. *et al.* Na-ion batteries, recent advances and present challenges to become low cost energy storage systems. *Energy Environ. Sci.* 5, 5884–5901 (2012).

2. Anantharamulu, N. *et al.* A wide-ranging review on Nasicon type materials. *J. Mater. Sci.* 46, 2821–2837 (2011).

3. Nakajima, H. *et al.* Crystallization behaviors in superionic conductor Na3PS4. *J. Power Sources* 511, 230444 (2021).

4. Gupta, M. K. *et al.* Investigation of Low-Energy Lattice Dynamics and Their Role in Superionic Na Diffusion and Ultralow Thermal Conductivity of Na_3PSe_4 as a Solid-State Electrolyte. *Chem. Mater.* 36, 11377–11392 (2024).

5. Udovic, T. J. *et al.* Sodium superionic conduction in $Na_2B_{12}H_{12}$. *Chem Commun* 50, 3750–3752 (2014).

6. Hansen, B. R. S., Paskevicius, M., Li, H.-W., Akiba, E. & Jensen, T. R. Metal boranes: Progress and applications. *Coord. Chem. Rev.* 323, 60–70 (2016).

7. Zhou, C., Yan, Y. & Jensen, T. R. Enhanced Electrochemical Performance of the $Li_2B_{12}H_{12}$-$Li_2B_{10}H_{10}$-$LiBH_4$ Electrolyte. *ACS Appl. Energy Mater.* 6, 7346–7352 (2023).

8. Su, Z. *et al.* A Novel Oxidized $Na_2B_{12}H_{12}$–Based Electrolyte for High-Voltage All-Solid-State Sodium Batteries. *ACS Appl. Energy Mater.* 8, 5656–5663 (2025).

9. Teprovich, J. A. *et al.* Bi-functional $Li_2B_{12}H_{12}$ for energy storage and conversion applications: solid-state electrolyte and luminescent down-conversion dye. *J. Mater. Chem. A* 3, 22853–22859 (2015).

10. Jin, M. *et al.* A Practical Nonflammable $Na_4B_{36}H_{34}$-Based Hydroborate Electrolyte for High-Voltage All-Solid-State Sodium Batteries. *ACS Energy Lett.* 9, 1176–1183 (2024).

11. Udovic, T. J. *et al.* Sodium superionic conduction in $Na_2B_{12}H_{12}$. *Chem. Commun.* 50, 3750–3752 (2014).

12. Tang, W. S. *et al.* Stabilizing lithium and sodium fast-ion conduction in solid polyhedral-borate salts at device-relevant temperatures. *Energy Storage Mater.* 4, 79–83 (2016).

13. He, L. *et al.* $Na_3NH_2B_{12}H_{12}$ as high performance solid electrolyte for all-solid-state Na-ion batteries. *J. Power Sources* 396, 574–579 (2018).

14. Sadikin, Y., Brighi, M., Schouwink, P. & Černý, R. Superionic Conduction of Sodium and Lithium in Anion-Mixed Hydroborates $Na_3BH_4B_{12}H_{12}$ and $(Li_{0.7}Na_{0.3})_3BH_4B_{12}H_{12}$. *Adv. Energy Mater.* 5, (2015).

15. Sadikin, Y., Schouwink, P., Brighi, M., Łodziana, Z. & Černý, R. Modified Anion Packing of $Na_2B_{12}H_{12}$ in Close to Room Temperature Superionic Conductors. *Inorg. Chem.* 56, 5006–5016 (2017).

16. Gulino, V., de Kort, L., Ngene, P., de Jongh, P. & Baricco, M. Combined Effect of Halogenation and SiO_2 Addition on the Li-Ion Conductivity of LiBH4. *Inorganics* 11, 459 (2023).

17. Mizuochi, H. *et al.* Effects of Oxide Morphology on Lithium-Ion Conductivity of $LiBH_4$–Al_2O_3 Composites. *ACS Appl. Energy Mater.* 8, 518–528 (2025).

18. Blanchard, D. *et al.* Nanoconfined $LiBH_4$ as a Fast Lithium Ion Conductor. *Adv. Funct. Mater.* 25, 184–192 (2015).

19. Gulino, V. *et al.* Room-Temperature Solid-State Lithium-Ion Battery Using a $LiBH_4$–MgO Composite Electrolyte. *ACS Appl. Energy Mater.* 4, 1228–1236 (2021).

20. Luo, X., Rawal, A. & Aguey-Zinsou, K.-F. Investigating the Factors Affecting the Ionic Conduction in Nanoconfined $NaBH_4$. *Inorganics* 9, 2 (2021).

21. Zhou, C. *et al.* Highly electrochemically stable $Li_2B_{12}H_{12}$-Al_2O_3 nanocomposite electrolyte enabling a 3.8 V room-temperature all-solid-state Li-ion battery. *J. Alloys Compd.* 938, 168689 (2023).

22. Wang, J., Steenhaut, T., Li, H.-W. & Filinchuk, Y. High Yield Autoclave Synthesis of pure $M_2B_{12}H_{12}$ (M = Na, K). *Inorg. Chem.* 62, 2153–2160 (2023).

23. Pylypko, S. *et al.* The highly stable aqueous solution of sodium dodecahydro- closo -dodecaborate $Na_2B_{12}H_{12}$ as a potential liquid anodic fuel. *Appl. Catal. B Environ.* 222, 1–8 (2018).

24. Luo, X., Rawal, A. & Aguey-Zinsou, K.-F. Investigating the Factors Affecting the Ionic Conduction in Nanoconfined $NaBH_4$. *Inorganics* 9, 2 (2021).

25. Payandeh, S. *et al.* Nido-Borate/Closo-Borate Mixed-Anion Electrolytes for All-Solid-State Batteries. *Chem. Mater.* 32, 1101–1110 (2020).

Chapter 5 Enhancing Ionic Transport and Li-Metal Compatibility in $LiBH_4$-$2LiNH_2$ via BN Interfacial Engineering

Abstract

Adding a small amount of BN significantly increases the ion conductivity of the $LiBH_4$-$2LiNH_2$ system owing to the formation of the highly conductive interface between the two phases. The $LiBH_4$-$2LiNH_2$-10%BN achieves an ionic conductivity as high as 1.17×10^{-3} S cm^{-1} at 35 °C. Remarkably, symmetric Li|$LiBH_4$-$2LiNH_2$-10%BN|Li cells exhibit long-term plating/stripping stability for >200 h at room temperature and >180 h at 50 °C with low polarization, successfully obviating the need for Li-In alloy anodes. Moreover, the practical feasibility of the electrolyte is validated in a solid-state Li|$LiBH_4$-$2LiNH_2$-10%BN|$Li_4Ti_5O_{12}$ full cell, which delivers reversible charge-discharge capability.

These results demonstrate that BN-based interfacial engineering enables fast Li^+ conduction and robust Li-metal compatibility, offering a practical and scalable route to high-performance hydride solid-state electrolytes.

5.1 Introduction

With the growing demand for electric vehicles and large-scale energy storage systems, the development of batteries with higher energy density and improved safety has become one of the major areas of research[1,2]. However, conventional liquid organic electrolytes present potential safety risks[3,4]. All-solid-state batteries (ASSBs), employing

solid-state electrolytes (SSEs), offer significant advantages in safety, thermal stability, and potential energy density[5,6], and have been regarded as promising candidates for new battery systems.

Among various SSEs, $LiBH_4$-based hydrides have attracted considerable attention due to their excellent chemical compatibility with lithium metal, outstanding mechanical strength, and high Li^+ conductivity in the hexagonal phase (>10^{-3} S cm^{-1} at 393 K) [7]. At room temperature, however, $LiBH_4$ adopts an orthorhombic phase with a very low conductivity (~10^{-8} S cm^{-1})[8]. To address this issue, strategies such as anion substitution (I^-, Br^-, Cl^-)[8–11] and molecular complexation (NH_3 and CH_3NH_3)[12–14] have been proposed to enhance its room-temperature conductivity but often require complex or high-temperature processing.

The $LiBH_4$-$LiNH_2$ composites represent an important advance because the introduction of $[NH_2]^-$ anions increases lithium vacancies and lowers migration barriers, thereby improving Li-ion conductivity to ~10^{-4} S cm^{-1} near room temperature[15,16]. Nonetheless, $LiBH_4$-$LiNH_2$ SSEs still face two main challenges: (1) their room-temperature conductivity (~10^{-4} S cm^{-1}) remains below the practical threshold (>10^{-3} S cm^{-1}); and (2) poor interfacial stability with lithium metal leads to rapid capacity decay. Prior interfacial-engineering approaches have attempted to address these issues. SiO_2 nanoscaffolds can improve the conductivity of $LiBH_4$-$LiNH_2$ via stabilization of a highly conductive phase[18] but involve high inactive-mass content and show no

demonstrated Li-metal compatibility. Similarly, introducing g-C_3N_4 into $LiBH_4$-$LiNH_2$ can construct continuous Li^+ transport networks, lower interfacial impedance, significantly increase room-temperature conductivity, and improve interfacial stability, achieving superior long-cycle performance[22], but stable long-term Li-metal cycling requires the use of Li-In alloy anodes.

Recently, two-dimensional (2D) materials have emerged as promising additives for hydride-based SSEs. BN, a layered 2D material with high thermal stability, a wide band gap, and excellent chemical inertness, has reduced grain-boundary resistance and facilitated Li^+ migration in $LiBH_4$, thereby enhancing conductivity[19]. MoS_2 has also been introduced in $LiBH_4$ and $Li_4(BH_4)_3I$ to achieve high conductivity at room temperature.[20,21] However, BN has not yet been applied to the $LiBH_4$-$LiNH_2$ system. Given its large specific surface area and chemical stability, BN is expected to further enhance ionic conductivity due to outstanding interfacial stability.

As shown in **Chapters 3** and **4**, interface engineering provides an effective baseline strategy for enhancing ion transport in borohydride-based solid-state electrolytes by forming interfacial regions for fast ion conduction. Although such methods can significantly increase conductivity without changing the borohydride lattice structure, the mechanical stability, interface integrity, and chemical robustness of the composite structure will further affect its performance. In this chapter,

we investigated $LiBH_4$-$2LiNH_2$-BN composite as an advanced interfacial model system, in which both anion chemistry and interfacial stabilization contribute to ionic transport. The $LiBH_4$-$2LiNH_2$ electrolyte containing 10 wt% BN (LBN-10%) achieves an ionic conductivity of 1.17×10^{-3} S cm^{-1} at 35 °C with a broad electrochemical window. It is worth noting that BN simultaneously enhances conductivity and dramatically improves Li-metal compatibility, enabling stable cycling with pure Li metal for >200 hours at room temperature, an achievement not previously reported for the $LiBH_4$-$LiNH_2$ system. Meanwhile, the practical applicability of this electrolyte is demonstrated through its compatibility with $Li_4Ti_5O_{12}$ in all solid-state batteries. This dual enhancement represents a significant step toward practical hydride-based SSEs.

5.2 Results and discussion

The XRD pattern of the as-prepared BN powder and the ball-milled BN is shown in **Fig. S5.1**. For the ball-milled BN, the broadening of the main peak after the mechanical process, and the disappearance of some diffraction peaks mean that BN has been refined. **Fig. 5.1(a)** compares the XRD patterns of three different BN contents of $LiBH_4$-$2LiNH_2$-BN composites and $LiBH_4$-$2LiNH_2$. The XRD pattern of $LiBH_4$-$2LiNH_2$ corresponds with the previous lecture. For the BN-added samples, the $LiBH_4$-$2LiNH_2$ still dominates the XRD peaks. When the content of BN is 5%, the diffraction peaks of BN in the pattern are almost invisible,

suggesting that the BN may form an amorphous phase after ball milling. Moreover, with the increasing content of BN, the peaks of BN become apparent. Nevertheless, the introduced BN does not affect the structure of $LiBH_4$-$2LiNH_2$. FT-IR spectra further illustrates whether BN affects the B-H bonds in the $LiBH_4$-$2LiNH_2$. The vibration bands of B-H (2200~2300 cm^{-1}) and B-N (1337 cm^{-1}) corresponding to $LiBH_4$-$2LiNH_2$ and BN are identified in **Fig. 5.1(b).** With the increasing content of BN, the B-N bonds in the $LiBH_4$-$2LiNH_2$-BN composite become sharper. **Fig. 5.1(c)-(d)** shows typical SEM images of $LiBH_4$-$2LiNH_2$-10%BN. The particle size after ball-milling was determined to be approximately 2-3 μm. In addition, some flat structures were observed around the particles, which were likely attributed to BN attached to the surface of $LiBH_4$-$2LiNH_2$ during the ball-milling process. These BN-electrolyte contacts are expected to play a central role in enhancing Li^+ transport by reducing grain-boundary resistance.

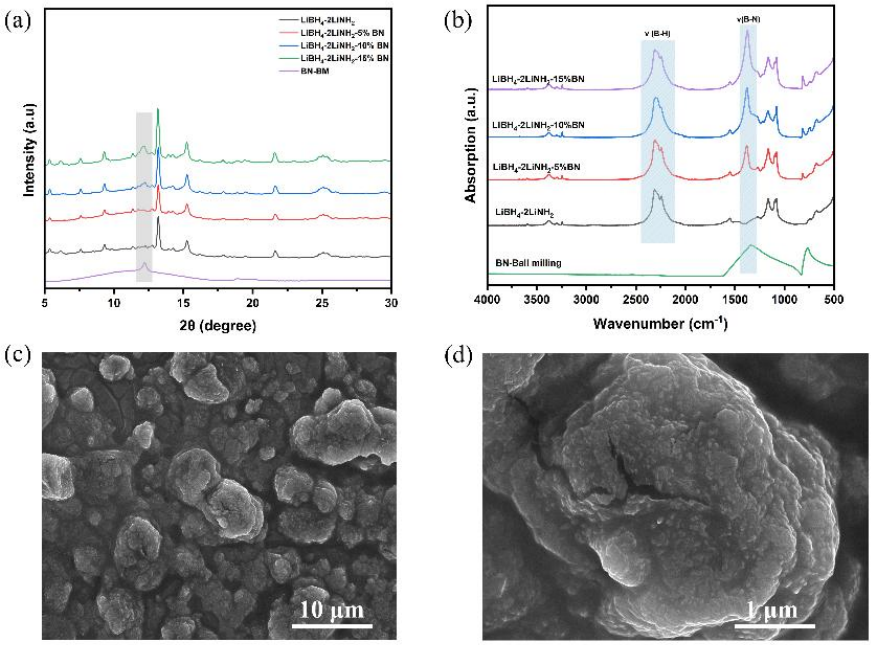

Fig. 5.1 (a) XRD patterns; **(b)** FTIR spectra of $LiBH_4$-$2LiNH_2$, BN-BM, and $LiBH_4$-$2LiNH_2$-x%BN materials; **(c)-(d)** SEM images of LiBH4-2LiNH2-10%BN materials.

Following the morphological analysis, X-ray Photoelectron Spectroscopy (XPS) was employed to definitively identify the chemical state of boron and demonstrate the distribution of BN at the interface. As shown in **Fig. 5.2**, the high-resolution B 1s spectrum of the $LiBH_4$-$2LiNH_2$-10%BN composite reveals three distinct chemical environments. The peak at 188.35 eV corresponds to the B-H bonds within the $LiBH_4$-$2LiNH_2$ matrix, while the prominent peak at 190.57 eV is characteristic of B-N bonds in h-BN. The minor peak at 192.02 eV is attributed to trace surface oxidation inevitable during sample

transfer[22]. Crucially, despite BN constituting only a fraction of the total mass, the B-N signal intensity is comparable to that of B-H. Given the surface-sensitive nature of XPS, this high B-N proportion serves as robust evidence that BN nanosheets are enriched at the surface of the electrolyte particles. This BN-rich interface is the key structural feature responsible for the enhanced transport properties discussed below.

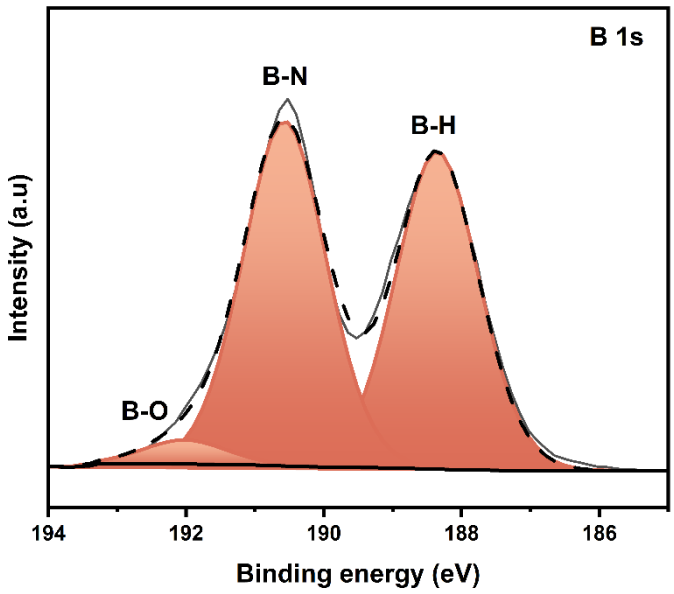

Fig. 5.2 B1s XPS spectra of $LiBH_4$-$2LiNH_2$-10%BN.

The ionic conductivity tests of composites were conducted by assembling symmetric stainless-steel cells with the solid-state electrolyte pellet thickness of 0.7-1.0mm. **Fig. 5.3(a)** shows EIS diagrams of Nyquist diagrams of $LiBH_4$-$2LiNH_2$, $LiBH_4$-$2LiNH_2$-x%BN composites, and $LiBH_4$-10% BN at 60 ℃. The typical Nyquist

plot of sample $LiBH_4$-$2LiNH_2$ and $LiBH_4$-10% at 60 °C consists of a semicircle in a high-frequency region and a linear tail in a low-frequency region. While $LiBH_4$-$2LiNH_2$-x%BN only exhibits a straight line intersecting the real axis, the absence of a semicircle suggests the fast Lithium-ion migration inside the bulk. The diameters of semicircles of $LiBH_4$-$2LiNH_2$, $LiBH_4$-$2LiNH_2$-5%BN, $LiBH_4$-$2LiNH_2$-10%BN, $LiBH_4$-$2LiNH_2$-15%BN composites, and $LiBH_4$-10% BN reveal the total resistance of 149.6 Ω, 60.5 Ω, 40 Ω, 42.5 Ω, and 2079 Ω, respectively. It is obviously found that LiBH4-$2LiNH_2$-x%BN has a smaller resistance than that of $LiBH_4$-$2LiNH_2$ and $LiBH_4$-10% BN. **Fig. 5.3(b)** shows the EIS results of $LiBH_4$-$2LiNH_2$-10%BN composite at various temperatures. The resistance gradually decreases with increasing temperature, demonstrating enhanced ionic conductivity at high temperature.

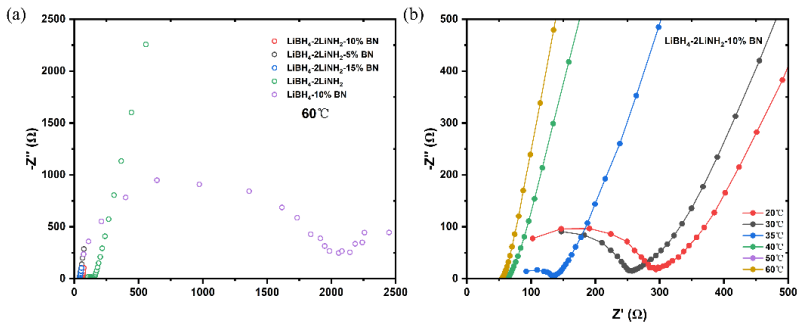

Fig. 5.3 (a) Electrochemical impedance spectroscopy (EIS) plots for $LiBH_4$-$2LiNH_2$, $LiBH_4$-$2LiNH_2$-x%BN composites, and $LiBH_4$-10% BN at 60 °C. **(b)** EIS plots for $LiBH_4$-$2LiNH_2$-10%BN at different temperatures.

The temperature-dependent (20-60 °C) ionic conductivity (**Fig. 5.4(a)**

and **Table 5.1)** shows that BN incorporation significantly enhances room-temperature Li^+ transport in the $LiBH_4$-$2LiNH_2$ system. Even with only 5% BN, the conductivity can reach 3.24×10^{-4} S cm^{-1} at 20 ℃. While it is only ~10^{-7} S cm^{-1} for pristine $LiBH_4$-$2LiNH_2$ under the same conditions. Increasing the BN content to 10 wt% further improves the ionic conductivity to 5.34×10^{-4} S cm^{-1}, representing an enhancement of approximately three orders of magnitude compared with the unmodified composite. For comparison, $LiBH_4$-10% BN exhibits ionic conductivity of 1.3 $\times10^{-6}$ S cm^{-1}, higher than pristine $LiBH_4$[23] and $LiBH_4$-$2LiNH_2$ but still far lower than that of $LiBH_4$-$2LiNH_2$-10%BN. Subsequently, when the mass content of BN exceeds 10 wt%, the conductivity begins to decrease, likely due to excessive BN interrupting continuous Li^+ percolation pathways. It is worth noting that previous studies have already demonstrated that BN incorporation enhances the ionic conductivity of $LiBH_4$[19], the interaction at the BN/hydride boundary induces lattice deformation and creates a conductive subsurface layer. This results in a percolation network where the insulating additive paradoxically acts as an enabler for fast ionic conduction. Our results not only corroborate this established interfacial-enhancement mechanism but also reveal an additional benefit: BN is even more effective in promoting Li^+ transport in the $LiBH_4$-$2LiNH_2$ system, where the presence of $[NH_2]^-$ facilitates vacancy formation. The BN further modifies these interfacial regions, enabling Li^+ to migrate more efficiently across particle boundaries and thereby lowering the

overall activation energy. This cooperative effect explains why the $LiBH_4$-$2LiNH_2$-10%BN composite achieves substantially higher room-temperature conductivity than either $LiBH_4$-$2LiNH_2$ or $LiBH_4$-BN.

At elevated temperatures, similar trends are observed. When heated to 35 ℃, the ionic conductivity of $LiBH_4$-$2LiNH_2$ sharply increases to ~10^{-4} S cm^{-1}, which is consistent with previous reports[24]. Meanwhile, the conductivity of $LiBH_4$-$2LiNH_2$-10%BN attains the highest value of 1.17 × 10^{-3} S cm^{-1}, revealing that BN-induced interfacial engineering simultaneously boosts the intrinsic $LiBH_4$-$2LiNH_2$ transport mechanism and further enhances Li^+ mobility through fast-ion interfacial pathways.

The activation energy was derived from the slope in the Arrhenius plots from 20 ℃ to 60 ℃. A summary of activation energy is shown in **Fig. 5.4(b)**. For $LiBH_4$-$2LiNH_2$, the *Ea* of the low temperature phase (between 20 and 35 °C) is 2.98 eV, whereas in the high-temperature region (above 40 ℃), the Ea values decrease substantially to 0.41 eV. In contrast, the *Ea* values of samples of $LiBH_4$-$2LiNH_2$-5%BN, $LiBH_4$-$2LiNH_2$-10%BN, $LiBH_4$-$2LiNH_2$-15%BN, and $LiBH_4$-10% BN are 0.42 eV, 0.47 eV, 0.58 eV, and 0.96 eV, respectively, as determined from 20 to 60 ℃. All $LiBH_4$-$2LiNH_2$-x%BN composites have a lower activation energy, demonstrating that BN incorporation effectively reduces the energy barrier for Li^+ migration within the solid electrolyte.

In particular, $LiBH_4$-$2LiNH_2$-5%BN and $LiBH_4$-$2LiNH_2$-10%BN samples show a lower activation energy value of 0.42 eV and 0.47 eV, which fall within the typical values of superior ionic conductors (< 0.5 eV)[25]. This substantial decrease indicates that BN introduces favorable Li^+ diffusion pathways at the composite interfaces. Rather than acting as a conductive filler[26], BN functions as an interfacial facilitator that restructures transport bottlenecks originally dominated by $LiBH_4$-$2LiNH_2$ grain boundaries.

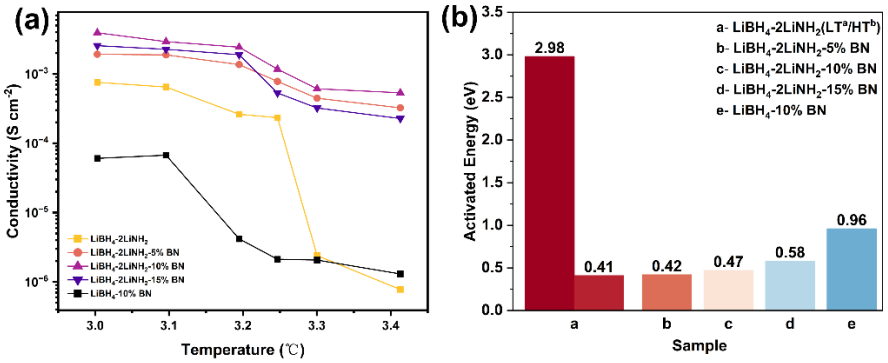

Fig. 5.4 (a) Temperature-dependent ionic conductivity of $LiBH_4$-$2LiNH_2$, $LiBH_4$-$2LiNH_2$-x%BN composites, and $LiBH_4$-10% BN. **(b)** *Ea* value of $LiBH_4$-$2LiNH_2$, $LiBH_4$-$2LiNH_2$-x%BN composites, and $LiBH_4$-10% BN. [a]*Ea* low temperature (LT) phase determined from 25 °C to 35 °C. [b] *Ea* high temperature (HT) phase determined from 35 °C to 60 °C.

Table 5.1 Conductivity of samples.

Sample	$LiBH_4$-$2LiNH_2$	$LiBH_4$-$2LiNH_2$-5%BN	$LiBH_4$-$2LiNH_2$-10%BN	$LiBH_4$-$2LiNH_2$-15%BN	$LiBH_4$-10%BN
$\sigma_{20°C}$ (S cm^{-1})	7.76×10^{-7}	3.24×10^{-4}	5.34×10^{-4}	2.27×10^{-4}	1.30×10^{-6}
$\sigma_{30°C}$ (S cm^{-1})	2.40×10^{-6}	4.47×10^{-4}	6.11×10^{-4}	3.22×10^{-4}	2.07×10^{-6}
$\sigma_{35°C}$ (S cm^{-1})	2.34×10^{-4}	7.79×10^{-4}	1.17×10^{-3}	5.31×10^{-4}	2.12×10^{-6}
$\sigma_{40°C}$ (S cm^{-1})	2.62×10^{-4}	1.36×10^{-3}	2.43×10^{-3}	1.89×10^{-3}	4.17×10^{-6}
$\sigma_{50°C}$ (S cm^{-1})	6.48×10^{-4}	1.88×10^{-3}	2.93×10^{-3}	2.27×10^{-3}	6.73×10^{-5}
$\sigma_{60°C}$ (S cm^{-1})	7.56×10^{-4}	1.92×10^{-3}	3.92×10^{-3}	2.56×10^{-3}	6.05×10^{-5}

To ensure that the BN additive does not introduce significant electronic conduction, the DC polarization measurement was conducted at a voltage of 500 mV for 13,000 s at 50 ℃ in **Fig. 5.5(a)**. The electronic conductivity of $LiBH_4$-$2LiNH_2$-10%BN was determined to be on the order of 10^{-7} S cm^{-1}, which was four orders of magnitude lower than its ionic conductivity. Consequently, the calculated Li^+ transference number reaches 0.999, indicating that nearly all charge transport is carried by Li^+ ions. Such a high transference number is critical for suppressing lithium dendrite formation and is one of the key criteria for an ideal solid-state ionic conductor. The differential scanning calorimetry (DSC) curve of composites showed the transition temperature in **Fig. S5.2.** Pristin**e** $LiBH_4$-$2LiNH_2$ exhibits a pronounced endothermic transition near ~35 °C, corresponding to its structural phase change. Upon BN incorporation, this transition shifts to ~45 °C, suggesting that BN modifies the local structural environment and slightly stabilizes the composite framework. This shift is consistent

with the interfacial interactions between BN and the hydride matrix and further supports the role of BN in tuning both the transport and thermal behavior of the $LiBH_4$-$LiNH_2$ system.

Linear sweep voltammetry (LSV) was employed to evaluate the apparent electrochemical stability window of the SSE, which is critical to choosing a suitable cathode for solid-state electrolytes. A Li| $LiBH_4$-$2LiNH_2$-10%BN|SS was assembled and measured at 50 ℃. As shown in **Fig. 5.5(b),** the LSV curve indicates that there is no component decomposition until 3.25 V (*vs* Li/Li^+), suggesting an apparent electrochemical stability window over 3.0 V, which is much wider than that of ~2.0 V in previous lectures[27]. The improved oxidative stability observed here may be associated with the chemical inertness of BN and its interfacial effects[28], which can delay the onset of decomposition. This finding highlights an additional advantage of BN interfacial engineering: stabilizing both ionic transport and the electrochemical window.

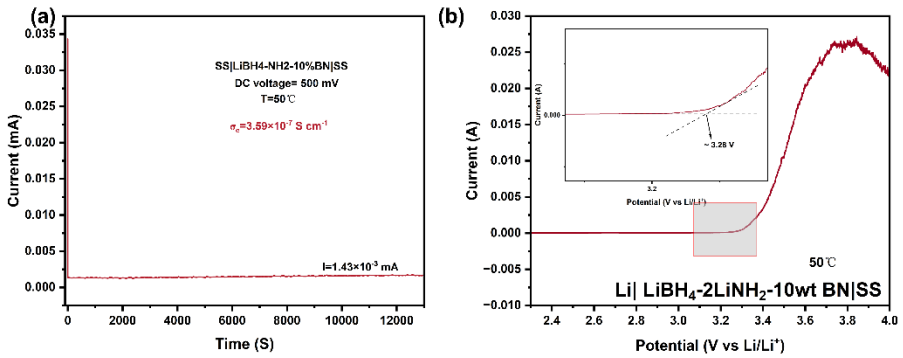

Fig. 5.5 (a) DC polarization curve of the $LiBH_4$-$2LiNH_2$-10%BN. **(b)** LSV curve of the

Li//SS cell within the potential windows of OCV to 4.0 V at a scan rate of 0.1 mV s^{-1} at 50 ℃.

The interfacial compatibility between the electrolyte and lithium metal was assessed using a symmetric Li| $LiBH_4$-$2LiNH_2$-10%BN|Li cell at a current density of 0.05 mA cm^{-2} at RT (**Fig. 5.6**). The remarkably low overpotential (~ 5 mV) and stable cycling over 200 hours clearly demonstrate the outstanding interfacial compatibility between BN-modified electrolyte and lithium metal. Notably, this level of stability represents a significant improvement over previously reported $LiBH_4$-$2LiNH_2$-g-C_3N_4 composites, which could only sustain Li||Li symmetric cycling for ~60 hours at 30 °C and required Li-In alloy anodes for long-term operation[22]. In contrast, BN-modified composite enables stable Li plating/stripping directly with a pure Li anode, thus avoiding the need for expensive alloy-protected electrodes[6] and highlighting the unique advantage of BN-based interfacial engineering in hydride solid electrolytes.

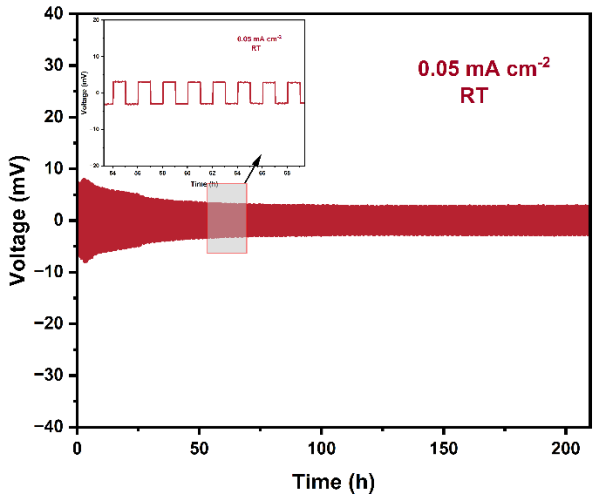

Fig. 5.6 Galvanostatic cycling curves of Li|$LiBH_4$-2$LiNH_2$-10%BN|Li cell at 0.05 mA cm^{-2} and at RT.

To further evaluate the compatibility at elevated temperatures, the symmetric Li|$LiBH_4$-2$LiNH_2$-10%BN|Li cell was tested at 50 °C. As shown in **Fig. 5.7 (a)** and **(b)**, the cell operated at 0.1 mA cm^{-2} with 1-hour current intervals. The overpotential remains exceptionally low, reaching a maximum of only ~7 mV. Importantly, the voltage profile remains highly stable over 180 hours of continuous cycling. The ability of the $LiBH_4$-2$LiNH_2$-10%BN composite to maintain such stability under more aggressive conditions demonstrates that BN interfacial engineering effectively suppresses thermally accelerated side reactions, ensuring uniform Li plating/stripping even at higher operating temperatures.

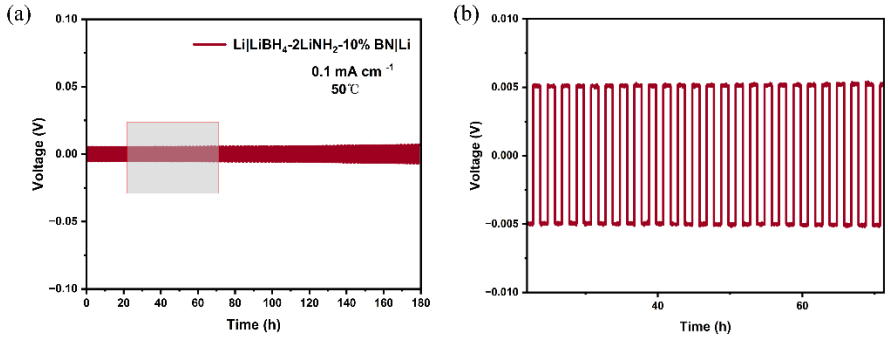

Fig. 5.7 (a) Galvanostatic cycling curves of Li|$LiBH_4$-2$LiNH_2$-10%BN|Li cell at 0.1 mA cm^{-2} and at 50 °C.**(b)** The detailed voltage plateau of Li stripping/plating at selected durations.

The Li dendrite suppression capability of the $LiBH_4$-2$LiNH_2$-10%BN was further examined by galvanostatic charge-discharge (GCD) of a symmetric Li| $LiBH_4$-2$LiNH_2$-10%BN|Li cell at 50 °C under increased current density (**Fig. 5.8**). The cell exhibits highly stable and reversible over-potential and increases smoothly with current density, which means a uniform Li plating and stripping process. As the current density gradually increased to 1.5 mA cm^{-2}, a sudden voltage change occurred, indicating a critical current density to suppress the formation of Li dendrites. These results demonstrate the excellent interfacial compatibility and robust electrochemical stability of the $LiBH_4$-2$LiNH_2$-10%BN composite electrolyte under demanding high-current operation. **Table S5.1** summarizes the ionic conductivity and Li-metal compatibility of the $LiBH_4$-2$LiNH_2$-10%BN electrolyte in comparison with previously reported hydride-based solid electrolytes. The data

clearly show that our BN-hydride composite achieves a uniquely favorable combination of high room-temperature conductivity and long-term stability against pure Li metal.

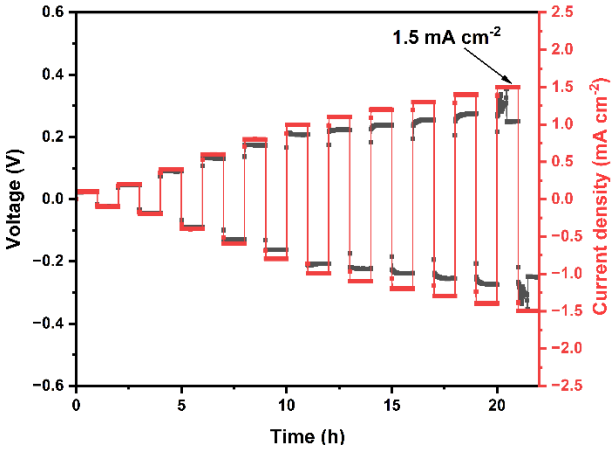

Fig. 5.8 Galvanostatic charge and discharge curves of Li|$LiBH_4$-2$LiNH_2$-10%BN|Li cell at increasing current densities at 50 °C.

To evaluate the practical applicability of the $LiBH_4$-2$LiNH_2$-10%BN electrolyte in all-solid-state lithium batteries, we chose $Li_4Ti_5O_{12}$ (LTO) as the cathode and Lithium metal as the anode to assemble Li|$LiBH_4$-2$LiNH_2$-10%BN|LTO cell. **Fig. 5.9** presents the galvanostatic charge-discharge profiles of the Li|$LiBH_4$-2$LiNH_2$-10%BN|LTO cell for the first three cycles under 0.1 C at 50 °C (1C=175 mAh g^{-1}). The cell exhibits well-defined and flat voltage plateaus at approximately 1.55 V and 1.58 V, corresponding to the characteristic redox reaction of LTO. The narrow voltage hysteresis observed here indicates excellent interfacial contact and fast ionic kinetics, which are enabled by the BN-modified electrolyte. The cell delivers a reversible specific capacity of

approximately 139 mAh g^{-1}, demonstrating high utilization of the active material. The overlapping profiles of the 2nd and 3rd cycles further suggest good initial reversibility. This successful proof-of-concept displays that the $LiBH_4$-$2LiNH_2$-10%BN electrolyte possesses sufficient ionic conductivity and electrochemical stability to support the operation of solid-state lithium metal batteries.

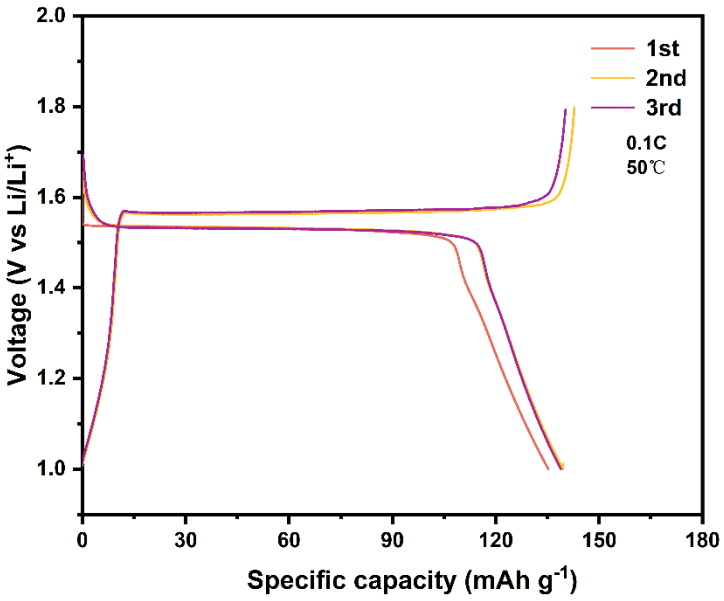

Fig. 5.9 Charge and discharge profiles of Li|$LiBH_4$-$2LiNH_2$-10%BN|LTO cell at 0.1 C and at 50 °C.

5.3 Conclusion

In this work, a series of $LiBH_4$-$2LiNH_2$-BN composite solid

electrolytes was successfully synthesized through a simple, scalable, and solvent-free mechanochemical route. Systematic structural and electrochemical analyses demonstrate that BN fundamentally improves both bulk Li^+ transport and Li-metal compatibility predominantly through interfacial engineering, rather than bulk chemical modification. Among all compositions, the $LiBH_4$-$2LiNH_2$-10%BN composite exhibits the most balanced performance, delivering a high ionic conductivity of 1.17×10^{-3} S cm^{-1} at 35 °C, a significantly broadened electrochemical stability window (~3.25 V), and a substantially reduced activation energy for Li^+ migration.

Crucially, BN incorporation imparts remarkable interfacial stability toward lithium metal. Symmetric Li|SSE|Li cells using the 10% BN composite maintain stable plating/stripping for over 200 hours at room temperature and 180 hours at 50 °C, all with low polarization and without the need for Li-In alloy anode. This behavior highlights that BN primarily stabilizes the electrode-electrolyte interface, rather than altering the intrinsic bulk properties of the electrolyte. Furthermore, the practical feasibility of this electrolyte was preliminarily validated through the reversible operation of a Li|$LiBH_4$-$2LiNH_2$-10%BN|LTO cell.

In summary, compared with established modification strategies, the BN-assisted approach presented here offers a simpler, more scalable, and more practically relevant pathway. The BN-assisted interfacial

modification not only boosts ionic transport but also resolves the critical anode interface bottleneck, paving the way for the practical application of lightweight and high-energy-density solid-state batteries.

5.4 Experimental section

Synthesis

Commercial $LiBH_4$ (Sigma, 95%), $LiNH_2$ (TCI, 95%), and BN (500 nm, Zhongye material) were used as received. BN powder was dried under dynamic vacuum at 200°C for 10h, then transferred to an Ar-filled glove box. $LiBH_4$ and $LiNH_2$ were mixed with a mole ratio of 1:2, named $LiBH_4$-$2LiNH_2$, and then mixed with a different mass fraction (5, 10, and 15wt%) of BN, named $LiBH_4$-$2LiNH_2$-x% BN. Then the mixture of $LiBH_4$-$2LiNH_2$-x% BN was milled on a planetary ball mill (XQM-0.4A, Changsha) at 500 rpm for 5 hours. The weight ratio of ball-to-powder is 13:1. For comparison, $LiBH_4$-10% BN was synthesized in the same conditions. All manipulations of the samples during the experiment were conducted in an Ar-filled glovebox with water and oxygen below 0.1 ppm.

Characterization

XRD patterns were collected by an MAR345 image plate detector with Mo Ka radiation (λ = 0.71072 Å). FTIR spectra were recorded by the attenuated total reflectance (ATR) on Bruker Alpha spectrometer in an argon-filled glovebox. DSC was conducted under Ar flow (total flow of 100 mL min^{-1}). Morphological characterization was achieved through Scanning Electron Microscopy (SEM), employing a ZEISS AURIGA FIB-SEM system.

Cell assemblies and Electrochemical measurement

The solid-state electrolyte pellets were prepared at 600 MPa with a diameter of 9 mm and a thickness of approximately 0.7-0.9 mm. The Electrochemical Impedance Spectroscopy (EIS), direct polarization (DC) method, and Linear Sweep Voltage (LSV) measurements were tested by the EC-lab electrochemical workstation. For EIS measurement, the temperature ranged from 20 to 60 ℃ at an interval of 10 ℃. The symmetrical Swagelok cell was prepared by placing the solid electrolyte pellet between two stainless-steel blocking electrodes. To ensure optimal conductivity, carbon-coated aluminum was applied to both sides of the solid electrolyte pellets. All the cells were maintained at a constant temperature for 1 hour before the measurement. The frequency range of the impedance measurements was set from 7 MHz to 100 mHz. The ionic conductivity can be obtained from the following equation:

$$\sigma = \frac{L}{RS} \qquad (1)$$

Where R represents the resistance of EIS, S represents contact area of SSE and L is the thickness of the SSE (0.6~0.9 mm). The activation energy can be calculated by the Arrhenius equation:

$$\ln \sigma T = \frac{E_a}{K_B T} + C \qquad (2)$$

The DC polarization was measured by two pieces of stainless steel (SS) electrodes with a constant voltage of 0.5 V for 13,000 s. The electronic

conductivity can be calculated by the following equation:

$$R = \frac{V}{I} \qquad (3)$$

The Li|SSE|Li symmetric cells (SSE: $LiBH_4$-$2LiNH_2$-10%BN) were assembled in CR2032 cells for galvanostatic discharge/charge measurements.

The $Li_4Ti_5O_{12}$, SSE, and super P (conductive carbon black) were placed in a mortar with the mass ratio of 4:4:2 and mixed by hand for 10 mins to form a homogeneous material, which was used as the cathode. The SSE (70 mg) was loaded in a 9 mm-diameter die and uniaxially cold-pressed at 400 MPa and held the pressure for 3 mins. Subsequently, 4 mg of composite cathode materials as a cathode, and Li foil as an anode, were assembled to assemble the solid-state battery in CR2032 cells. The fabricated batteries were measured at 0.1 C charging/discharging rate, in the voltage range of 1.0 V-1.8V (*vs* Li/Li^+) at 50 °C.

5.5 Support information

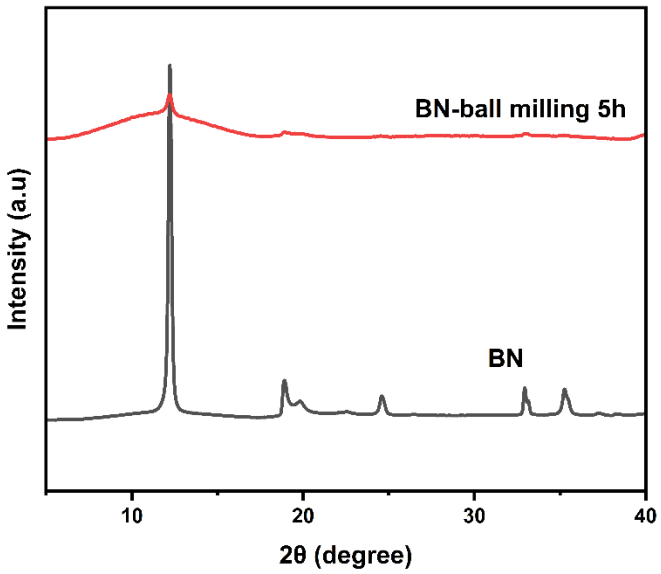

Fig. S5.1 PXRD pattern of BN and BN-ball milling.

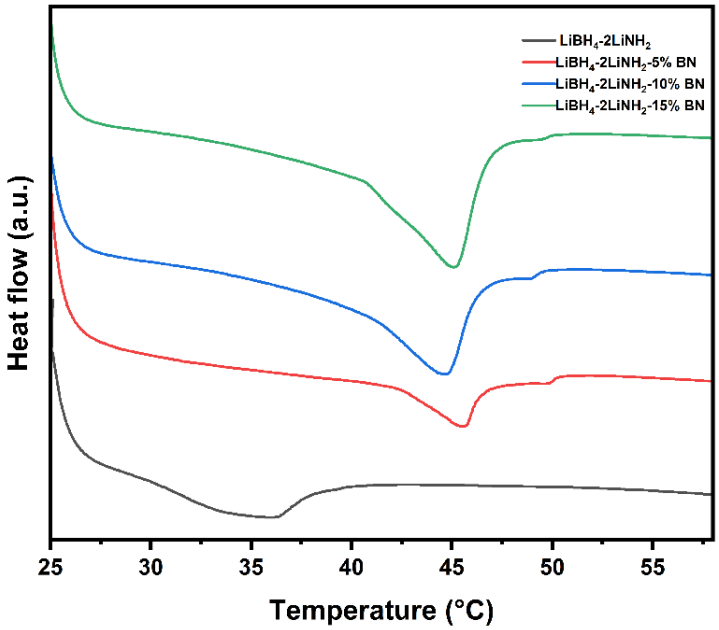

Fig. S5.2 DSC curve of $LiBH_4$-$2LINH_2$ and $LiBH_4$-$2LINH_2$-BN composites.

Table S5.1. A comparison of the electrochemical properties of our work with the previously reported $LiBH_4$-based state electrolyte cells.

Electrolytes	Ionic conductivity ($S\ cm^{-1}$)	Symmetrical Li‖Li cells	References
$LiBH_4$-$2LiNH_2$-BN	1.17×10^{-3} (35℃)	200 hours at RT	This work
$LiBH_4$-$2LiNH_2$	2.0×10^{-4} (RT)	-	[15]
$LiBH_4$-$2LiNH_2$-g-C_3N_4	1.5×10^{-3} (30℃)	60 hours at 45 ℃	[18]
$LiBH_4$-$2LiNH_2$-SiO_2	5.0×10^{-4} (30℃)	-	[17]
$LiBH_4$-BN	1.15×10^{-4} (40℃)	500 hours at 70 ℃	[19]
$LiBH_4$-MoS_2	$\sim10^{-4}$ (RT)	45 hours	[20]
$LiBH_4$-LiI-MoS_2	2.78×10^{-4} S (RT)	35 hours	[21]

5.6 References

1. Nitta, N., Wu, F., Lee, J. T. & Yushin, G. Li-ion battery materials: present and future. *Mater. Today* **18**, 252–264 (2015).
2. Scrosati, B. & Garche, J. Lithium batteries: Status, prospects and future. *J. Power Sources* **195**, 2419–2430 (2010).
3. Liu, Y.-K. *et al.* Research progresses of liquid electrolytes in lithium-ion batteries. *Small* **19**, 2205315 (2023).
4. Blomgren, G. E. Liquid electrolytes for lithium and lithium-ion batteries. *J. Power Sources* **119–121**, 326–329 (2003).
5. Huang, X., Li, T., Fan, W., Xiao, R. & Cheng, X.-B. Challenges and solutions of solid-state electrolyte film for large-scale applications. *Adv. Energy Mater.* **14**, 2303850 (2024).
6. Zhao, Q., Stalin, S., Zhao, C.-Z. & Archer, L. A. Designing solid-state electrolytes for safe, energy-dense batteries. *Nat. Rev. Mater.* **5**, 229–252 (2020).
7. Takahashi, K. *et al.* All-solid-state lithium battery with LiBH4 solid electrolyte. *J. Power Sources* **226**, 61–64 (2013).
8. Sveinbjörnsson, D., Christiansen, A. S., Viskinde, R., Norby, P. &

Vegge, T. The $LiBH_4$-LiI Solid Solution as an Electrolyte in an All-Solid-State Battery. *J. Electrochem. Soc.* **161**, A1432 (2014).

9. Sveinbjörnsson, D. *et al.* Effect of Heat Treatment on the Lithium Ion Conduction of the $LiBH_4$–LiI Solid Solution. *J. Phys. Chem. C* **117**, 3249–3257 (2013).
10. Lee, Y.-S., Ley, M. B., Jensen, T. R. & Cho, Y. W. Lithium Ion Disorder and Conduction Mechanism in $LiCe(BH_4)_3Cl$. *J. Phys. Chem. C* **120**, 19035–19042 (2016).
11. Gulino, V. *et al.* Phase Stability and Fast Ion Conductivity in the Hexagonal $LiBH_4$–LiBr–LiCl Solid Solution. *Chem. Mater.* **31**, 5133–5144 (2019).
12. Yan, Y. *et al.* Ammonia-assisted fast Li-ion conductivity in a new hemiammine lithium borohydride, $LiBH_4 \cdot 1/2NH_3$. *Chem. Commun.* **56**, 3971–3974 (2020).
13. Zhang, T. *et al.* Ammonia, a Switch for Controlling High Ionic Conductivity in Lithium Borohydride Ammoniates. *Joule* **2**, 1522–1533 (2018).
14. Grinderslev, J. B. *et al.* Methylamine Lithium Borohydride as

Electrolyte for All-Solid-State Batteries. *Angew. Chem. Int. Ed.* **61**, e202203484 (2022).

15. Yan, Y. *et al.* A lithium amide-borohydride solid-state electrolyte with lithium-ion conductivities comparable to liquid electrolytes. *Adv. Energy Mater.* **7**, 1700294 (2017).
16. Matsuo, M. *et al.* Complex Hydrides with $(BH_4)^-$ and $(NH_2)^-$ Anions as New Lithium Fast-Ion Conductors. *J. Am. Chem. Soc.* **131**, 16389–16391 (2009).
17. De Kort, L. M., Harmel, J., De Jongh, P. E. & Ngene, P. The effect of nanoscaffold porosity and surface chemistry on the Li-ion conductivity of $LiBH_4$–$LiNH_2$ /metal oxide nanocomposites. *J. Mater. Chem. A* **8**, 20687–20697 (2020).
18. Zhuang, X. *et al.* A cyclic durable all-solid-state battery constructed with $LiBH_4$-based electrolyte with high ionic conductivity at room temperature. *J. Alloys Compd.* **1003**, 175707 (2024).
19. Wu, Z. *et al.* Defective Boron Nitride Inducing the Lithium-ion Migration on the Sub-Surface of $LiBH_4$. *Adv. Funct. Mater.* **32**, 2205677 (2022).

20. Liu, Z. *et al.* Lithium migration pathways at the composite interface of $LiBH_4$ and two-dimensional MoS_2 enabling superior ionic conductivity at room temperature. *Phys. Chem. Chem. Phys.* **22**, 4096–4105 (2020).

21. Liu, Z. *et al.* High ionic conductivities of composites of $Li_4(BH_4)_3I$ with two-dimensional MoS_2 at room temperature. *J. Alloys Compd.* **815**, 152353 (2020).

22. Lu, X., Liu, W., Ouyang, J. & Tian, Y. Distinct surface hydration behaviors of boron-rich boride thin film coatings. *Appl. Surf. Sci.* **311**, 749–752 (2014).

23. Prosini, P. P. $LiBH_4$ as a Solid-State Electrolyte for Li and Li-Ion Batteries: A Review. *Batteries* **9**, 269 (2023).

24. Matsuo, M. *et al.* Complex Hydrides with $(BH_4)^-$ and $(NH_2)^-$ Anions as New Lithium Fast-Ion Conductors. *J. Am. Chem. Soc.* **131**, 16389–16391 (2009).

25. He, X., Zhu, Y. & Mo, Y. Origin of fast ion diffusion in super-ionic conductors. *Nat. Commun.* **8**, (2017).

26. Shan, C. *et al.* Remarkably improved ionic conductivity and lithium

metal compatibility of LLZTO-$Li_4(BH_4)_3I$ composite solid-state electrolyte. *J. Alloys Compd.* **980**, 173554 (2024).

27. Zhuang, X. *et al.* A cyclic durable all-solid-state battery constructed with LiBH4-based electrolyte with high ionic conductivity at room temperature. *J. Alloys Compd.* 175707 (2024).
28. Pakdel, A., Bando, Y. & Golberg, D. Nano boron nitride flatland. *Chem. Soc. Rev.* **43**, 934–959 (2014).

Chapter 6 Discovery of Hybrid Organic-Inorganic Lithium Borohydrides: Correlating structure, thermal stability, and ionic transport behavior

Abstract

The structural engineering of complex hydrides has traditionally relied on metal cation substitution or anion mixing. Hybrid organic-inorganic design has long been proposed as a promising yet unrealized strategy for tuning the structural and transport properties of complex borohydrides. Herein, we present the first systematic synthesis and characterization of a new class of hybrid organic-inorganic lithium borohydrides, derived from the incorporation of tetraalkylammonium cations (R_4N^+, R = Methyl (Me), Ethyl (Et), Butyl (Bu)) into the $LiBH_4$ lattice. X-ray diffraction and spectroscopic analyses reveal that the incorporation of organic cations induces the formation of distinct mixed-cation crystalline phases (PH1 and Li-rich PH2), rather than simple physical mixtures. By varying the alkyl chain length, we establish a clear correlation between cation size, lattice connectivity, thermal stability, and lithium-ion transport behavior. Specifically, the methyl-substituted phase ($Me_4NLi_2(BH_4)_3$, PH2) crystallizes in a *Pnma* symmetry and exhibits s a favorable compromise between lattice flexibility and structural integrity. This new hybrid structure enables fast lithium-ion transport (7.55×10^{-5} S cm^{-1} at 90 °C) with an extended oxidative stability to 3.7 V (*vs* Li^+/Li), surpassing pristine $LiBH_4$. In contrast, larger Et_4N^+ and Bu_4N^+ cations generate excessive free volume, suppressing BH_4^- reorientation and destabilizing the crystal lattice, ultimately yielding low ionic conductivity. These findings

establish organic-cation incorporation as a powerful route to access novel hydride frameworks to tune structure-dynamics-transport relationships and to explore their electrochemical potential.

6.1 Introduction

Conventional modification strategies, such as anion substitution with halides[6–8] or amides[8–11], or the introduction of molecular additives[9], primarily rely on increasing lattice disorder to enhance ion mobility. While effective in activating fast-ion conduction, these approaches inevitably destabilize the crystal framework, leading to lowered melting points or severely narrowed electrochemical stability windows. This persistent trade-off highlights a critical gap in borohydride chemistry: the lack of structural design strategies that decouple lattice dynamics from framework stability.

Organic-inorganic hybridization offers an unexplored degree of freedom for structural engineering. Unlike rigid metal cations, large and anisotropic organic cations (e.g., tetraalkylammonium R_4N^+) possess unique steric and electronic tunability[10–12]. The incorporation of such cations into metal hydride is not merely a physical mixing process; it holds the potential to drive the formation of new crystallographic phases with distinct coordination environments and expanded free volumes. Pioneering studies have successfully demonstrated this concept in multivalent metal systems. For instance, bulky organic cations (e.g., Me_4N^+ and Bu_4N^+) have been incorporated into yttrium (Y^{3+})[13,14] or rare-earth-based (Ho, Tm, Yb) borohydrides[15] and magnesium borohydride ($Mg(BH_4)_2$)[16] to alter their thermal or magnetic properties. However, these findings cannot be directly

translated to lithium-based systems. $LiBH_4$ possesses distinct coordination chemistry and ionic transport requirements essential for solid-state batteries. To date, the systematic creation of hybrid lithium borohydrides has not been studied. Specifically, whether organic cations can be successfully incorporated into $LiBH_4$, and how they influence the critical electrochemical stability, remain open questions.

Previous chapters have demonstrated that interfacial engineering, through the incorporation of inorganic hosts such as zeolites or two-dimensional BN, can effectively enhance the ionic conductivity and electrochemical stability of $LiBH_4$-based electrolytes. In this chapter, we investigate whether organic cations can be systematically incorporated into the $LiBH_4$ framework to regulate crystal chemistry and dynamic behavior. By reacting $LiBH_4$ with tetraalkylammonium borohydrides (R_4NBH_4, R = Me, Et, Bu), we identify two distinct types of mixed-cation phases: a stoichiometric phase (PH1) with limited Li^+ connectivity and a $LiBH_4$-rich phase (PH2) featuring more continuous Li-based substructures. Through a combined structural, thermal, and electrochemical study, we demonstrate how the size of the organic cation governs lattice dimensionality, anion dynamics, and lithium-ion transport, thereby establishing organic-cation engineering as a viable structural design strategy for complex hydrides.

6.2 Results and Discussion

Structural evolution and phase formation in R_4N-$LiBH_4$ systems

Table 6.1. Summary of Synthesized Hydride Phases.

Name	Chemical Formula	Li: [R_4N] Molar Ratio
Me_4N-PH1	$(CH_3)_4NLi(BH_4)_2$	1.15
Me_4N-PH2	$(CH_3)_4NLi_2(BH_4)_3$	2.30
Et_4N-PH1	-	1.15
Et_4N-PH2	-	2.30
Bu_4N-PH1	-	1.15
Bu_4N-PH2	-	2.30

A summary of the investigated R_4N-Li-BH_4 systems is provided in **Table 6.1**. The formation of novel R_4N-$LiBH_4$ (R=Me, Et, Bu) hybrid phases was first examined by PXRD. Unlike simple physical mixtures, high-energy ball milling of $LiBH_4$ with Me_4NBH4 drives a chemical transformation, yielding novel hybrid phases that depend on the molar ratio. As shown in **Fig. 6.1**, the PXRD patterns of Me_4N-Li-BH_4 samples with a 1:1 molar ratio (Me_4N-PH1), several new reflections occurred, which cannot be assigned to either pristine $LiBH_4$ or TMAB, evidencing the formation of a new mixed-cation borohydride phase. Increasing the $LiBH_4$ content to a 1:2 ratio leads to the emergence of additional reflections, generally broader and distinct from those

observed for PH1. This indicates the formation of the second phase, hereafter referred to as Me_4N-PH2. At still higher $LiBH_4$ content (3:1 to 7:1), the characteristic peaks of $LiBH_4$ become increasingly dominant, implying the presence of unreacted $LiBH_4$ in the sample. Overall, these results demonstrate that phase formation in Me_4N-$LiBH_4$ is highly dependent on the $LiBH_4$: TMAB molar ratio. Adjusting this ratio yields either a single mixed-cation phase (PH1 or PH2) or two-phase mixtures containing one mixed-cation phase together with excess $LiBH_4$, reflecting different extents of structural ordering and reaction completeness

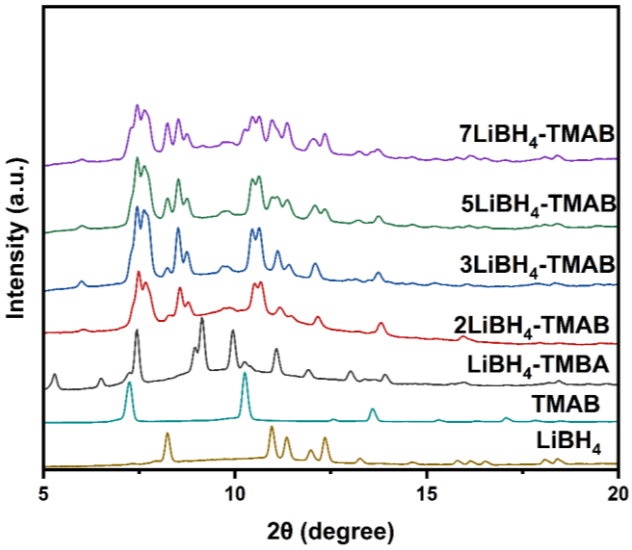

Fig. 6.1. PXRD spectra of Me_4NBH_4:$LiBH_4$ mixtures after ball-milling with different molar ratios.

To clarify the structural regulation induced by organic cations

incorporation, the crystal structures of the Me_4N-Li-BH_4 system were determined through PXRD analysis and Rietveld refinement. Two distinct phases can be clearly identified: $(Me_4N)Li(BH_4)_2$ (PH1) (*Immm*) and $(Me_4N)Li(BH_4)_2$(PH2) (*Pnma*). A detailed comparison of the two phases is summarized in **Table 6.2**.

In the Me_4N-PH1 phase, the crystal structure consists of liner $[Li(BH_4)_2]^-$ complex anions charge-balanced by $(Me_4N)^+$ organic cations. Each Li^+ cation is coordinated by four nearly tetrahedral BH_4^- tetrahedra through Li-H interactions, which are analogous to those reported in $NH_4Li_2(BH_4)_3$[17]. The Li-H distances range from 1.9 to 2.2 Å, corresponding to Li-B separations of approximately 2.4-2.7 Å, indicating a slightly asymmetric coordination environment around Li^+ and confirming Li^+ can build the cation framework with tetrahydroborate anion (BH_4^-)[18]. The incorporation of the bulky $(Me_4N)^+$ cations disrupts the three-dimensional $[Li(BH_4)_4]$ network of $LiBH_4$, yielding a more open and weakly connected one-dimensional $[Li(BH_4)_2]^-$ units[19,20].

Interestingly, increasing the $LiBH_4$ content to a 1:2 ratio drives the crystallization of a Li-rich phase, the Me_4N-PH2 adopts a lower symmetry (*Pnma*) and exhibits a distinct connected anionic framework, in which each Li^+ cation is predominantly coordinated by three BH_4^- groups, giving rise to a continuous one-dimensional $[Li_2(BH_4)_3]^-$ chain extending along the b axis. Unlike reported $NH_4Li_2(BH_4)_3$, where BH_4^-

complexes connect two or four Li^+ to form a fully three-dimensional Li-BH_4 framework, the one-dimensional connectivity of Me_4N-PH2 is more likely associated with the large steric footprint of Me_4N^+ cation, which restricts and prevents the formation of higher-dimensional frameworks. The chain topology of PH2 closely resembles that structure of $Li_2A(BH_4)_3$ (A= Rb, Cs)[18]. The Li-H and Li-B distances (1.75-2.15 Å and 1.82-2.92 Å, respectively) reveal a more asymmetric and anisotropic coordination environment than in PH1.

The transformation from *Immm* to *Pnma* is accompanied by lattice expansion and the generation of additional Li sites. Both phases adopt one-dimensional ion chains interconnected by a dihydrogen-bond network, highlighting the structural adaptability of the Me_4N-Li-BH_4 system upon phase evolution. (**Fig. 6.2**).

Table 6.2 Structural data for new tetramethylammonium lithium borohydride.

Chemical formula	$(Me_4N)\ Li(BH_4)_2$	$(Me_4N)\ Li_2(BH_4)_3$
Sample temperature	RT	RT
Crystal system	orthorhombic	orthorhombic
Space group	*Immm* (No.71)	*Pnma* (No.62)
a (Å)	15.33360	18.5790
B (Å)	9.08991	6.7427
C (Å)	6.83738	9.8723
β (º)	90	90
V($Å^3$)	953.001	1236.73

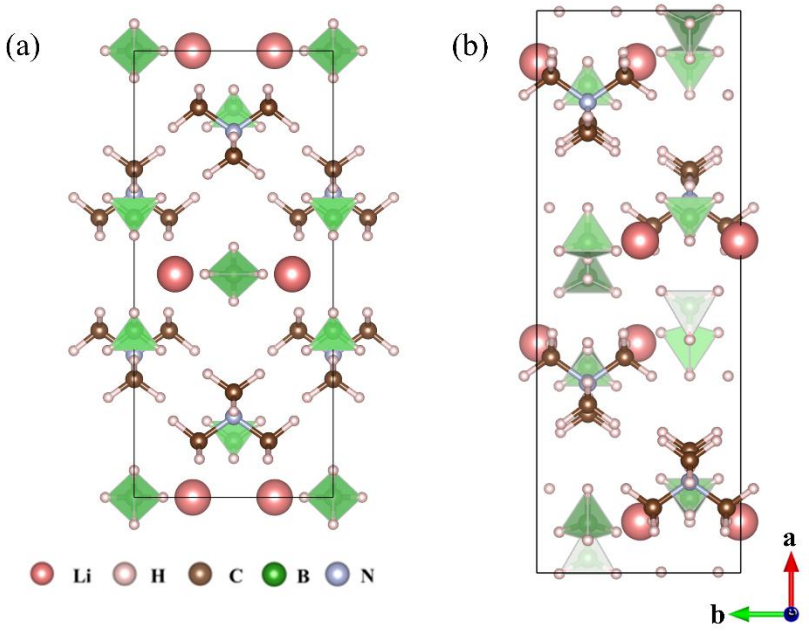

Fig. 6. 2 Crystal structures of (a) $(Me_4N)Li(BH_4)_2$ and $(Me_4N)Li_2(BH_4)_3$.

A similar phase evolution trend is observed when comparing the PXRD patterns of the Et_4N-Li-BH_4 and Bu_4N-Li-BH_4 systems (**Fig. 6.3),** where both 1:1 and 2:1 molar ratios give rise to new reflections superimposed on residual $LiBH_4$ peaks. This suggests partial formation of mixed-cation phases coexisting with unreacted $LiBH_4$ domains. The systematic appearance of new peaks across all R_4N^+ species confirms that chemical interaction, rather than mechanical mixing, drives phase formation. However, with increasing cation size, the diffraction peaks become broader and less intense, reflecting enhanced lattice distortion and reduced crystallinity induced by the bulky alkyl chains. This observation implies that the organic cations introduce substantial free volume and positional disorder, which may alter the dynamic behaviour of the BH_4^- anions and thereby influence ionic transport properties.

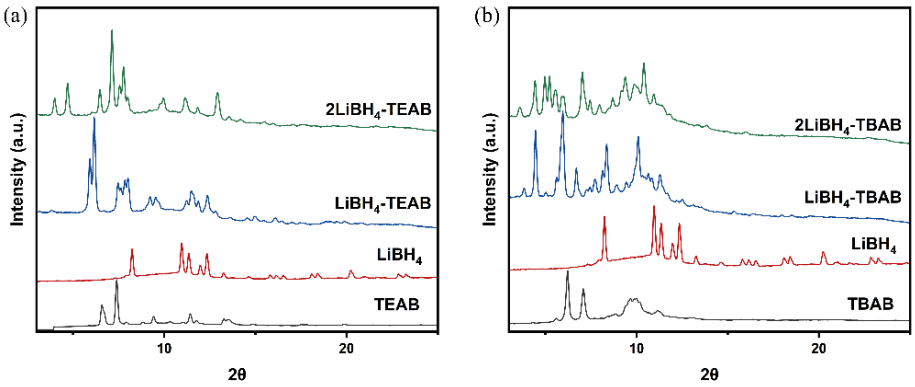

Fig. 6.3 PXRD pattern of **(a)** Et_4N-Li-BH_4 and **(b)** Bu_4N-Li-BH_4.

Lattice vibration and anion dynamics revealed by FTIR spectroscopy

The local bonding environments and dynamic behavior of the BH_4^- groups were analyzed by Fourier-transform infrared spectroscopy (FTIR). **Fig. 6.4** shows the FTIR spectra of R_4N-Li-BH_4 (R=Me, Et, Bu) systems and their pristine components. Pristine $LiBH_4$ exhibits two characteristic absorption bands at 2270 cm^{-1} corresponding to the B-H stretching vibration, and peaks at 1069 cm^{-1} originate from B-H bending modes[20]. After the introduction of the R_4NBH4, new absorption bands appear near 1484-1490 cm^{-1} and 940-970 cm^{-1} regions, assigned to C-H and C-N stretching vibrations[10,21], respectively, confirming the presence of the R_4N^+ group. For the Et_4N-$LiBH_4$ composites, an additional absorption band emerges around 1600 cm^{-1}, which is assigned to the C-H bending (scissoring) vibration of the CH_2 groups in the ethyl chains[22]. Notably, there is no absorption in the 2500-3000 cm^{-1} region, which indicates a lack of B-O vibrational signatures. These observations confirm that BH_4^- remains chemically intact, and that hybrid formation proceeds without partial oxidation or side reactions.

Compared with pristine $LiBH_4$, all Me_4N-Li-BH_4 composites display a red shift of the B-H stretching band. This change indicates weakened B-H interactions and partial charge delocalization between Li^+, Me_4N^+, and BH_4^-. Meanwhile, the -H and C-N bands remain visible, confirming

the existence of the Me_4N^+ cation during composite formation.

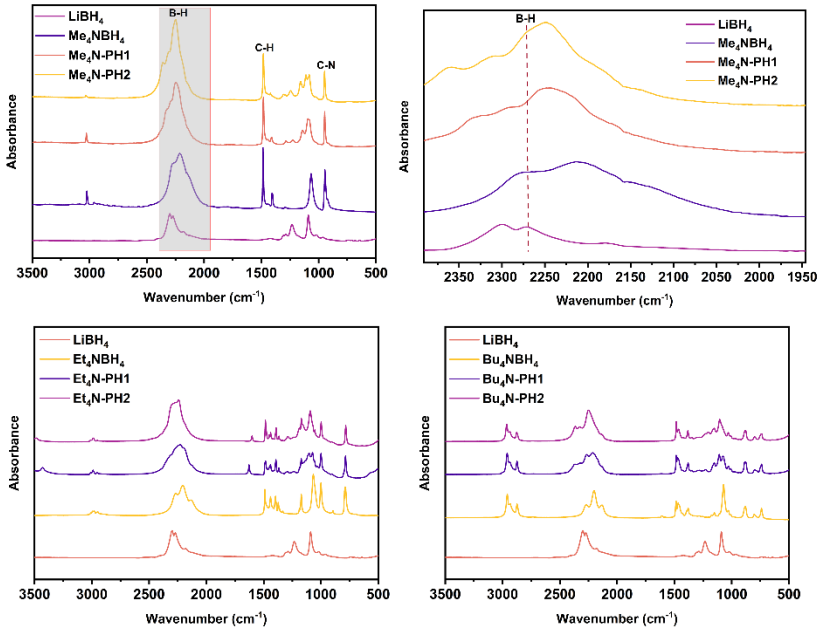

Fig. 6.4 FT-IR spectra of **(a)** Me_4N-Li-BH_4, **(b)** Enlarge zoom of the vibration bands B-H, **(c)**Et_4N-Li-BH_4, and **(d)**Bu_4N-Li-BH_4.

Thermal behavior of R_4N-$LiBH_4$ systems

The thermal behavior of the R_4N-Li-BH_4 composites was investigated by differential scanning calorimetry (DSC) and thermogravimetric analysis (TGA). For the Me_4N-Li-BH_4 system, synchrotron in-situ X-ray diffraction and differential scanning calorimetry (DSC) measurements were performed in PH2. The temperature-dependent XRD patterns (30-180 °C) show a gradual shift

in peak position and changes in intensity, indicating progressive structural rearrangement upon heating. It undergoes phase transitions at 100 and 130 ℃, consistent with the first two endothermic features in the DSC curve. These transitions are attributed to structural rearrangements involving Li^+ redistribution and BH_4^- reorientation, reflecting increasing dynamic disorder.

Upon further heating to 219 °C, the diffraction pattern collapses and is accompanied by a sharp endothermic event and measurable mass loss in TGA, confirming melting followed immediately by decomposition, which is lower than the melting point of $LiBH_4$ (286 °C)[2] and TMAB(235 °C)[12], indicating reduced thermal stability of the composite. This melting point depression likely arises from the introduction of bulky Me_4N^+ cations, which disrupts the original $LiBH_4$ crystalline framework, reduces lattice energy, and weakens electrostatic cation-anion interactions. The resulting structural frustration and enhanced disorder lower the energy barrier for melting. A similar trend has been observed in the $Mg(BH_4)_2$-TMAB system[16], suggesting a general effect of organic cation incorporation in borohydrides.

In contrast, there are no phase-transition peaks that occur in Me_4N-PH1 according to DSC curve (**Fig. S6.1**), only a single endothermic peak appears at 217 °C, also accompanied by a pronounced weight loss, similar to that of PH2. Therefore, the upper limit of the thermal stability for Me_4N-$LiBH_4$ is around 219 °C.

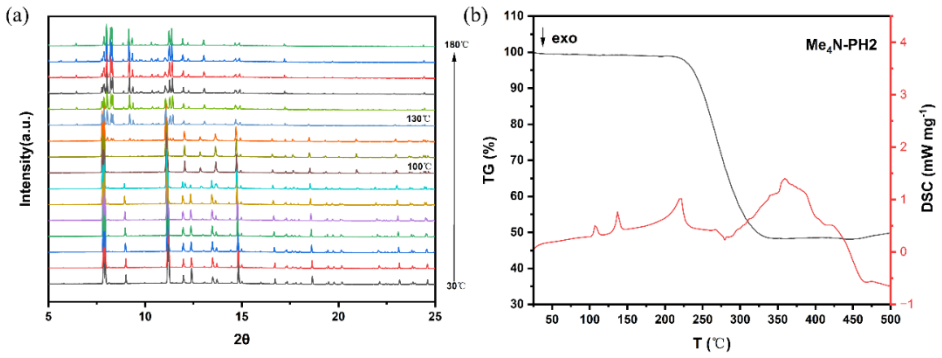

Fig. 6.6 (a) *In-situ* SR-PXD of Me_4N-PH2. (b) TGA-DSC curve of Me_4N-PH2.

Et_4N^+ incorporation results in substantially weaker thermal stability compared to Me_4N^+. In the Et_4N-Li-BH_4 systems, Et_4N-PH1 exhibits a continuous structural transition between 50 °C and 86 °C according to *in-situ* XRD, consistent with a weak endothermic event observed in the DSC curve. This marks the onset of structural rearrangement. At approximately 105 °C, all diffraction peaks disappear, and a more pronounced endothermic peak appears near 100 °C in the DSC curve, indicating melting with complete loss of long-range order. No mass loss is observed until temperatures approach ~200 °C. The Et_4N-PH2 shows an even more complex thermal behavior. Two distinct structural transitions occur around 50-70 °C and 70-100 °C, corresponding to the two endothermic events in the DSC curve. At approximately 148 °C, all diffraction peaks disappear, coinciding with an endothermic peak in the DSC but without detectable mass loss in TGA, indicating melting without decomposition. At higher temperatures (~200 °C), the TGA curve shows a sharp weight loss, confirming thermal decomposition of

the sample. These results demonstrate that Et_4N^+ induces much stronger lattice frustration than Me_4N^+, resulting in earlier structural collapse and a broader molten regime.

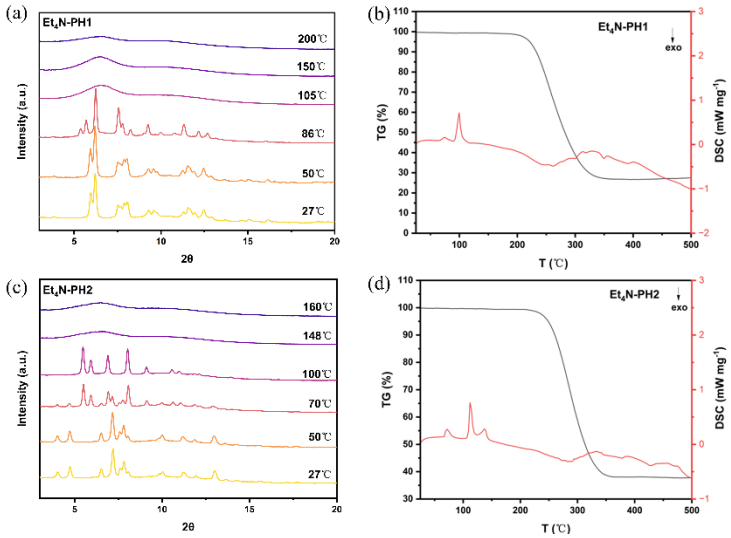

Fig. 6.7 *In-situ* PXRD of **(a)** Et_4N-PH1 and **(c)** Et_4N-PH2 and corresponding TGA-DSC curve of **(b)** Et_4N-PH1 and **(d)** Et_4N-PH2.

The Bu_4N^+, the largest in this series, produces the most dramatic thermal destabilization. For Bu_4N-PH1, the XRD patterns begin to change between 45 -50 °C, with peak deformation corresponding to a small endothermic signal and a minor mass loss (**Fig. 6.8(b)**). This suggests partial decomposition prior to melting, a behavior absent in the Me_4N^+ and Et_4N^+ systems. Between 50 -70 °C, the diffraction peaks gradually weaken and eventually disappear, indicating a melting process. A slow mass loss (~10%) accompanies this range, while a

major decomposition step occurs only near ~200 °C.

For Bu_4N-PH2, the XRD patterns remain unchanged up to 65 °C. However, between 65 -75 °C, peak intensities rapidly decrease, coinciding with a sharp endothermic peak in DSC and an initial weight loss in TGA, indicating that the sample begins to melt while partially decomposing. By 105 °C, no crystalline peaks are observed, confirming the molten state. Like PH1, significant decomposition occurs only at ~200 °C. The thermal behavior of Bu_4N-Li-BH_4 is like that (Tm=78°C) in tetrabutylammonium yttrium borohydride (TBAYB)[14], illustrating the general destabilizing influence of long alkyl chains in tetraalkylammonium borohydrides.

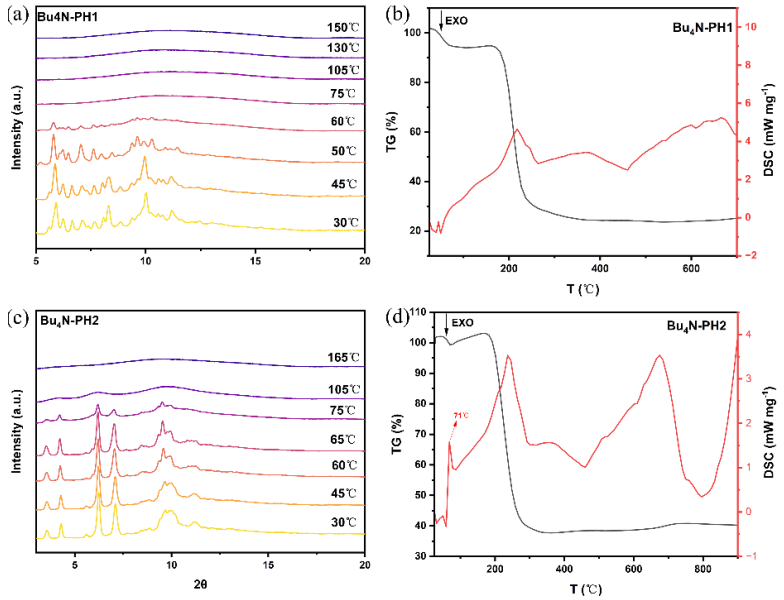

Fig. 6.8 *In-situ* PXRD of **(a)** Bu_4N-PH1 and **(c)**Bu_4N-PH2 and corresponding TGA-DSC curve of **(b)** Bu_4N-PH1and **(d)** Bu_4N-PH2.

All samples exhibit multiple endothermic events below 250 °C, occurring at temperatures significantly lower than those of pristine $LiBH_4$ and tetraalkylammonium borohydrides (R_4NBH_4, where R = methyl (Me), ethyl (Et), and butyl (Bu))[23,24], which correspond to successive solid-solid transitions or melting processes. As the size of the organic cation increases, the Li-BH_4 framework experiences progressively greater steric expansion, rendering the lattice more prone to relaxation. At the same time, the electrostatic interactions between Li^+ and BH_4^- are weakened, lowering the lattice energy and reducing the resistance of the structure to thermal perturbation. The larger alkyl substituents also introduce enhanced dynamic-disorder in BH_4^- reorientation and organic-cation motion, which further destabilizes the framework under heating. These effects collectively erode long-range structural connectivity, most prominently in the Bu_4N^+ system. These results demonstrate that the size of the organic cation governs the balance between lattice rigidity and dynamic softening, ultimately determining the melting behavior and overall thermal stability of the hybrid borohydrides.

Correlation between lattice dynamics and electrochemical properties

Electrochemical impedance spectroscopy (EIS) was employed to evaluate the ionic transport behavior of the R_4N-Li-BH_4 composites within the temperature range of 40-90 °C (**Fig. 6.9**). All samples show

semicircular Nyquist plots at low temperatures, which gradually shrink with increasing temperature, indicating thermally activated ionic conduction (**Fig. S6.2-S6.4**). The extracted conductivities and activation energies are summarized in **Table 6.3**.

For each system, the $LiBH_4$-rich borohydrides (PH2, nominal 2:1) exhibit significantly higher conductivity than the corresponding PH1 (1:1) phase, highlighting the role of Li^+ concentration and structural connection in facilitating ion migration. For Me_4N-Li-BH_4 system, Me_4N-PH2 displays the highest ionic conductivity, reaching 7.55×10^{-5} S cm^{-1} at 90 °C, representing a two-order-of-magnitude enhancement compared with pristine $LiBH_4$[25]. This enhanced performance is accompanied by a relatively low activation energy of 0.59 eV.

Furthermore, the electronic conductivity of Me_4N-PH2 was determined to be 6.72×10^{-9} S cm^{-1} by DC measurement at 90 °C (**Fig. S6.5**), which is more than four orders of magnitude lower than its ionic conductivity. Accordingly, the Li-ion transference number of Me_4N-PH2 was calculated to be higher than 0.999, indicating that the electronic conductivity is almost negligible in Me_4N-PH2. These results validate that moderate structural distortion and active BH_4^- reorientation promote Li^+ mobility.

Linear sweep voltammetry (LSV) was further conducted to assess the electrochemical stability of the Me_4N-Li-BH_4 system. No noticeable decomposition occurs until 4.49 V for Me_4N-PH1 and 3.70 V (*vs* Li^+/Li)

for Me_4N-PH2 (**Fig. S6.6**). Both values are substantially higher than that of pristine $LiBH_4$ (~2.0 V vs Li^+/Li)[26,27], indicating that the incorporation of the Me_4N^+ cation effectively broadens the electrochemical stability window. The slightly lower oxidative stability of PH2 relative to PH1 may be attributed to its Li^+ framework, which exposes BH_4^- units more directly compared to the more compact PH1 structure. This combination of ionic conductivity driven by structural dynamics and extended apparent electrochemical stability window under blocking conditions suggests potential compatibility with high-voltage cathodes, which highlights Me_4N-PH2 as a promising model system for exploring structure-dynamics-transport relationships in lithium borohydrides, with potential relevance to solid-state electrolyte applications.

In contrast, the Et_4N-PH2 and Bu_4N-PH2 composites exhibit lower solid-state conductivities and higher activation energies. This decrease in conductivity can be attributed to the progressive increase in cation size, which introduces excessive free volume and suppresses cooperative BH_4^- rotational dynamics, thereby limiting Li-ion transport.

Notably, the Bu_4N-PH2 sample exhibits two distinct activation energy regimes. In the low-temperature region (LT), a relatively high activation energy is observed, consistent with sluggish Li^+ transport in a highly disordered and weakly connected framework. In contrast, a significantly reduced activation energy is obtained in the high-

temperature region (HT), which is related to the sharp conductivity increase up to 10^{-2} S cm^{-1} at 90 °C, which coincides with the melting region identified in the DSC results. This behavior is characteristic of melt-assisted ion transport, where ion diffusion occurs within a partially liquid environment rather than through a crystalline conduction network.

Taken together, these results establish a unified structure–dynamics–transport relationship across the series. Optimal Li^+ conduction is achieved when the organic cation induces moderate lattice softening that enhances BH_4^- reorientation while preserving sufficient structural connectivity for long-range Li^+ percolation. The Me_4N-PH2 phase exemplifies this balance, offering high ionic conductivity, negligible electronic contribution, and broad electrochemical stability. By contrast, excessively large cations (Et_4N^+, Bu_4N^+) over-soften the lattice, leading to fragmented Li^+ pathways or melting at low temperatures and thus restricting solid-state ion transport.

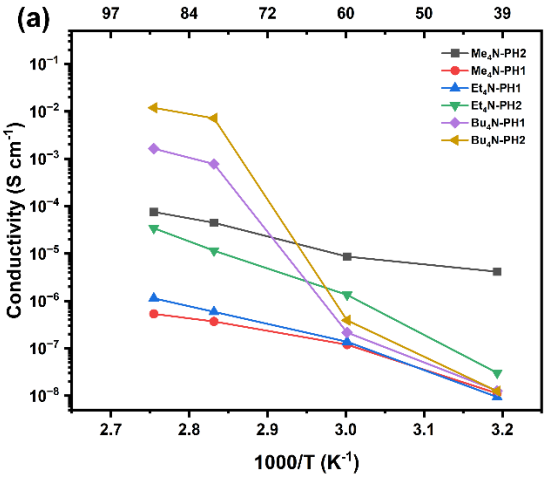
(a)
97
84
72
60
50
39
Me4N-PH2
Me4N-PH1
Et4N-PH1
Et4N-PH2
Bu4N-PH1
Bu4N-PH2
Conductivity (S cm-1)
10-1
10-2
10-3
10-4
10-5
10-6
10-7
10-8
2.7
2.8
2.9
3.0
3.1
3.2
1000/T (K-1)

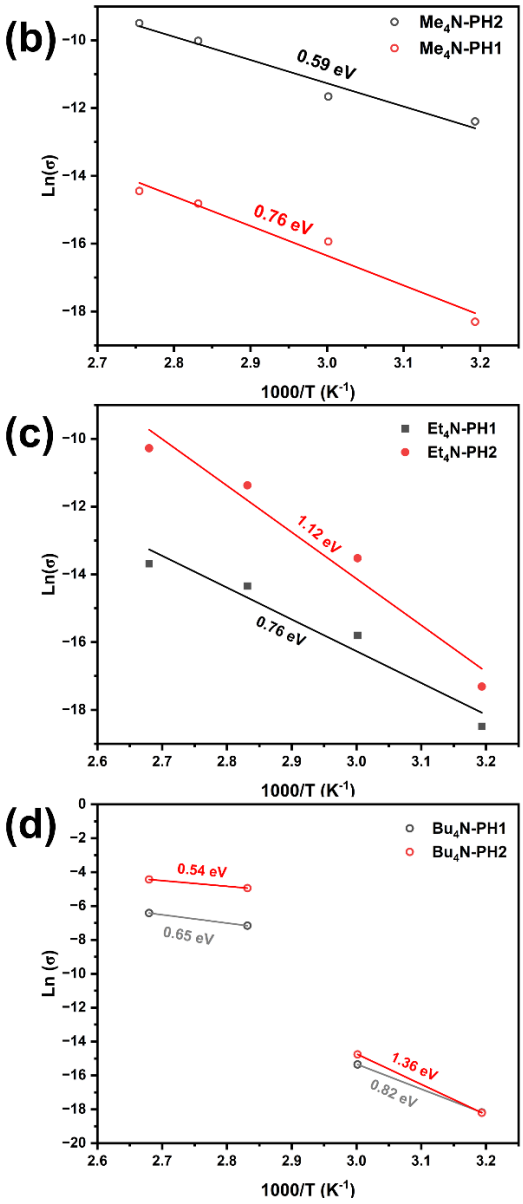

Fig. 6.9 (a) Temperature-dependent ionic conductivity of Me_4N-$LiBH_4$, Et_4N-Li-BH_4 and Bu_4N-Li-BH_4.The Arrhenius curves for **(b)** Me_4N-$LiBH_4$, **(c)** Et_4N-$LiBH_4$, and **(d)** Bu_4N-Li-BH_4.

Table 6.3 Ionic conductivity and *E*a.

Sample	Li: [R_4N] Molar Ratio	σ (40°C) (S cm^{-1})	σ (90°C) (S cm^{-1})	E_a (eV)
Me_4N-Li-BH_4	1:1	1.12×10^{-8}	5.33×10^{-7}	0.76
	2:1	4.14×10^{-8}	7.55×10^{-5}	0.59
Et_4N-Li-BH_4	1:1	9.38×10^{-9}	1.14×10^{-6}	0.76
	2:1	3.04×10^{-8}	3.44×10^{-5}	1.12
Bu_4N-Li-BH_4	1:1	1.27×10^{-8}	1.64×10^{-3}	0.82 (LT)/0.65 (HT)
	2:1	1.24×10^{-8}	1.19×10^{-2}	1.36 (LT)/0.54 (HT)

The above results demonstrate that the incorporation of organic cations has a strong effect on both the thermal stability and ionic transport behavior of borohydride. This dual effect originates from the interaction between the crystal structure, anion dynamics, and cation-induced structural disorder. In addition, Li ion concentration also plays an important role in forming different phases. A higher $LiBH_4$ content favors the formation of the $LiBH_4$-rich phase (PH2), which has more connected Li^+ pathways, while a lower Li^+ content leads to the mixed-cation phase (PH1) with weaker conductivity. Therefore, both the amount of Li^+ and the size of the organic cation jointly determine the structure and ion transport properties of the R_4N-$LiBH_4$ borohydrides.

In the $LiBH_4$-rich phase (PH2), the moderate lattice distortion

induced by the Me_4N^+ cation softens the framework and promotes Li^+ redistribution. Rather than simple expansion, this structural distortion is key to enhancing ion transport. Following the theoretical framework of Kim *et al.*[28], the distorted lattice facilitates Li^+ transport by enlarging migration channels and reducing the depth of potential wells. This leads to a flattened energy landscape that promotes rapid long-range diffusion in the hybrid structure. This lattice relaxation activates BH_4^- reorientation, giving rise to a typical "paddle-wheel" effect[29] that significantly lowers the Li^+ migration barrier. Meanwhile, the partial weakening of Li-BH_4 interactions slightly decreases the melting point while maintaining overall structural integrity. As a result, the Me_4N-PH2 phase achieves an excellent balance between high ionic conductivity and good thermal stability.

When the alkyl chain length increases to Et_4N^+ and Bu_4N^+, steric effects become dominant. Larger organic cations create excessive free space and local strain, disrupting the continuous Li^+ conduction pathways and suppressing cooperative BH_4^- rotational motions. Consequently, the activation energy increases, the ionic conductivity decreases, and the lattice stability is compromised. In the Bu_4N-$LiBH_4$ system, the melting temperature drops to approximately 50-80 °C, leading to early melting and quasi-liquid ionic diffusion. While too-soft lattice enhances ion movement but inevitably reduces thermal stability.

Overall, both Li^+ concentration and organic-cation size control the

relationship between the structure and properties of the R_4N-$LiBH_4$ borohydrides:

(1) Higher Li^+ content promotes formation of $LiBH_4$-rich phases (PH2) with enhanced Li^+ transport;
(2) Moderate lattice softening improves ion mobility while maintaining the structure stability;
(3) Oversized organic-cations induce lattice instability and premature melting;
(4) The overall performance exhibits a non-monotonic dependence on cation size ($Me_4N^+ > Et_4N^+ > Bu_4N^+$).

6.3 Conclusion

This chapter has demonstrated that the incorporation of organic cations into lithium borohydrides offers a conceptually distinct route for regulating ionic transport through intrinsic lattice engineering. By systematically introducing tetraalkylammonium borohydrides with increasing alkyl-chain length, a series of mixed-cation lithium borohydride phases with markedly different structural and dynamic characteristics was obtained.

A clear structure-dynamics-transport relationship is established: as the cation size increases, the lattice becomes progressively softer and less stable, leading to concurrent changes in ionic conductivity and

thermal stability. The $LiBH_4$-rich Me_4N-PH2 phase achieves an optimal balance between lattice flexibility and structural connectivity, exhibiting an intrinsic solid-state ionic conductivity of 7.55×10^{-5} S cm^{-1} at 90 °C with an extended apparent electrochemical stability window under blocking conditions while maintaining good thermal stability. The high conductivity observed in Bu_4N-based phases originates from melt-assisted transport rather than intrinsic solid-state conduction, emphasizing the importance of maintaining structural integrity.

While the hybrid organic-inorganic borohydrides investigated here do not yet represent optimized solid electrolytes for immediate application, this work demonstrates that intrinsic lattice modulation constitutes a powerful and complementary design strategy to interface-dominated approaches. The insights gained in this chapter provide a conceptual foundation for integrating lattice engineering and interfacial control, which is further discussed in the general conclusions and perspectives of this thesis.

6.4 Experimental Section

All sample preparation was carried out in an argon-filled glovebox ($H_2O \leq 1$ ppm, $O_2 \leq 1$ ppm) to avoid moisture or oxygen contamination. The commercial lithium borohydride ($LiBH_4$), tetramethylammonium borohydride ($(CH_3)_4NBH_4$, Me_4NBH_4, TMAB), tetraethylammonium borohydride ($(C_2H_5)_4NBH_4$, Et_4NBH_4, TEAB), and n-tetrabutylammonium borohydride ($(C_4H_9)_4NBH_4$, Bu_4NBH_4, TBAB) were all purchased from Sigma-Aldrich and used as received without further purification.

Two compositions were prepared for each R_4NBH_4-$LiBH_4$ system (R= Me, Et, and Bu), corresponding to molar ratios of 1:1.15 and 1:2.3, and are referred to as "PH1" and "PH2" phases, respectively. The mixtures were synthesized by high-energy ball milling of $LiBH_4$ and R_4NBH_4 using a Fritsch Pulverisette 7 premium line planetary ball mill. Milling was performed in a 45 mL stainless steel jar containing three stainless steel balls (10 mm diameter; total mass = 41 g). The specific ball-to-powder mass ratios (BPRs) and sample compositions for each phase are summarized in **Table 6.3**.

Table 6.3. Summary of Synthesized Hydride Phases.

Name	Chemical Formula	Li: [R_4N] Molar Ratio	BPR (Ball-Powder Ratio)
Me_4N-PH1	$(CH_3)_4NLi(BH_4)_2$	1.15	359
Me_4N-PH2	$(CH_3)_4NLi_2(BH_4)_3$	2.30	295
Et_4N-PH1	-	1.15	172
Et_4N-PH2	-	2.30	150
Bu_4N-PH1	-	1.15	207
Bu_4N-PH2	-	2.30	190

Materials Characterization

Powder X-ray diffraction (PXRD). PXRD measurements were performed using two Incoatec X-ray generators (mixed Mo Kα radiation, weighted average λ = 0.71073 Å). Due to the air sensitivity of the samples, powders were loaded into 0.7 mm glass capillaries inside an argon-filled glovebox. The diffraction patterns were recorded on a MAR345 image plate and integrated using the program Fit2D.

***In-situ* synchrotron radiation powder X-ray diffraction (*in situ* SR-PXD).** *In-situ* synchrotron diffraction experiments were conducted at the beamline BM01 of the Swiss-Norwegian Beamlines (SNBL) at the European Synchrotron (ESRF, Grenoble, France) using a PILATUS 2M detector (Dectris, Switzerland). The incident X-ray wavelength was

0.77509 Å. Samples were sealed in glass capillaries under argon and subsequently heated from room temperature to 180 ℃ with a heating rate of 5 ℃ min^{-1} during data collection.

Fourier Transform Infrared (FTIR) spectroscopy analysis. Infrared spectra were recorded between 400 and 4000 cm^{-1} using a Bruker α II spectrometer equipped with an attenuated total reflectance (ATR) accessory. All measurements were carried out in an argon-filled glovebox to avoid air exposure.

Thermal properties. Samples were investigated by thermogravimetric analysis and differential scanning calorimetry (TGA/DSC) was performed on a NETZSCH STA 449 F3 Jupiter instrument equipped with a stainless-steel furnace and operated inside an argon-filled glovebox. Samples were heated from 25 °C to 600 °C at a constant heating rate of 5 °C min^{-1}.

Electrochemical Test

The ionic conductivity of the solid-state electrolytes (SSEs) was determined by electrochemical impedance spectroscopy (EIS) using a BioLogic VMP-300 potentiostat. Nyquist plots were recorded over a frequency range of 7 MHz to 100 mHz, with an applied AC voltage amplitude of 100 mV.

The SSE powders were pressed into solid pellets with a diameter of

9 mm and a thickness of approximately 0.5-1.3 mm under a cold pressure of 600 MPa. The pellets were assembled into symmetric Swagelok-type cells with stainless steel (SS) blocking electrodes, forming an SS|SSEs|SS configuration.

EIS measurements were conducted between 40 °C to 90 °C. The temperature increased at 0.33 °C min^{-1}, and impedance spectra were collected at 10 °C intervals. Before each measurement, the cell was equilibrated at the target temperature for 30 minutes to ensure thermal stability and reproducibility.

The ionic conductivity (σ) was calculated using the following equation:

$$\sigma = \frac{L}{RS} \quad (1)$$

Where L (in cm) is the thickness of the SSEs, R (in Ω) is the value of bulk resistance obtained from the complex EIS plots, and S (in cm^2) is the pellet cross-sectional area.

Direct current (DC) polarization was conducted at 500 mV constant voltage to analyze the electronic conductivity.

The linear scanning voltammogram (LSV) of the borohydride was obtained at 50 ℃ using a lithium foil (the reference electrode) and a stainless steel (the working electrode) sandwiching the pressed pellets. The range of the test voltage used was open circuit voltage (OCV) to 5.0 V at the scanning rate of 0.1 mV s^{-1}.

6.5 Support information

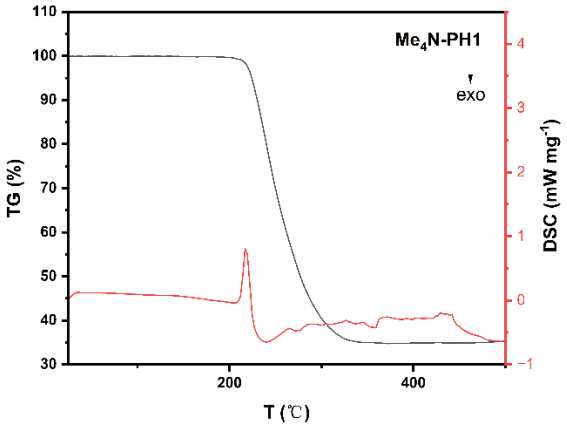

Fig. S6.1 DSC curve of Me_4N-PH1.

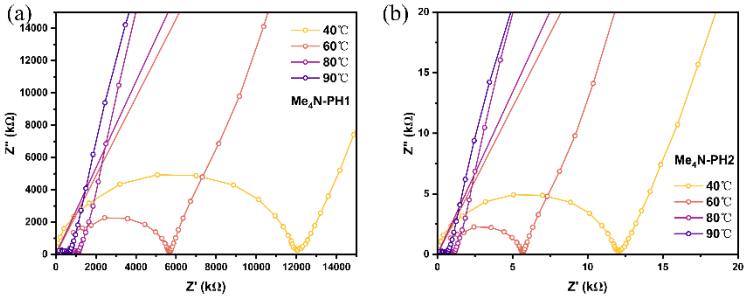

Fig. S6.2 EIS plots of **(a)** Me_4N-PH1 and **(b)** Me_4N-PH2.

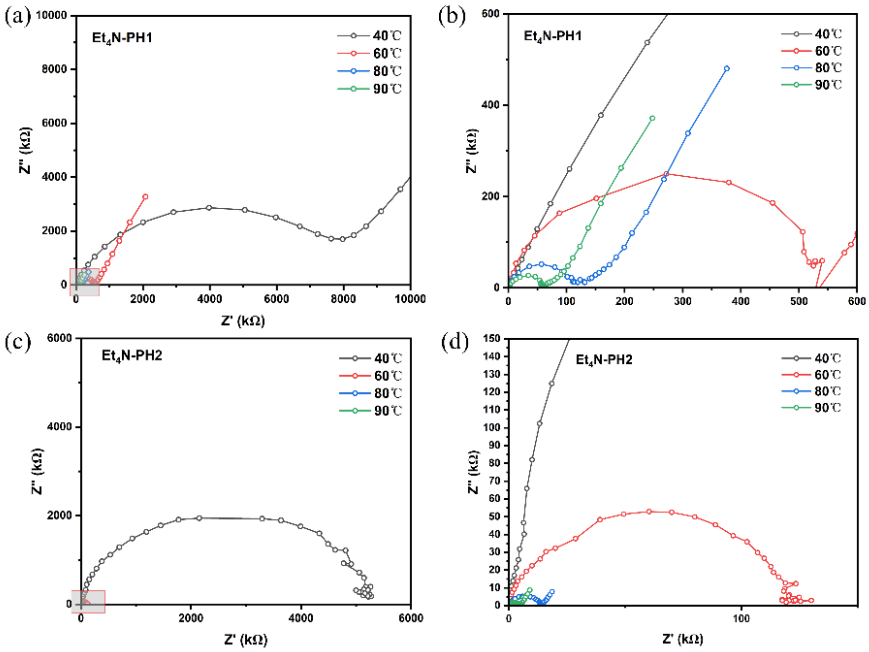

Fig. S6.3 EIS plots of **(a)-(b)** Et_4N-PH1 and **(c)-(d)** Et_4N-PH2.

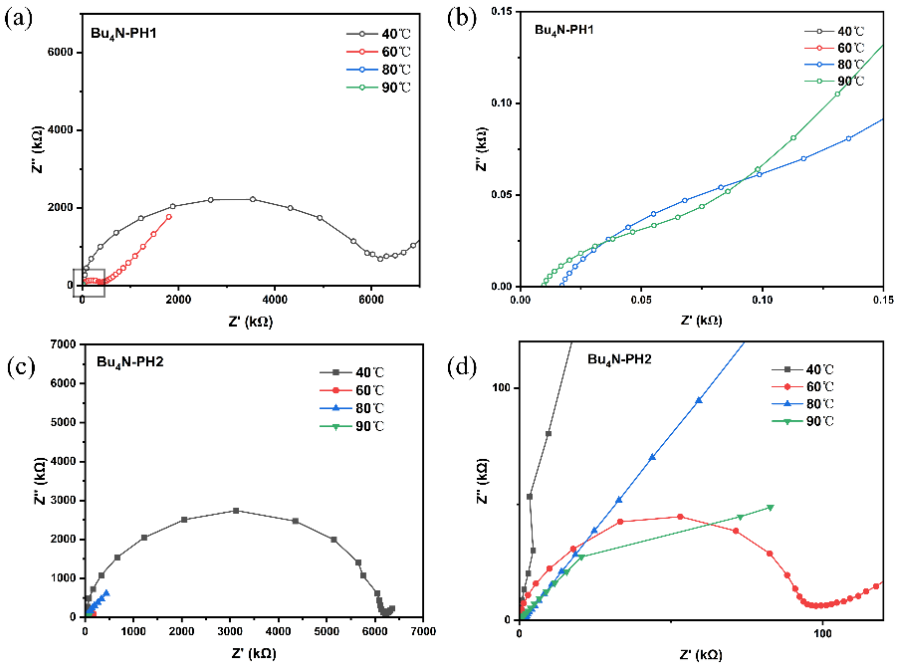

Fig. S6.4 EIS plots of **(a)-(b)** Bu4N-PH1 and **(c)-(d)** Bu4N-PH2.

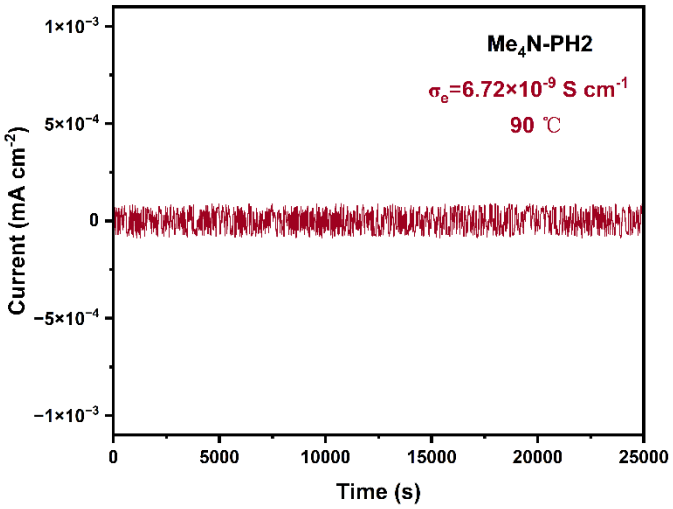

Fig. S6.5 DC polarization plot of a SS|Me4N-PH2|SS.

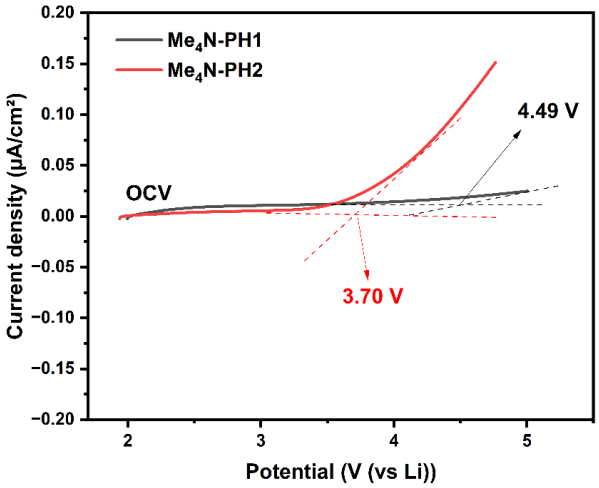

Fig. S6.6 LSV curve of Me_4N-$LiBH_4$.

6.6 References

1. Mohtadi, R., Remhof, A. & Jena, P. Complex metal borohydrides: multifunctional materials for energy storage and conversion. *J. Phys.: Condens. Matter* **28**, 353001 (2016).
2. Paskevicius, M. *et al.* Metal borohydrides and derivatives–synthesis, structure and properties. *Chem. Soc. Rev.* **46**, 1565–1634 (2017).
3. Edelstein, N. Bonding in metal borohydride complexes. *Inorg. Chem.* **20**, 297–299 (1981).
4. Orimo, S., Nakamori, Y., Eliseo, J. R., Züttel, A. & Jensen, C. M. Complex Hydrides for Hydrogen Storage. *Chem. Rev.* **107**, 4111–4132 (2007).
5. Luo, X. & Aguey-Zinsou, K.-F. Correlations between the ionic conductivity and cation size in complex borohydrides. *Ionics* **26**, 5287–5291 (2020).
6. Rude, L. H. *et al.* Iodide substitution in lithium borohydride, $LiBH_4$–LiI. *J. Alloys Compd. 509, 8299–8305 (2011).*
7. Arnbjerg, L. M. *et al.* Structure and Dynamics for $LiBH_4$−LiCl

Solid Solutions. *Chem. Mater.* **21**, 5772–5782 (2009).

8. Cascallana-Matias, I., Keen, D. A., Cussen, E. J. & Gregory, D. H. Phase Behavior in the $LiBH_4$–LiBr System and Structure of the Anion-Stabilized Fast Ionic, High Temperature Phase. *Chem. Mater.* **27**, 7780–7787 (2015).
9. Grinderslev, J. B. *et al.* Methylamine Lithium Borohydride as Electrolyte for All-Solid-State Batteries. *Angew Chem Int Ed* **61**, e202203484 (2022).
10. Mishchenko, A. M. *et al.* Preparation of *closo*-decaborate by pyrolysis of tetraethylammonium borohydride: Revision and optimization for large-scale production. *Polyhedron* **279**, 117646 (2025).
11. Kendall, D. S. & Lipscomb, W. N. Crystal structure of tetramethyl ammonium tetradecahydrodecaborate. Structure of the $B_{10}H_{14}^{2-}$ ion. *Inorg. Chem.* **12**, 546–551 (1973).
12. Banus, M. D., Bragdon, R. W. & Gibb, T. R. P. Jr. Preparation of Quaternary Ammonium Borohydrides from Sodium and Lithium Borohydrides. *J. Am. Chem. Soc.* **74**, 2346–2348 (1952).

13. Jaroń, T. & Grochala, W. Probing Lewis acidity of $Y(BH_4)_3$via its reactions with MBH_4 (M = Li, Na, K, NMe4). *Dalton Trans.* **40**, 12808–12817 (2011).

14. Jaroń, T., Wegner, W., Cyrański, M. K., Dobrzycki, Ł. & Grochala, W. Tetrabutylammonium cation in a homoleptic environment of borohydride ligands: $[(n\text{-}Bu)_4N][BH_4]$ and $[(n\text{-}Bu)_4N][Y(BH_4)_4]$. *J. Solid State Chem.* **191**, 279–282 (2012).

15. Wegner, W. & Jaroń, T. Synthesis, Polymorphism and Thermal Decomposition Process of $(n\text{-}C_4H_9)_4NRE(BH_4)_4$ for RE = Ho, Tm and Yb. *Materials (Basel)* **14**, 1329 (2021).

16. Bell, R. T. *et al.* $Mg(BH_4)_2$-Based Hybrid Metal–Organic Borohydride System Exhibiting Enhanced Chemical Stability in Melt. *ACS Appl. Energy Mater.* **4**, 1704–1713 (2021).

17. Grinderslev, J. B. *et al.* Structural Diversity and Trends in Properties of an Array of Hydrogen-Rich Ammonium Metal Borohydrides. *Inorg. Chem.* **59**, 12733–12747 (2020).

18. Schouwink, P., Smrčok, Ľ. & Černý, R. Role of the Li+ node in the Li-BH4 substructure of double-cation tetrahydroborates. *Acta Cryst*

B **70**, 871–878 (2014).

19. Soulié, J.-P., Renaudin, G., Černý, R. & Yvon, K. Lithium borohydride $LiBH_4$: I. Crystal structure. *J. Alloys Compd.* **346**, 200–205 (2002).
20. Filinchuk, Y., Chernyshov, D. & Dmitriev, V. Crystal chemistry of light metal borohydrides. *arXiv preprint arXiv:1003.5378* (2010).
21. Hartman, M. R., Rush, J. J., Udovic, T. J., Bowman, R. C. & Hwang, S.-J. Structure and vibrational dynamics of isotopically labeled lithium borohydride using neutron diffraction and spectroscopy. *J. Solid State Chem.* **180**, 1298–1305 (2007).
22. Hlel, F., Rheim, A., Guerfel, T. & Guidara, K. Synthesis, calorimetric study, infrared spectroscopy and crystal structure investigation of β-$[(C_2H_5)_4N][(CH_3)_4N]ZnCl_4$. Z. *Naturforsch. B* **61**, 1002–1006 (2006).
23. Pringle, J., Howlett, P., MacFarlane, D. & Forsyth, M. Organic ionic plastic crystals: Recent advances. *J. Mater. Chem.* **20**, (2010).
24. Züttel, A. et al. Hydrogen storage properties of $LiBH_4$. *J. Alloys Compd*. **356–357**, 515–520 (2003).

25. Takahashi, K. et al. All-solid-state lithium battery with $LiBH_4$ solid electrolyte. *J. Power Sources* **226**, 61–64 (2013).

26. Gulino, V. *et al.* Phase Stability and Fast Ion Conductivity in the Hexagonal $LiBH_4$–LiBr–LiCl Solid Solution. *Chem. Mater.* **31**, 5133–5144 (2019).

27. Asakura, R. *et al.* Electrochemical Oxidative Stability of Hydroborate-Based Solid-State Electrolytes. *ACS Appl. Energy Mater.* **2**, 6924–6930 (2019).

28. Kim, K. & Siegel, D. J. Correlating lattice distortions, ion migration barriers and stability in solid electrolytes. *J. Mater. Chem. A* **7**, 3216–3227 (2019).

29. Zhang, Z. & Nazar, L. F. Exploiting the paddle-wheel mechanism for the design of fast ion conductors. *Nat. Rev. Mater.* **7**, 389–405 (2022).

Chapter 7 Conclusion and perspectives

7.1 Conclusion

Research on solid-state electrolytes has already become an important trend in the field of new energy. And borohydrides, due to their potential high ionic conductivity and lightweight nature, show unique application prospects. This thesis investigated borohydride-based solid-state electrolytes through a combination of interfacial engineering and structure modification strategies, aiming to address three central challenges that hinder their practical application: low ionic conductivity at moderate temperatures, limited electrochemical stability, and insufficient interfacial compatibility with electrodes.

Chapter 1 presented the background and motivation of this study, providing a brief introduction to the fundamentals of Li- and Na-based batteries as well as the classification and development of typical solid-state electrolytes, and clarified the research objectives and directions for borohydride-based electrolytes.

Chapter 2 briefly described the synthesis methods and the characterization techniques employed (XRD, FTIR, BET, EIS, CV, etc.), which laid the methodological foundation for the subsequent systematic study.

Chapter 3 demonstrated the effect of zeolite confinement of $LiBH_4$: due to zeolite's porosity and high surface area, which facilitate the formation of continuous interfacial ion-transport pathways, a high ionic

conductivity of 10^{-4} S cm^{-1} at 80 ℃ with significantly reduced activation energies were achieved, consistent with an interfacial-dominated transport mechanism. In addition, the composite electrolyte showed good compatibility in electrochemical applications; solid-state cells assembled with LTO cathodes exhibited stable cycling performance at 80 °C and 100 °C, further highlighting the relevance of the zeolite confinement strategy as an interfacial design concept for improving ionic transport in borohydride-based electrolytes.

Chapter 4 extended the zeolite-based composite strategy to sodium borohydride systems. $Na_2B_{12}H_{12}$-zeolite composites exhibited enhanced Na^+ conductivity, indicating that this design approach is transferable across different alkali systems. Moreover, when employed as the solid electrolyte in Na||Na symmetric cells, the composite enabled stable cycling at 80 °C. These results demonstrate that the zeolite-based composite strategy is transferable to Na^+-conducting borohydrides, reinforcing the general relevance of interfacial engineering for alkali-metal hydride electrolytes.

In **Chapter 5**, the known conductive $LiBH_4$-$LiNH_2$ system was modified by the introduction of two-dimensional BN, revealing the synergistic role of 2D materials in interface engineering. The incorporation of BN not only enhanced the mechanical strength and interfacial stability of the composite electrolyte but also facilitated the formation of a mechanically robust and ionically favorable interfacial

architecture, improving ion transport across the interface. Benefiting from these effects, the composite electrolyte exhibited higher ionic conductivity and lower activation energy, along with enhanced electrochemical performance. In Li||Li symmetric cells, stable cycling behavior was observed at both room temperature and 50 °C, and shows good compatibility with LTO cathode, further confirming the significance of interface engineering strategies in advancing the practical potential of borohydride-based solid electrolytes.

Chapter 6 systematically investigates a series of R_4NBH_4-$LiBH_4$ borohydrides. The study shows that these composites are not simple physical mixtures but new mixed-cation phases. Their crystal structures vary with composition, revealing clear differences at different cation ratios. The alkyl-chain length of the R_4N^+ cation strongly affects the melting point of the resulting phases. In addition, the ionic conductivity of these materials was measured. Notably, the Me_4NBH_4-$LiBH_4$ sample with a molar ratio of 1:2 named Me_4N-PH2 exhibited an ionic conductivity of 10^{-5} S cm^{-1} at 80 °C, providing new insight into improving the ionic conductivity of $LiBH_4$-based borohydride.

Chapter 7 summarized the major results and outlined future research directions, including a deeper understanding of ion transport at the atomic scale, improving interface stability with both cathodes and anodes, developing scalable synthesis methods, and exploring new nanoporous or hybrid hosts.

In summary, this thesis demonstrates that the introduction of rigid inorganic support as well as flexible organic constituents effectively enhances the ionic conductivity of borohydrides. This strategy not only provides a new perspective for the application of borohydrides as solid-state electrolytes but also lays the groundwork for future optimization of ion transport through interface engineering and composite design.

Nevertheless, several limitations remain in the present work. The fundamental understanding of interfacial ion transport mechanisms is still incomplete, particularly regarding the dynamic coupling between structural disorder and ion migration. In addition, the long-term electrochemical stability and compatibility with practical electrode materials have not yet been fully established. Furthermore, the scalability and reproducibility of some composite systems require further investigation for practical implementation.

It is expected that addressing these challenges will play an important role in advancing borohydride-based solid electrolytes and accelerating their integration into next-generation all-solid-state batteries.

7.2 Perspective

So far, the results presented in this thesis demonstrate that both interfacial engineering and structure modification can effectively enhance the ionic transport properties of borohydride-based solid electrolytes. Although significant progress has been achieved, several

critical challenges must still be addressed before these materials can be practically implemented in all-solid-state batteries, particularly in systems requiring stable long-term cycling performance.

A key direction concerns interfacial stability and compatibility with high-voltage cathodes. Although certain borohydride phases already exhibit expanded electrochemical stability windows up to ~3.8 V, coupling them with high voltage layered oxides such as Lithium nickel manganese cobalt oxides (NMC) or $LiFePO_4$ still faces major obstacles due to interfacial chemical reactions and high contact resistance. Future work should therefore focus on developing tailored interfacial coatings or functional interlayers that enable stable, low-impedance contact between electrochemically inert borohydride electrolytes and high-energy cathode materials.

Beyond interfacial considerations, a deeper understanding of ion-transport mechanisms at the atomic scale remains essential. Although structure-property relations have been established in this work, the precise coupling between anion reorientational dynamics, lattice softening, and lithium-ion migration pathways is not yet fully understood. Advanced experimental techniques, such as quasi-elastic neutron scattering or solid-state NMR combined with computational modeling, will be crucial to quantitatively disentangle these contributions and to guide the rational design of next-generation hydride electrolytes.

Another promising avenue lies in the exploration of multicomponent composite electrolytes. Recent studies have begun to investigate the role of borohydrides in polymer- and sulfide-based electrolytes, for example, as interfacial modifiers or functional additives to improve stability and enhance the continuity of ion-conducting networks[1–3]. Such research provides new perspectives for the utilization of borohydrides, particularly in the design of composite solid electrolytes. Looking forward, the integration of borohydrides with polymers, sulfides, and other classes of electrolytes may not only enable performance complementarity but also open more diverse and sustainable directions for the development of all-solid-state batteries.

From an application-oriented perspective, scalability and processing compatibility represent additional challenges. Although mechanochemical synthesis provides a simple and solvent-free route for laboratory-scale material preparation, the translation of these approaches to industrially relevant processing conditions requires further investigation, including pellet fabrication, composite densification, and long-term stability under operating conditions.

In summary, while this thesis establishes clear design principles for enhancing ionic transport in borohydride-based solid electrolytes, it also highlights that their successful deployment in all-solid-state batteries will depend on coordinated advances in interface engineering, mechanistic understanding, and materials processing. Addressing these

challenges will require interdisciplinary efforts spanning solid-state chemistry, electrochemistry, and materials engineering.

7.3 References

1. Bao, K. *et al.* Modulating composite polymer electrolyte by lithium closo-borohydride achieves highly stable solid-state battery at 25°C. *Sci. China Mater.* **65**, 95–104 (2022).

2. Wang, Y. *et al.* Understanding the Role of Borohydride Doping in Electrochemical Stability of Argyrodite Li6PS5Cl Solid-State Electrolyte. *Advanced Materials* **n/a**, 2506095.

3. Wei, Y. *et al.* Polymeric Electronic Shielding Layer Enabling Superior Dendrite Suppression for All-Solid-State Lithium Batteries. *ACS Nano* **18**, 5965–5980 (2024).